EMI Analysis and Modeling of Switching Circuits

POLITECNICO DI TORINO
Facoltà di Ingegneria

Corso di Dottorato in
Ingegneria Elettronica e delle Comunicazioni

Tesi di Dottorato

EMI Analysis and Modeling of Switching Circuits

Analisi e Modelli delle Emissioni Elettromagnetiche
di Circuiti a Commutazione

Riccardo Trinchero

Coordinatore
Prof. I. Montrosset

Tutori
Prof. F. Canavero
Prof. I. Stievano

XXVII ciclo

Acknowledgments

First and foremost, this thesis would not have been accomplished without the vital supports of many people. I would like to thank *in primis* my advisor, Prof. Flavio Canavero for offering me the great opportunity to join the EMC Group and undertake this activity. Then I wish to thank Prof. Igor Stievano for his continuos help during my activity.

I also acknowledge my colleagues, who are part of an enjoyable work environment. Special thanks to Elisabetta for her help and patience with the administrative things.

Last but not the least, I would like to thank my family for their constant support in my life. To them I dedicate this thesis.

Contents

Abstract

Nowadays, switching power converters are massively used in almost any electrical and electronic equipment and appliances. This class of circuits are inherently time-varying systems that are characterized by the periodic activity of their internal switches which leads to discontinuos absorbed currents. The above currents, that play the role of high frequency noisy disturbances feeding the power distribution system, become a serious concern for designers that need to comply with the electromagnetic compatibility (EMC) regulation for the conducted emission (CE). In this framework, modeling and simulation tools for switching circuits are key resources in the early design phase for the prediction of the conducted emission and for the assessment of alternative design scenarios.

The classical approach to CE prediction is via physical-based models and time-domain simulations. This solution, however, requires intimate knowledge of the internal device structure. Also, large simulation times are in general needed to avoid integration errors and to achieve accurate results (the CE are in fact computed by applying the Fourier transform on the steady-state portion of the current response of the circuit). As an alternative, frequency-domain behavioral approaches are available in literature. In the latter case, the proposed models are small-signal time-invariant approximations computed from the external observation of the circuit behavior. These approaches, that are based on simplified equivalents, do not take into account the internal time-varying nature of the circuit and in many cases unavoidably lead to a model accuracy that strongly depends on the operating condition of devices.

To overcome the above limitations, this thesis proposes an alternative approach to CE assessment based on the mathematical framework developed for time-varying circuits and systems. The proposed method allows for the steady-state prediction of circuit responses directly in the frequency-domain. A topological approach is used, where the original time-varying circuit is suitably replaced by an augmented time-invariant equivalent solved via standard tools for circuit analysis. The new augmented variables in the above equivalent turn out to be the harmonic coefficients of the Fourier series expansion of the corresponding voltage and current variables in the original circuit. A second important contribution in this work is the application of the proposed mathematical tool to the modeling of a switching converter and of its CE disturbances from measured data. The converter is seen as a black-box element that is characterized via a limited set of port voltage and current observations, leading to an equivalent augmented admittance fully describing the time-varying nature of the system.

Summarizing, this thesis provides a comprehensive theoretical discussion together with several tutorial examples. What is more important, it proposes a novel approach to CE prediction with improvements with respect to state-of-the-art approaches and linear time-invariant surrogates. A

real application test case involving a dc-dc boost converter and real measured data is also used to validate the method and stress its features for both numerical simulation and black-box modeling.

Sommario

Oggigiorno i convertitori a commutazione vengono impiegati nella maggior parte dei dispositivi per l'elettronica di potenza. I suddetti convertitori presentano un comportamento periodico tempo variante, in quanto il loro funzionamento è basato sulla commutazione periodica della configurazione del circuito tramite l'impiego di interruttori elettronici. Dal punto di vista della compatibiltà elettromagnetica (EMC), i circuiti a commutazione sono considerati come la principale sorgente di rumore all'interno della rete di alimentazione. Infatti le commutazioni del circuito introducono delle discontinuità nel comportamento delle correnti assorbite, generando rumore ad alta frequenza. In questo scenario la simulazione numerica riveste un ruolo fondamentale nelle prime fasi del processo di progettazione; infatti consente ai progettisti di predire e limitare i livelli delle emissioni condotte (EC) in modo da rispettare i limiti imposti dagli standard EMC.

Classicamente le EC per dispositivi commutati vengono modellate e simulate tramite modelli nel dominio del tempo, basati su una descrizione dettagliata di ogni componente del circuito. Le simulazioni nel dominio del tempo presentano spesso problemi di convergenza dovuti alla scelta del tempo di campionamento e tempi di simulazione lunghi, in quanto le emissioni condotte vengono stimate applicando la trasformata di Fourier alla risposta a regime delle correnti del circuito.

L'alternativa è quella di stimare le EC del circuito direttamente nel dominio della frequenza tramite modelli comportamentali. I modelli comportamentali sono approssimazioni di piccolo segnale tempo invariati del circuito a commutazione, che ignorano completamente la natura tempo variante del dispositivo e forniscono in alcuni casi risultati poco accurati.

Questa tesi mira ad estendere i risultati presenti in letteratura e a fornire un approccio differente per l'analisi e la modellazione delle EC di circuiti a commutazione, basato sulla loro natura tempo variante. Infatti la formulazione matematica sviluppata per i sistemi lineari tempo varianti consente di caratterizzare questa importante tipologia di circuiti direttamente nel dominio della frequenza. L'approccio usato per la simulazione dei dispositivi a commutazione è basato sulla sostituzione degli elementi del circuito con una loro rappresentazione aumentata ottenuta tramite un'espansione in serie di Fourier delle variabili del circuito. La nuova interpretazione del circuito consente di sostituire il comportamento tempo variante degli interruttori con un equivalente ammettenza o impedenza tempo invariante, permettendo di analizzare il circuito tramite approcci standard per la analisi dei circuiti tempo invarianti come l'analisi nodale.

Nell'ultima parte della tesi viene fornito un approccio innovativo di modellazione "black-box" di un generico circuito a commutazione. Il modello proposto è basato su una rappresentazione aumentata impedenza o ammettenza ad una porta dell'interno dispositivo direttamente nel dominio della frequenza, ottenuta tramite una serie di misure. Il modello aumentato proposto estende i risultati in letteratura in quando permette di considerare la natura tempo variante del dispositivo

mostrando un'accuratezza superiore nella stime delle EC rispetto ai modelli surrogati tempo invariati.

La tesi fornisce una discussione completa e teorica dei circuiti commutati combinata con esempi illustrativi mirata a comprendere e completare il materiale pubblicato e a validare l'approccio considerato.

List of Acronyms

CCM	continuous conduction mode
CE	conducted emissions
CM	common mode
DFT	discrete Fourier transform
DM	differential mode
DUT	device under test
EMC	electromagnetic compatibility
EMD	electromagnetic disturbances
EMI	electromagnetic interferences
FFT	fast Fourier transform
IFFT	inverse fast Fourier transform
LISN	line impedance stabilization network
LTI	linear time-invariant
LTV	linear time-varying
MNA	modified nodal analysis
PLTV	periodic linear time-varying
PSL	periodically switched linear
PWM	pulse-width modulation

Chapter 1

Introduction

In the past Years, many efforts have been spent to propose effective solutions aimed at the modeling and characterization of the electromagnetic-interference (EMI) noise emissions of switching circuits. Without loss of generality, switched mode power converters, dc motors and inverters are typical examples belonging to this classification that share the common behavior of exhibiting periodically time-varying responses arising from the internal activity of the switching components. The above feature unavoidably leads to discontinuous absorbed currents that behave as noisy EMI disturbances feeding the power distribution system and that need to be fully characterized. To this aim, it is important to find a modeling strategy that allows to predict the CE of a switching device for the systematic assessment of alternative design strategies for EMI suppression (e.g., see [27, 31]).

There are two basic approaches to model and simulate a switched circuit: the physics- and the behavioral-based methods. The physics-based modeling requires intimate knowledge of the device structure and mechanism. The CE are estimated through a time-domain simulation of the whole switching device by applying the Fourier transform to the steady-state portion of its response [28, 29, 30]. It is cumbersome to apply this method in power electronics systems, since it is difficult and time consuming to model all the devices in the system. Also, the time-domain simulation of a generic switching circuit, that exhibits a dynamical behavior with both fast and slow dynamics, is extremely inefficient and requires long CPU time to avoid integration errors and to allow the circuit responses reaching steady-state. On the other hand, the behavioral approaches are based on simplified circuits inspired from the classical Norton- or Thevenin-like linear time-invariant (LTI) structures. The reader should refer to [31, 32, 33, 34, 35, 36, 37] for a representative set of the state-of-the-art contributions. In the latter approaches some simplifications are unavoidably introduced to suppress the time-varying nature of the switches and to replace the original circuit with a time-invariant representation. Model parameters are in general computed from the observation of device responses recorded during normal operation. In turn, the obtained models can be hardly used to predict the behavior of the circuit in different design configurations (e.g., when a filter is interposed between the supply main and the converter).

To overcome the above limitations, this thesis provides an alternative approach which allows to predict the frequency-domain CE of the switched circuits. The proposed interpretation is based on the theory of the linear systems [2, 3, 5, 11, 10, 12, 17, 19] and takes into account the inherent

time-varying nature of the advocated circuits leading to better accuracy with respect to the classical methods.

This thesis is organized as follows. Chapter 2 introduces the mathematical framework needed to formally describe a time-varying system both in time- and in frequency-domain by means of a generalized version of the transfer functions and the impulse response concepts. In Chap. 3, the mathematical formulation is applied to the analysis of an example switching circuit by an augmented interpretation of the variables of the circuit and the solution of a linear system. Chapter 4 extends the standard automatic tools for the circuit analysis (e.g., the nodal analysis) to the case of switching circuits. This is achieved by substituting each elements of the switched circuit with their corresponding augmented admittance/impedance representation. In Chapter 5 the proposed technique is applied to reproduce the steady-state behavior of four switching converters both in time- and frequency-domain. Chapter 6 specializes the augmented formulation to the prediction of the CE of a dc-dc boost converter. The results are validated by a series of measurements according to the EMC standards. Finally, Chapter 7 deals with the generation of a "black box" frequency-domain model of a switching device from measured data. The proposed procedure is based on the admittance characterization of the whole circuit. The obtained predictions are validated via real measurements on a real dc-dc boost converter for different working conditions.

Chapter 2

Mathematical Background of Linear Time-Varying Systems

In this Chapter the well-known mathematical framework developed for the analysis of linear time-invariant (LTI) systems is extended to the case of linear time-varying (LTV) systems. In particular, the transfer function and the impulse response concepts are *generalized* by means of integral operators to take into account for the time-varying nature of the system.

The proposed mathematical description is then applied to the specific case of periodic linear time-varying (PLTV) systems, highlighting the main differences with respect to the LTI case. This Chapter focuses on theoretical aspects of PLTV systems, a more practical interpretation (how the theory can be applied to the circuits) will be given in the next chapters.

The Chapter is organized as follows; Section 2.1 summarizes the standard tools and properties used for the analysis of classical LTI system both in time- and in frequency-domain. In Section 2.2, the generalized transfer functions and the generalized impulse response are defined as a direct extension of the LTV case. In the last Section of this Chapter the mathematical framework developed for LTV is applied to the particular case of PLTV systems by highlighting their main properties and characteristics.

2.1 Linear Time-Invariant Case

The aim of this Section is to recall the basic notations and properties used for the analysis of classical LTI systems both in time- and frequency-domain. The *zero-state* of a generic single-input single-output LTI system [1] is defined by the following compact notation:

$$y_{\mathrm{out}}(t) = L[x_{\mathrm{in}}(t)] \tag{2.1}$$

where x_{in} and y_{out} are the input and the output signals, respectively, and L is the *operator* or *rule* accounting for the system behavior.

The system L is *linear* if and only if:

$$L[a_1 x_{\mathrm{in},1}(t) + a_2 x_{\mathrm{in},2}(t)] = a_1 L[x_{\mathrm{in},1}(t)] + a_2 L[x_{\mathrm{in},2}(t)] \tag{2.2}$$

for any coefficient a_1 and a_2 and for any input signal $x_{\mathrm{in},1}(t)$ and $x_{\mathrm{in},2}(t)$.
A generic system L is called *time-invariant* if and only if:

$$L[x_{\mathrm{in}}(t-t_0)] = y_{\mathrm{out}}(t-t_0) \tag{2.3}$$

for any real time instant t_0.

For a system defined by (2.1), the evolution of the output signal can be computed from the impulse response $h(t)$ by means of the convolution integral that writes:

$$y_{\mathrm{out}}(t) = h(t) * x_{\mathrm{in}}(t) = \int_{-\infty}^{+\infty} h(t-\tau)x_{\mathrm{in}}(\tau)d\tau \tag{2.4}$$

where $h(t) = L\left[\delta(t)\right]$, $\delta(t)$ being the Dirac's delta function.

Additionally, the well-known counterpart of (2.4) in the frequency-domain writes:

$$Y_{\mathrm{out}}(\omega) = H(\omega)X_{\mathrm{in}}(\omega) \tag{2.5}$$

where $H(\omega)$ is called *frequency-domain network function* or *transfer function* and it is obtained via the Fourier transform of the impulse response $h(t)$, i.e.,

$$H(\omega) = \int_{-\infty}^{+\infty} h(t)\exp(-j\omega t)dt. \tag{2.6}$$

2.2 Linear Time-Varying Case

This Section collects the essential theoretical results needed to extend the characterization of LTI systems to the more complex case of linear time-varying systems [2]. The discussion is aimed at presenting the notation and the main mathematical tools allowing to handle these systems.

For the sake of illustration, the example of Fig. 2.1 is considered. It shows a simple time-varying linear circuit consisting of two resistors, one capacitor and one switch (top panel) and its system representation in terms of interconnected blocks (bottom panel). From the above example, clearly, the output of the system y_{out} depends on the position of the switch S. For a fixed state of S, the output can be defined by either $h_1(t)$ or $h_2(t)$ and the standard convolution integral given by (2.4) can be used to compute the system response. To account for a possible time-varying activity of the system, equation (2.4) must be replaced by

$$y_{\mathrm{out}}(t) = \int_{-\infty}^{+\infty} h(t,\tau)x_{\mathrm{in}}(\tau)d\tau \tag{2.7}$$

where the generalized impulse response $h(t,\tau)$ is defined by $h(t,\tau) = L[\delta(t-\tau)]$ (where in a causal linear time-varying system $h(t,\tau) = 0$ for $t < \tau$) according to [2, 11]. It is relevant to

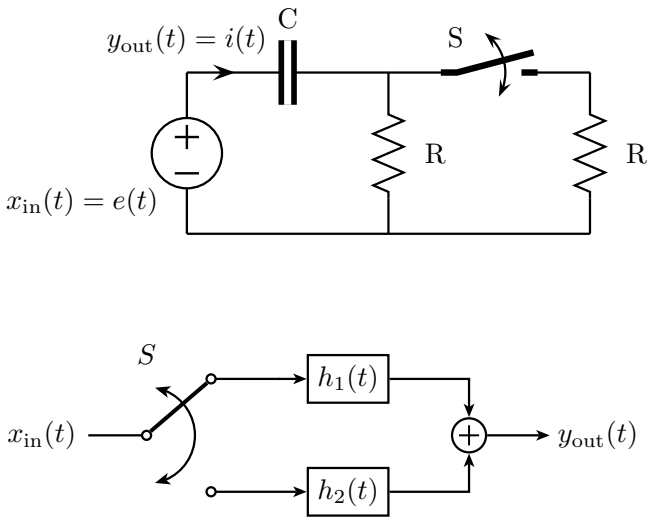

Figure 2.1: Top panel: example time-varying circuit; bottom panel: system equivalent defined in terms of two LTI blocks (namely h_1 and h_2) and one switch.

remark that in the previous equation, t plays the role of the observation time and τ represents the so-called excitation time accounting for the position of the delta function feeding the system. In other words, the excitation time is used to explore the time-varying nature of the system under different operating conditions.

In attempt to copy the success of the transfer function (2.6) of the LTI systems for the case of time-varying systems, we have to introduce the *time-varying transfer function* $H(t, \Omega)$ defined as:

$$\begin{aligned} H(t,\Omega) &= \int_{-\infty}^{+\infty} h(t,\tau)\exp(-j\Omega(t-\tau))d\tau \\ &= \int_{-\infty}^{+\infty} p(t,\hat{\tau})\exp(-j\Omega\hat{\tau})d\hat{\tau} \end{aligned} \tag{2.8}$$

where $\hat{\tau} = t - \tau$ and $p(t, \hat{\tau}) = h(t, t - \tau)$.

From (2.8) it follows that the time-varying transfer function $H(t, \Omega)$ is the Fourier transform with respect $\hat{\tau}$ of the shifted generalized impulse response $p(t, \hat{\tau})$, similar to the LTI case.

The generalized response $h(t, \tau)$ transform can be suitably derived from (2.8) by the inverse transform as follows:

$$\begin{aligned} h(t,\tau) &= \int_{-\infty}^{+\infty} H(t,\Omega)\exp(j\Omega(t-\tau))d\Omega \\ &= \int_{-\infty}^{+\infty} P(t,\Omega)\exp(j\Omega\hat{\tau})d\Omega \end{aligned} \tag{2.9}$$

For an arbitrary input the time-varying transfer function $H(t, \Omega)$ relates the output signal $y_{\text{out}}(t)$ in time-domain to the input spectrum $X_{\text{in}}(\omega)$. The relation can be proven by substituting the equation (2.9) into (2.7):

$$\begin{aligned} y_{\text{out}}(t) &= \int_{-\infty}^{+\infty} h(t,\tau)x_{\text{in}}(\tau)d\tau \\ &= \int_{-\infty}^{+\infty} \left[\frac{1}{2\pi}\int_{-\infty}^{+\infty} H(t,\Omega)\exp(j\Omega(t-\tau))d\Omega\right] x_{\text{in}}(\tau)d\tau \\ &= \frac{1}{2\pi}\int_{-\infty}^{+\infty} H(t,\Omega)\exp(j\Omega t)\left[\int_{-\infty}^{+\infty} x_{\text{in}}(\tau)\exp(-j\Omega\tau)d\tau\right] d\Omega \end{aligned} \tag{2.10}$$

where from (2.10), the integral with respect to the time-variable τ is the Fourier transform of the input signal $x_{\text{in}}(t)$, thus the previous equation can be rewritten as:

$$y_{\text{out}}(t) = \frac{1}{2\pi}\int_{-\infty}^{+\infty} H(t,\Omega)\exp(j\Omega t)X_{\text{in}}(\Omega)d\Omega. \tag{2.11}$$

At this point the time-domain response of a generic linear time-varying system $y_{\text{out}}(t)$ can be computed analytically both from the time-domain behavior of the input $x_{\text{in}}(\tau)$ by the generalized impulse response $h(t,\tau)$ and the operator (2.7) and from the frequency-domain characterization of the input X_{in} by the time-varying transfer function $H(t,\Omega)$ and the operator in (2.11).

Now, it is possible to introduce the *bi-frequency transfer function* $H(\omega,\Omega)$ and its operator which allow to describe the LTV systems completely in frequency-domain. The bi-frequency transfer function $H(\omega,\Omega)$ can be derived from the generalized impulse response $h(t,\tau)$ via the following integral:

$$H(\omega,\Omega) = \int_{-\infty}^{+\infty}\int_{-\infty}^{+\infty} h(t,\tau)\exp(-j(\omega t-\Omega\tau))dtd\tau. \tag{2.12}$$

The above equation extends the Fourier transform of the classical impulse response $h(t)$ to the two-dimensional case $h(t,\tau)$ [2]. Similarly, the generalization of (2.5) becomes:

$$Y_{\text{out}}(\omega) = \frac{1}{2\pi}\int_{-\infty}^{+\infty} H(\omega,\Omega)X_{\text{in}}(\Omega)d\Omega. \tag{2.13}$$

The bi-frequency transfer function $H(\omega,\Omega)$ can be considered as a map between the input $X_{\text{in}}(\Omega)$ and the output $Y_{\text{out}}(\omega)$, where the variables Ω and ω are the input and output frequencies, respectively.

Equation (2.13) suggests that a sinusoidal excitation with angular frequency Ω feeding the system can produce an output response characterized by a possibly richer frequency-domain behavior (i.e., Y_{out} turns out to be a function of ω). On the contrary, it is well-known that LTI systems operating in the sinusoidal steady-state at Ω produce responses characterized by the same input frequency. In the latter case, Y_{out} would consist of two delta functions located at $\omega = \pm\Omega$.

Equation (2.13) can be used in order to obtain other direct and inverse relations between generalized time-varying transfer functions and the bi-frequency transfer function as in [2].

We start applying the Fourier transform to the equation (2.11):

$$\begin{aligned} Y_{\text{out}}(\omega) &= \mathcal{F}\left[y_{\text{out}}(t)\right](\omega) \\ &= \int_{-\infty}^{+\infty}\left[\frac{1}{2\pi}\int_{-\infty}^{+\infty} H(t,\Omega)X(\Omega)\exp(j\Omega t)d\Omega\right]\exp(-j\omega t)dt \\ &= \frac{1}{2\pi}\int_{-\infty}^{+\infty} X(\Omega)\left[\int_{-\infty}^{+\infty} H(t,\Omega)\exp(j(\Omega-\omega)t)dt\right]d\Omega \\ &= \frac{1}{2\pi}\int_{-\infty}^{+\infty} H(\omega,\Omega)X_{\text{in}}(\Omega)d\Omega \end{aligned} \tag{2.14}$$

Equation (2.14) shows that the bi-frequency transfer function $H(\omega,\Omega)$ can be also computed from the time-varying transfer function $H(t,\Omega)$ via:

$$H(\omega,\Omega) = \int_{-\infty}^{+\infty} H(t,\Omega)\exp(j(\Omega-\omega)t)dt. \tag{2.15}$$

The above equations constitute the basic set of definitions needed to solve both analytically and numerically time-varying circuits. This overview also highlights the main differences between time-invariant and time-varying systems. In the latter case, the relations among the input and output variables both in time- and in frequency-domain involve more complex operators rather than simple products and convolutions. The mathematics is unavoidably more complex. However, the framework is well-established and allows us to effectively employ the readily available results to real application examples.

2.3 Periodic Linear Time-Varying Case

This Section deals with the analysis of PLTV systems by means of the generalized transfer functions described in the previous Section. A PLTV system can be seen as a particular case of the time-varying linear systems, where the parameters of the system change periodically in time (i.e. due to the effect of switches). As an example, the circuit of Fig. 2.1 can be considered a PLTV system when the position of the switch S is periodically changed between the close and the open states. It is important to remark that this class of systems represents an important subset of time-varying systems with a large number of applications in different engineering domains (well-known examples are the standard configurations of dc-dc converters as the buck, boost and buck-boost topologies).

For PLTV systems, the time-varying transfer function $H(t,\Omega)$ (2.8) turns out to be a periodic function of t that can be expanded in Fourier series, leading to [6]:

$$H(t,\Omega) = \sum_{n=-\infty}^{+\infty} H_n(\Omega)\exp(jn\omega_c t) \tag{2.16}$$

where $\omega_c = 2\pi/T$ is the fundamental angular frequency of the periodic behavior of the system (T is the characteristic period) and $H_n(\Omega)$ are new objects called *aliasing transfer functions*, defined as:

$$H_n(\Omega) = \frac{1}{T}\int_0^T H(t,\Omega)\exp(-jn\omega_c t)dt. \tag{2.17}$$

The bi-frequency transfer function for a PTVL system can be computed by substituting (2.16) into (2.15):

$$\begin{aligned} H(\omega,\Omega) &= \int_{-\infty}^{+\infty}\sum_{n=-\infty}^{+\infty} H_n(\Omega)\exp(-jn\omega_c t)\exp(j(\Omega-\omega)t)dt \\ &= 2\pi\sum_{n=-\infty}^{+\infty} H_n(\Omega)\delta(\omega-\Omega-n\omega_c). \end{aligned} \tag{2.18}$$

where, the exponential functions are converted in frequency-domain by means of the following property of the Fourier transform:

$$\int_{-\infty}^{+\infty}\exp(-j(\omega-\Omega-n\omega_c)t)dt = 2\pi\delta(\omega-\Omega-n\omega_c). \tag{2.19}$$

Hence, the output $Y_{\rm out}(\omega)$ in frequency-domain can be finally defined via (2.13) and writes:

$$\begin{aligned} Y_{\rm out}(\omega) &= \sum_{n=+\infty}^{+\infty}\int_{-\infty}^{+\infty} H_n(\Omega)\delta(\omega-\Omega-n\omega_c)X(\Omega)d\Omega \\ &= \sum_{n=-\infty}^{+\infty} H_n(\omega-n\omega_c)X_{\rm in}(\omega-n\omega_c). \end{aligned} \tag{2.20}$$

The above equation is the generalization of (2.5) for PLTV systems. This can be appreciated by observing that (2.20) is equivalent to (2.5) when $n = 0$.

In order to better understand the behavior of the considered systems, it is important to specialize the above equations for the case of a cisoidal excitation $x_{\rm in}(t) = (X_0/2\pi)\exp(j\Omega t)$. The frequency-domain response $Y_{\rm out}(\omega)$ of the system is obtained by substituting the frequency-domain description of the input signal $X_{\rm in}(\omega) = X_0\delta(\omega-\Omega)$ into (2.20), leading to:

$$Y_{\rm out}(\omega) = \sum_{n=-\infty}^{+\infty} H_n(\Omega)X_0\delta(\omega-\Omega-n\omega_c). \tag{2.21}$$

The above equation, that is the Fourier transform of a signal described by its Fourier series, can be rewritten in time-domain by means of a complex sum of trigonometric functions with angular frequencies $\Omega + n\omega_c$:

$$y_{\text{out}}(t) = \frac{1}{2\pi} \sum_{n=-\infty}^{+\infty} H_n(\Omega) X_0 \exp(j(\Omega + n\omega_c)t). \tag{2.22}$$

From the previous results it is clear that a PLTV system is completely described both in frequency- and in time-domain by the aliasing transfer functions $H_n(\Omega)$ [5, 11].

2.3.1 Formal derivation of the steady-state behavior

The discussion starts by introducing the definition of a *stationary* signal. A deterministic signal $x_{\text{in}}(t)$ is stationary if and only if it can be written as:

$$x_{\text{in}}(t) = \sum_{n=\infty}^{+\infty} X_n \exp(j\omega_n t) \tag{2.23}$$

where X_n are complex coefficients and ω_n are real numbers. Signals of the form of $x_{\text{in}}(t)$ are called *almost periodic* signals.

A stationary system is a system that for every deterministic stationary input signals delivers a stationary deterministic output. A system reaches the steady-state condition, when the output signal is considered for an harmonic excitation after the transient has vanished. For the sake of illustration let us consider the response of a stationary system to a cisoidal excitation $x_{\text{in}}(t) = \exp(j\Omega t)$ of angular frequency Ω:

$$y_{\text{out}}(t) = \sum_{n=-\infty}^{+\infty} P_n(\Omega) \exp(j\omega_n(\Omega)t) \tag{2.24}$$

where $P_n(\Omega)$ and $\omega_n(\Omega)$ are functions determined by the system.

Using the linearity of the system, the response of the system $y_{\text{out}}(t)$ to a generic excitation can be written by using the spectrum $X_{\text{in}}(\omega)$ of a generic input signal $x_{\text{in}}(t)$ as follows:

$$y_{\text{out}}(t) = \frac{1}{2\pi} \int_{-\infty}^{+\infty} \sum_{n=-\infty}^{+\infty} P_n(\Omega) \exp(j\omega_n(\Omega)t) X_{\text{in}}(\Omega) d\Omega \tag{2.25}$$

Comparing (2.25) with the corresponding relation shown in (2.11), we find that:

$$H(t, \Omega) = \sum_{n=-\infty}^{+\infty} P_n(\Omega) \exp(j\omega_n(\Omega)t) \tag{2.26}$$

hence the bi-frequency transfer function of a generic stationary system is defined by:

$$H(\omega, \Omega) = 2\pi \sum_{n=-\infty}^{+\infty} P_n(\Omega) \delta(\omega - \omega_n(\Omega)) \tag{2.27}$$

Equation (2.27) shows that the harmonic components of the response of a stationary system are defined via the projections of the functions $\omega_n(\Omega)$ on the frequency variable ω.

The generic input-output relations (2.26) and (2.27) for a generic stationary system become the input-output relations (2.16) and (2.18) developed for PLTV system by defining the function $\omega_n(\Omega)$ as follows:

$$\omega_n(\Omega) = \Omega + n\omega_c. \tag{2.28}$$

where ω_c is the angular frequency related to the periodic activity of the system.

The last equation proofs that the PLTV systems are stationary systems, in fact after the transient all the variables of the system are stationary signals that can be represented by their Fourier expansion (2.29) as shown in (2.21). Hence at the steady-state, the response of a generic PLTV system to a cisoidal excitation of angular frequency Ω can be rewritten as follows:

$$y_{\text{out}}(t) = \sum_{n=-\infty}^{+\infty} Y_n(\Omega) \exp(j(\Omega + n\omega_n)t) \tag{2.29}$$

2.3.2 Interpretation in terms of LTI subsystems

Equation (2.22) suggests a more intuitive interpretation of the PLTV systems in terms of an infinite number of LTI systems as shown in Fig. 2.2.

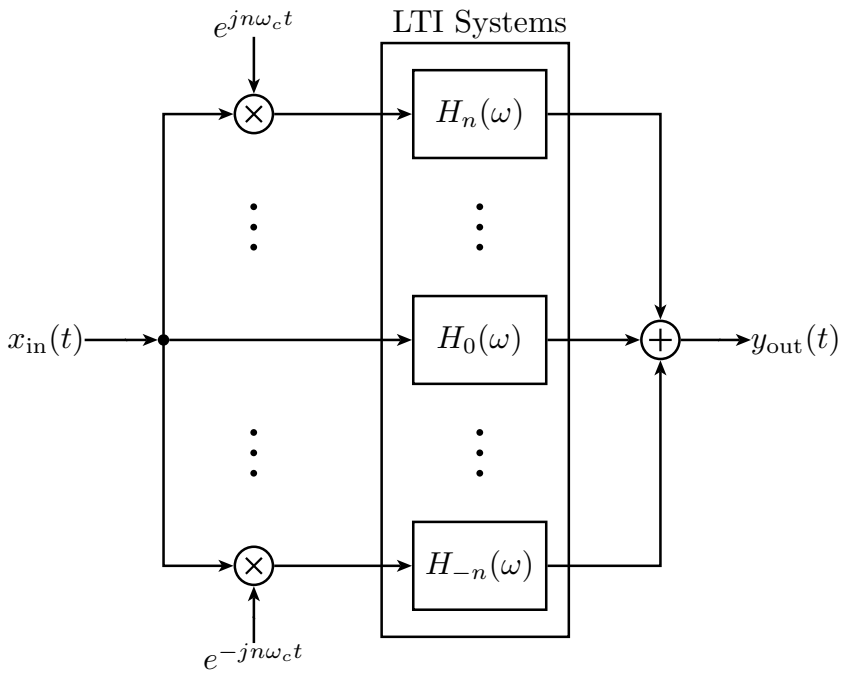

Figure 2.2: Canonical block-diagram interpretation of a genetical PLTV system in term of an infinite number of LTI systems.

According to Fig. 2.2 the response $y_{\mathrm{out}}(t)$ of a PLTV system is the superposition of the responses of an infinite number of LTI systems defined by the aliasing transfer functions $H_n(\omega)$. It is worth nothing that different from the classical LTI systems the block-diagram includes also an infinite number of mixer elements. The frequency mixers shift the frequency range of the excitation of the system $x_{\mathrm{in}}(t)$ generating new harmonics in the spectrum of the response $y_{\mathrm{out}}(t)$ as shown in Fig. 2.3 at multiples of the angular switching frequency ω_c.

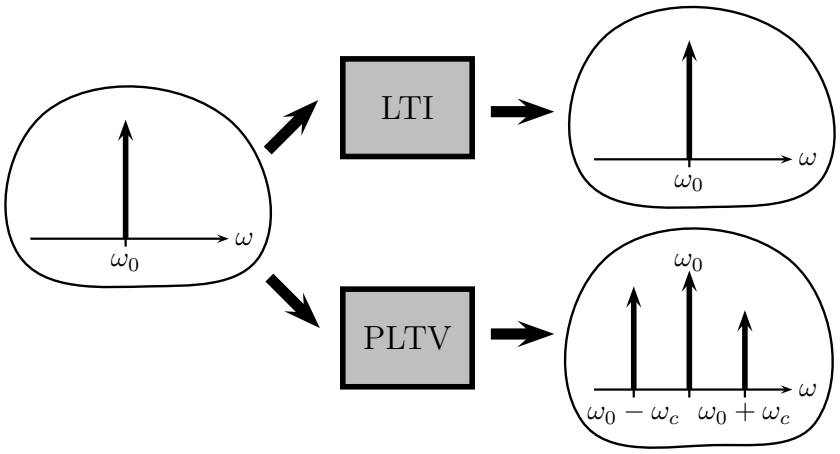

Figure 2.3: Schematic allowing a graphical interpretation of the response of LTI and PLTV system to a single tone excitation of angular frequency ω_0.

2.4 Chapter Summary

This Chapter briefly introduces the basic notation used hereafter in this thesis to analyze and to model the steady-state behavior of the LPTV systems both in time- and frequency-domain. According to the theory of LTV systems and [2], both the frequency- and the time-domain behavior of the latter systems is provided by the generalized transfer functions and their corresponding integral operators, that extend the well-known concept of the standard transfer function used for the case of LTI systems.

Chapter 3

Steady-State Analysis of Switching Circuits

This Chapter focuses on the analysis of a particular class of PLTV systems called periodically switched linear (PSL) systems or circuits by means of the mathematical framework developed in the previous Chapter. A generic PSL circuit is the interconnection of classical LTI elements (i.e., resistors, capacitors, inductors, independent voltage sources, etc..) and switches characterized by a periodic behavior. The switches are the PLTV elements of the circuit and are defined by means of generalized transfer functions. Therefore, similarly to the impedance and admittance representations developed for the classical LTI elements, the frequency-domain voltage-current characteristic of a time-varying switch is given via its bi-frequency admittance or impedance *operator*. Due to the presence of integral operators, the analysis of PSL circuits requires the solution of *integral equations* that are clearly more complicated than the products and convolutions operations used to solve LTI circuits both in frequency- and in time-domain.

Two examples are considered to show how resistive and dynamical circuits containing switching elements can be solved directly in frequency-domain by means of the proposed approach based on generalized transfer functions.

This Chapter is organized as follows. In Section 3.1, the analytical solution of a simple PSL resistive example is illustrated to understand the effects of switches on the current and the voltage variables of the circuit both in time- and frequency-domain. The analytical solution is also used to derive the bi-frequency admittance representation of a memoryless PSL circuit. The results obtained from the analysis of the simple resistive circuit are used to define the *generalized Ohm's law* of a generic time periodical switch element by the bi-frequency admittance or impedance characterization. The last Section 3.4 focuses on the solution of dynamical PSL circuits containing switches that are described by their bi-frequency admittance or impedance operator. As mentioned before, the solution of this kind of circuits involves integral equations and allows to directly compute the steady-state responses of the currents and voltages of the circuit both in time- and frequency-domain.

3.1 PSL Resistive Elements

Let us to consider the schematic of Fig. 3.1(a) with the aim of justifying the formulas collected in Chapter 2 and to stress the features of PSL circuits. The discussion starts by considering the circuit as the interconnection of an ideal voltage source and a resistive PSL component characterized by its bi-frequency admittance as shown in Fig. 3.1(b).

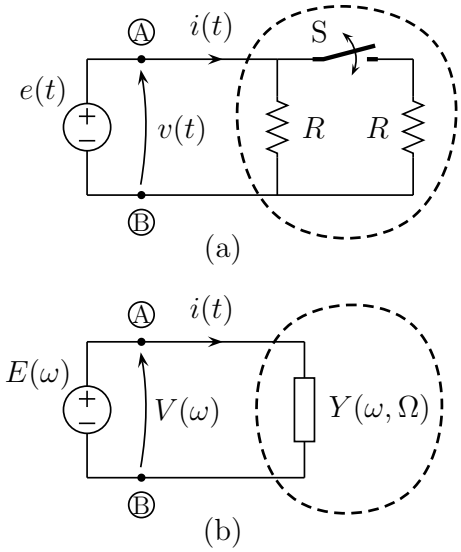

Figure 3.1: Top panel: example circuit consisting of the interconnection of an ideal voltage source and of a switching resistive PSL block. Bottom panel: circuit with the PSL block described by means of its generalized bi-frequency admittance $Y(\omega, \Omega)$.

The resistive switching element is characterized by a periodic switching activity between the open and the close position with a characteristic period T. The switch is assumed to be closed in the first half part of the period (e.g., $t \in [0, T/2]$) and open in the remaining part.

3.1.1 Bi-frequency admittance representation

According to the definition of the bi-frequency transfer function, the bi-frequency admittance $Y(\omega, \Omega)$ for the PSL element of Fig. 3.1(b) can be defined as a map between the frequency-domain current responses $I(\omega)$ and a single tone voltage excitations $E(\omega)$ of angular frequency Ω. The independent voltage source $e(t)$ is defined in time-domain by a cisoidal signal:

$$e(t) = (E_0/2\pi)\exp(j\Omega t). \tag{3.1}$$

Since the switching block does not include dynamical elements, the port current $i(t)$ can be alternatively interpreted as the juxtaposition in time of the current response computed from the analysis of the circuit of Fig. 3.1 at each operating state of the switch (i.e., open and close). Hence, the current $i(t)$ writes:

$$i(t) = \frac{E_0}{2\pi}\exp(j\Omega t)\cdot\left[\underbrace{G_1\sum_{n=-\infty}^{+\infty}\Pi_{\frac{T}{2}}(t-nT)}_{w(t)} + G_2\sum_{n=-\infty}^{+\infty}\Pi_{\frac{T}{2}}\left(t-nT-\frac{T}{2}\right)\right] \tag{3.2}$$

where, $G_1 = 2/R$ and $G_2 = 1/R$ are the equivalent conductances of the PSL two-terminal element when the switch is close or open, respectively, and $\Pi_\Delta(t-t_0)$ is the window function defined by:

$$\Pi_\Delta(t-t_0) = \begin{cases} 1 & t_0 \le t \le \Delta + t_0 \\ 0 & \text{otherwise} \end{cases} \tag{3.3}$$

According to the properties of the Fourier transform, the current $i(t)$ of equation (3.2) can be written in frequency-domain via the following convolution:

$$I(\omega) = E(\omega) * W(\omega)\left(G_1 + G_2\exp\left(j\omega\frac{T}{2}\right)\right) \tag{3.4}$$

where $E(\omega) = E_0\delta(\omega-\Omega)$ is the Fourier transform of the voltage excitation $e(t)$ and $W(\omega) = \sum_{n=-\infty}^{+\infty} f_c c_n \delta(\omega - n\omega_c)$ is the discrete spectrum of the periodic window function $w(t)$.

Applying the convolution integral operator defined by (2.4), we get the following spectrum:

$$I(\omega) = \sum_{n=-\infty}^{+\infty} f_c c_n\left(G_1 + G_2\exp\left(jn\omega_c\frac{T}{2}\right)\right)E_0\delta\left(\omega-\Omega-n\omega_c\right) \tag{3.5}$$

where $f_c = 1/T$ and c_n are the coefficients of the Fourier series expansion of the periodic function $w(t) = \sum_{n=-\infty}^{+\infty}\Pi_{\frac{T}{2}}(t-nT)$:

$$\begin{aligned} c_n &= \int_{t_0}^{t_0+\Delta} 1\exp(-jn\omega_c t)dt \\ &= \int_0^{T/2} 1\exp(-jn\omega_c t)dt \\ &= \frac{1-\exp(-jn\omega_c T/2)}{jn\omega_c}. \end{aligned} \tag{3.6}$$

Different from the LTI case, the current response of (3.5) shows as the response of a PSL circuit to a single tone excitation of frequency Ω contains an infinite number of harmonics at frequency $\Omega + n\omega_c$.

It is important to notice that (3.5) is equivalent to the generic equation (2.20), where a single-frequency excitation $E(\omega) = E_0\delta(\omega-\Omega)$ is considered ($E(\omega)$ being the Fourier transform of the input cisoidal signal).

Equations (2.20) and (3.5) allow to define the aliasing transfer functions $Y_n(\Omega)$ for the pure resistive circuit of Fig. 3.1(a) as:

$$Y_n \;=\; f_c c_n \left(G_1 + G_2 \exp\left(jn\omega_c \frac{T}{2} \right) \right). \tag{3.7}$$

In this example, the functions $H_n = Y_n$ do not depend on the variable Ω since the circuit in each operating state is resistive and its solution involves instantaneous relations only. According to (2.18), the generalized bi-frequency admittance can be written as:

$$Y(\omega, \Omega) \;=\; 2\pi \sum_{n=-\infty}^{+\infty} Y_n \cdot \delta\left(\omega - \Omega - n\omega_c\right). \tag{3.8}$$

Figure 3.2 shows the magnitude of the 2 variables function $Y(\omega, \Omega)$ defined by (3.8) and computed for $R = 100\,\Omega$ and $f_c = 10\,\text{kHz}$. To improve the readability of the plot, the $\Omega-$axis is discretized and four samples are considered only. This figure allows to get a practical interpretation of the transfer function of a time-varying system. Due to the term $\delta(\omega - \Omega - n\omega_c)$ in (2.18), the cut of the two-dimensional surface $Y(\omega, \Omega)$ for a fixed Ω value turns out to be given by the superposition of delta functions occurring at frequencies $\Omega + n\omega_c$ (n=..., $-1, 0, 1, ...$). Clearly, the position of such deltas on the $\omega-$axis are shifted to the right (or to the left) when the values of the input frequencies Ω increase (or decrease).

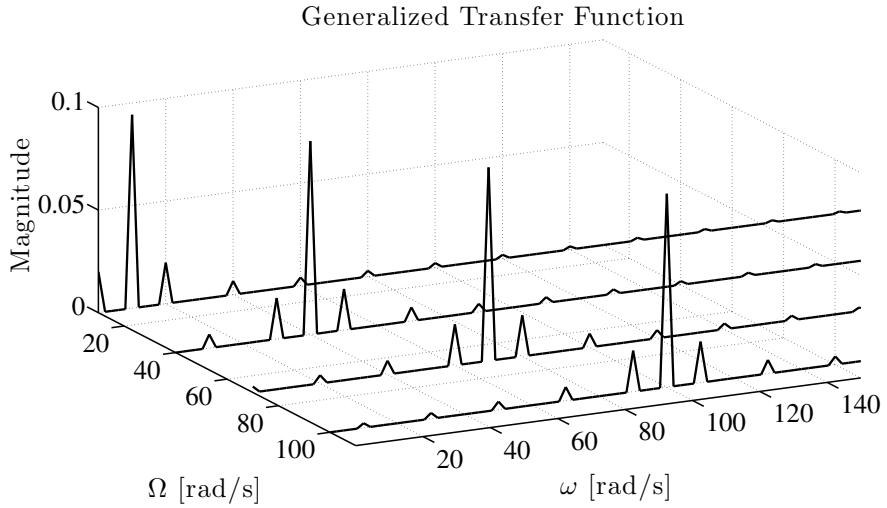

Figure 3.2: Bi-frequency generalized admittance $H(\omega, \Omega)$ associated to the example circuit of Fig. 3.1.

It is relevant to notice that the proposed procedure can be applied to multiport resistive elements as well, provided that their port admittance characteristic can be computed as for the example two-terminal element of Fig. 3.1 [19]. In practice, voltage sources are applied to the different ports of the multiport and the current responses are interpreted as the juxtaposition in time of

the port current responses computed for the different operating states of the switches, leading to matrix relations similar to (3.5).

3.1.2 Current response to a generic voltage excitation

Similar to the classical LTI admittance $Y(\omega)$, the bi-frequency admittance $Y(\omega, \Omega)$ allows to compute the steady-state current response of a switching element for a generic periodical voltage excitation via the integral operator introduced in (2.13).

For the sake of illustration, the advocated integral operator is used to compute the current response $I(\omega)$ of the simple PSL circuit in Fig. 3.1(b) to a sinusoidal voltage excitation $e(t) = E_0 \sin(2\pi f_0 t)$:

$$I(\omega) = \frac{1}{2\pi} \int_{-\infty}^{+\infty} Y(\omega, \Omega) E(\Omega) d\Omega, \tag{3.9}$$

the above equation is the *generalized Ohm's law* for a linear time-varying element.

For the case of a generic resistive PSL element, equation (3.9) can be written by considering the bi-frequency admittance $Y(\omega, \Omega)$ of (3.8), as follows:

$$\begin{aligned} I(\omega) &= \int_{-\infty}^{+\infty} \sum_{n=-\infty}^{+\infty} Y_n \delta\left(\omega - \Omega - n\omega_c\right) \frac{E_0}{j2\pi} \left[\delta(\Omega - \omega_0) - \delta(\Omega + \omega_0)\right] d\Omega \\ &= \frac{E_0}{j2\pi} \sum_{n=-\infty}^{+\infty} Y_n \left[\delta(\omega - \omega_0 - n\omega_c) - \delta(\omega + \omega_0 - n\omega_c)\right]. \end{aligned} \tag{3.10}$$

where $E(\omega) = \frac{E_0}{j2\pi} \left[\delta(\omega - \omega_0) - \delta(\omega + \omega_0)\right]$ is the spectrum of the sinusoidal voltage excitation of angular frequency $\omega_0 = 2\pi f_0$.

The above equation highlights that the steady-state current response $I(\omega)$ of a PSL system to a two-harmonic voltage excitation $E(\omega)$ at angular frequencies $\pm\omega_0$, contains an infinite number of components at frequencies $\pm\omega_0 + n\omega_c$ (for $n = \ldots, -1, 0, 1, \ldots$).

The time-domain steady-state response of the current can be easily computed by applying the inverse Fourier transform to the equation (3.14):

$$i(t) = E_0 \sum_{n=-\infty}^{+\infty} Y_n \exp\left(jn\omega_c t\right) \left(\frac{\exp(j\omega_0 t) - \exp(-j\omega_0 t)}{2j}\right). \tag{3.11}$$

Figure 3.3 shows the time-domain current response $i(t)$ of the circuit of Fig. 3.1 to a sinusoidal excitation of frequency $f_0 = 100\,\text{kHz}$ and amplitude $E_0 = 10\,\text{V}$ and its corresponding frequency-domain spectrum.

It is important to remark that the linear property of the PSL system allows to extend the proposed results to the case of a generic stationary excitation $e(t)$:

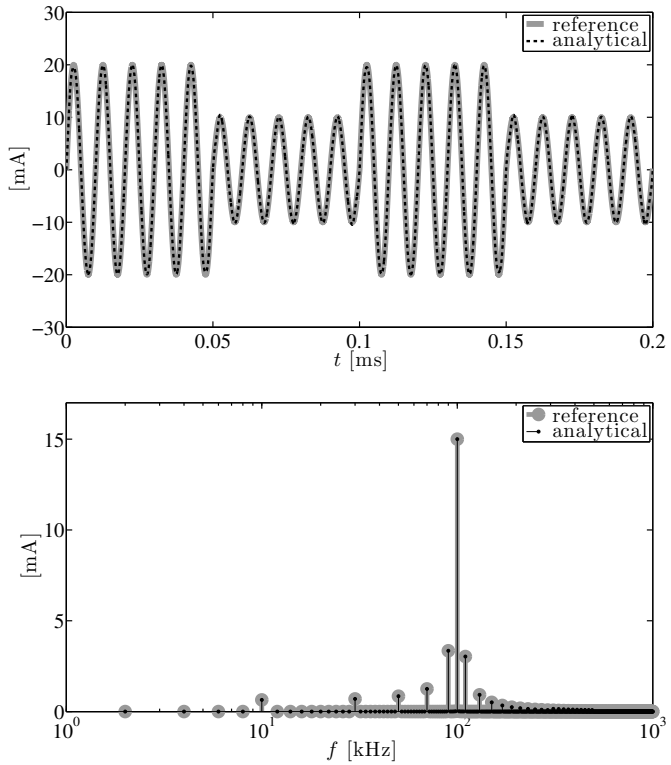

Figure 3.3: Time-domain response of the current $y(t)$ of the circuit of Fig. 3.1 (top panel) and its corresponding spectrum $Y(f)$ (bottom panel).

$$e(t) = \sum_{m=-\infty}^{+\infty} E_m \exp(j\omega_m t) \tag{3.12}$$

where the corresponding spectrum is defined via the following infinite sum of Dirac's functions:

$$E(\omega) = \sum_{m=-\infty}^{+\infty} \frac{E_m}{2\pi} \delta(\omega - \omega_m). \tag{3.13}$$

In this case, the spectrum of current response $I(\omega)$ is obtained by applying the integral operator (3.9) to the above voltage excitation $E(\omega)$ as follows:

$$\begin{aligned} I(\omega) &= \int_{-\infty}^{+\infty} \sum_{n=-\infty}^{+\infty} Y_n \delta\left(\omega - \Omega - n\omega_c\right) \sum_{m=-\infty}^{+\infty} \frac{E_m}{2\pi} \delta(\Omega - \omega_m) d\Omega \\ &= \sum_{n=-\infty}^{+\infty} \sum_{m=-\infty}^{+\infty} \frac{E_m}{2\pi} Y_n \delta(\omega + \omega_m - n\omega_c). \end{aligned} \tag{3.14}$$

The linearity property of the integral operator allows to compute the current response $I(\omega)$ of the PSL circuit to a multi-tone excitation $E(\omega)$ by means of the *superposition theorem*, as the sum of the responses of the system to a series of cisoidal excitations.

Hence, the corresponding steady-state time-domain current response $i(t)$ writes:

$$i(t) = \sum_{n=-\infty}^{+\infty} Y_n \exp(jn\omega_c t) \sum_{m=-\infty}^{+\infty} E_m \exp(j\omega_m t). \tag{3.15}$$

The above equations clearly illustrate the mechanism of harmonic generation characteristic of the linear time-varying circuit. In fact, the time-varying behavior of the circuit generates new harmonics even if circuit does not contain active elements (i.e., the circuit of Fig. 3.1 has an ideal voltage source connected to a passive two-terminal switching resistive element).

3.2 Solution via Kirchhoff's Laws

In this section the mathematical framework developed for the case of linear time-varying systems is used to obtain the time- and in frequency-domain steady-state response of a dynamical PSL circuit containing the PSL block defined in the previous example. The considered circuit shown in Fig. 3.4(a) is composed of two parts: the LTI block (on the left) and the resistive PSL block (on the right). The LTI part of the circuit is a non-ideal voltage source that consists of the interconnection of an ideal independent voltage source $e(t)$ connected to an inductor L and a resistor R_L with a parallel capacitor C and its series resistor R_C. From a practical point of view, the circuit can be considered as the connection between a linear filter (part on the left) and a bi-frequency admittance $Y(\omega, \Omega)$ that is used to replace the time-varying block, as in the schematic of Fig. 3.4(b).

Without loss of generality the following analysis focuses on the computation of the behavior of the voltage v_{AB} for a cisoidal voltage excitation $e(t) = E_0 \exp(j\omega_0 t)$.

The discussion starts by applying the classical Kirchhoff's laws to the circuit of Fig. 3.4(b):

$$\begin{cases} E(\omega) = I(\omega)Z_s(\omega) + V_{AB}(\omega) \\ I(\omega) = I_p(\omega) + I_A(\omega) = Y_p(\omega)V_{AB}(\omega) + I_A(\omega). \end{cases} \tag{3.16}$$

Equation (3.16) does not contain any information about the time-varying behavior of the considered circuit, in fact the time-varying behavior of the PSL block has to be included into the v_{AB}-i_A relation via the *generalized Ohm's law* as follows:

$$V_{AB}(\omega) = \frac{1}{2\pi} \int_{-\infty}^{+\infty} Z(\omega, \Omega) I_A(\Omega) d\Omega \tag{3.17}$$

$$I_A(\omega) = \frac{1}{2\pi} \int_{-\infty}^{+\infty} Y(\omega, \Omega) V_{AB}(\Omega) d\Omega \tag{3.18}$$

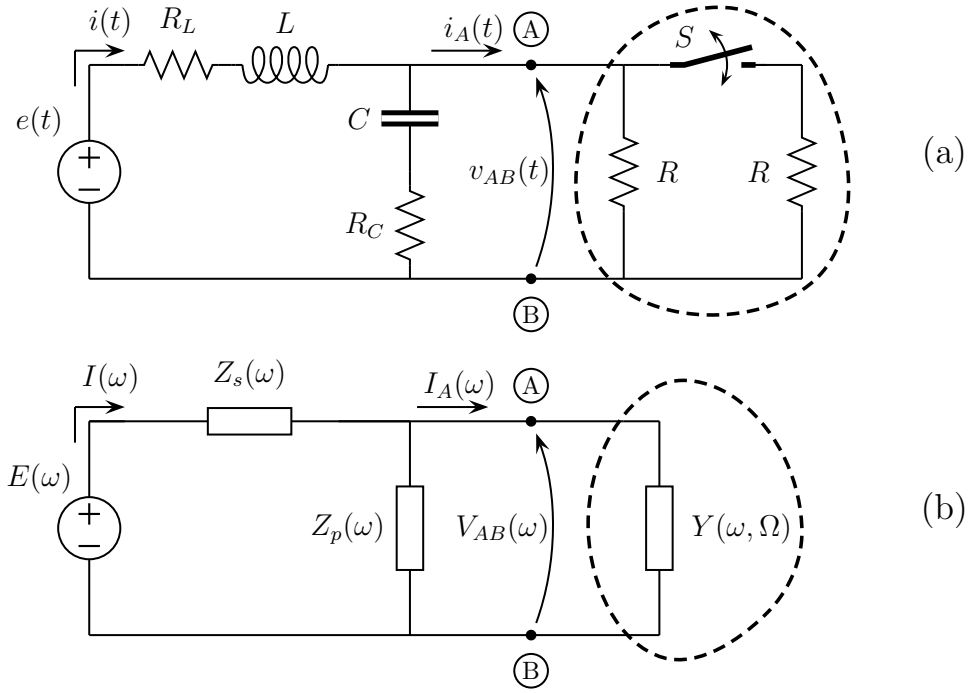

Figure 3.4: Example circuit consisting of a PSL resistive circuit connected to an LTI non-ideal source (panel(a)); frequency-domain interpretation of the circuit where the PSL block is replaced by its bi-frequency admittance representation $Y(\omega, \Omega)$ (panel(b)).

where $Z(\omega, \Omega)$ and $Y(\omega, \Omega)$ are the so called bi-frequency impedance and admittance of the PSL block. Due to the presence of the integral operator the classical relation $Y(\omega) = 1/Z(\omega)$ defined for LTI systems is not valid.

Substituting (3.18) into (3.16), the equation can be written in terms of the unknown voltage V_{AB}, the bi-frequency admittance $Y(\omega, \Omega)$, the LTI impedances $Z_s(\omega)$ and admittance $Y_p(\Omega)$ and the voltage excitation $E(\omega)$.

$$V_{AB}(\omega) = E(\omega) - Z_s(\omega) \left[Y_p(\omega) V_{AB}(\omega) + \frac{1}{2\pi} \int_{-\infty}^{+\infty} Y(\omega, \Omega) V_{AB}(\Omega) d\Omega \right] \tag{3.19}$$

where $Y_p(\omega) = 1/(R_C + 1/j\omega C)$ and $Z_s(\omega) = R_L + j\omega L$.

The integral equation (3.19) is in the form of a *Fredholm integral equation*, that comes from the generalization of the Kirchhoff's laws for the PSL circuit of Fig. 3.4(b). It is important to stress that up to now, the periodicity of the the time-varying element is not taken into account, in fact the generalized Ohm's laws of (3.17) and (3.18) allow to characterize each kinds of LTV element. The integral equation (3.19) can be simplified by considering the time-domain periodic behavior of the linear time-varying block.

From Chap. 2 we know two important features of the PLTV circuits:

1. the bi-frequency transfer function $H(t, \Omega)$ is a periodic function (see Sec. 2.3.1), thus the bi-frequency admittance can be written by its Fourier series in the following form:

$$Y(\omega,\Omega) = 2\pi \sum_{n=-\infty}^{+\infty} Y_n(\Omega)\delta(\omega - n\omega_c - \Omega) \tag{3.20}$$

where the aliasing admittances $Y_n(\Omega)$ depends on PLTV element of the circuit (e.g., see the example of Sec. 3.1).

2. all the variables of a PLTV system at the steady-state can be expressed in terms of their Fourier series expansion. This means that at the steady-state all the voltages and the currents of a PSL circuit can be written as the sum of periodic functions. Hence in the considered example, the voltage $V_{AB}(\omega)$ and the current $I_A(\omega)$ for a voltage excitation $E(\omega) = E_0\delta(\omega - \omega_0)$ can be written in frequency-domain as follows:

$$V_{AB}(\omega) = \sum_{n=-\infty}^{+\infty} V_n\delta(\omega - n\omega_c - \omega_0) \tag{3.21}$$

$$I_A(\omega) = \sum_{n=-\infty}^{+\infty} I_n\delta(\omega - n\omega_c - \omega_0) \tag{3.22}$$

where $\omega_c = 2\pi/T$ and T is the switching period of the PSL circuit.

The aforementioned properties of a PSL circuit will allow to replace the integral equation (3.19), with a simple system of linear equations.

Let us start by substituting the steady-state frequency-domain relation between the voltage $V_{AB}(\omega)$ and the current $I_A(\omega)$ across and through the PSL element in (3.21) and (3.22) into the generalized Ohm's law (3.18):

$$\begin{aligned} I_A(\omega) &= \sum_{n=-\infty}^{+\infty} I_n\delta(\omega - n\omega_c - \omega_0) = \frac{1}{2\pi}\int_{-\infty}^{+\infty} Y(\omega,\Omega)V_{AB}(\Omega)d\Omega = \\ &= \int_{-\infty}^{+\infty} \sum_{m=-\infty}^{+\infty} Y_m\delta(\omega - m\omega_c - \Omega) \sum_{k=-\infty}^{+\infty} V_k\delta(\Omega - k\omega_c - \omega_0)d\Omega = \\ &= \sum_{k=-\infty}^{+\infty}\sum_{m=-\infty}^{+\infty} V_kY_m\delta(\omega - (m+k)\omega_c - \omega_0) \end{aligned} \tag{3.23}$$

thus:

$$\sum_{n=-\infty}^{+\infty} I_n\delta(\omega - n\omega_c - \omega_0) = \sum_{k=-\infty}^{+\infty}\sum_{m=-\infty}^{+\infty} V_kY_m\delta(\omega - (m+k)\omega_c - \omega_0) \tag{3.24}$$

It is important to notice that the periodic behavior of the system and the convenient interpretation of voltages and currents in terms of their series expansions allow to replace the integral operator with the products of two sums. Substituting the equations (3.21), (3.22) and (3.24) into the Fredholm integral equation (3.19), we obtain the following equation:

$$\begin{aligned}\sum_{n=-\infty}^{+\infty} V_n\delta(\omega - n\omega_c - \omega_0) &= E_0\delta(\omega-\omega_0) - Z_s(\omega)\left[Y_p(\omega)\sum_{n=-\infty}^{+\infty} V_n\delta(\omega - n\omega_c - \omega_0) + \right.\\ &\left. + \sum_{k=-\infty}^{+\infty}\sum_{m=-\infty}^{+\infty} V_kY_m\delta(\omega-(m+k)\omega_c-\omega_0)\right] \end{aligned} \tag{3.25}$$

The n-th component of the voltage V_n for $n \neq 0$ is defined by equation (3.25) as:

$$V_n = -Z_s(\omega_0 + n\omega_c)Y_p(\omega_0+n\omega_c)V_n - Z_s(\omega_0+n\omega_c)\sum_{k+m=n} V_kY_m \tag{3.26}$$

or better as:

$$\begin{aligned} &V_n + Z_s(\omega_0+n\omega_c)Y_p(\omega_0+n\omega_c)V_n + Z_s(\omega_0+n\omega_c)Y_0V_n + \\ &+Z_s(\omega_0+n\omega_c)\sum_{k+m=n}^{m\neq 0} V_kY_m = 0 \end{aligned} \tag{3.27}$$

Instead, for $n = 0$ the forcing term E_0 appears thus the equation (3.25) becomes:

$$\begin{aligned} V_0 + Z_s(\omega_0)Y_p(\omega_0)V_0 + Z_s(\omega_0)Y_0V_0 + & \\ +Z_s(\omega_0)\sum_{k+m=0}^{m\neq 0} V_kY_m &= E_0 \end{aligned} \tag{3.28}$$

Equations (3.27) and (3.28) show that the unknown voltage coefficients V_n are defined by a linear combination of the admittance aliasing functions Y_n and the impedances $Z_p(\omega)$ and $Z_s(\omega)$ of the filter.

For practical reasons, the infinite series in (3.21) and in (3.22) are truncated and N is the total number of both positive and negative harmonics thus:

$$V_{AB}(\omega) \approx \sum_{n=-N}^{+N} V_n\delta(\omega - n\omega_c - \omega_0) \tag{3.29}$$

$$I_A(\omega) \approx \sum_{n=-N}^{+N} I_n\delta(\omega - n\omega_c - \omega_0). \tag{3.30}$$

The truncation allows to rewrite the Fredholm's integral equation (3.19) as a simple *linear system* as following:

$$\mathbf{TV} = \mathbf{E} \tag{3.31}$$

where $\mathbf{T}$ is a $(2N+1) \times (2N+1)$ matrix depending on the structure of the circuit, $\mathbf{V}$ is a vector collecting the unknown voltage coefficients of dimension $(2N+1)$ and $\mathbf{E}$ is a vector of dimension $(2N+1)$ containing the voltage source of the circuit.

The vector $\boldsymbol{V}$ containing the unknown coefficients V_n is defined as follows:

$$\boldsymbol{V} = \begin{bmatrix} V_{-N} \\ \vdots \\ V_0 \\ \vdots \\ V_N \end{bmatrix} \tag{3.32}$$

The matrix $\boldsymbol{T}$ of the considered example circuit in Fig. 3.4 is defined by (3.27) and (3.28) as:

$$\boldsymbol{T} = \begin{bmatrix} \vdots & \ddots & \vdots & \vdots & \vdots & \vdots & \vdots \\ \cdots & \beta_1 & \Lambda_{-1} & \beta_{-1} & \beta_{-2} & \beta_{-3} & \cdots \\ \cdots & \beta_2 & \beta_1 & \Lambda_0 & \beta_{-1} & \beta_{-2} & \cdots \\ \cdots & \beta_3 & \beta_2 & \beta_1 & \Lambda_1 & \beta_{-1} & \cdots \\ \vdots & \vdots & \vdots & \vdots & \vdots & \ddots & \vdots \\ \cdots & \beta_{N-5} & \beta_{N-4} & \beta_{N-3} & \beta_{N-2} & \beta_{N-1} & \Lambda_N \end{bmatrix} \tag{3.33}$$

where the frequency-dependent coefficients are: $\beta_n = Y_n Z_s(\omega_0 + n\omega_c)$ and $\Lambda_n = 1 + Z_s(\omega_0 + n\omega_c)Y_p(\omega_0 + n\omega_c) + Y_0 Z_s(\omega_0 + n\omega_c)$. The matrix $\boldsymbol{T}$ is an hermitian complex *Toeplitz* matrix, thus $\boldsymbol{T} = \boldsymbol{T}^H$.

The vector $\boldsymbol{E}$ is related to a delta excitation in frequency-domain of the circuit therefore it is different from zero only for the $N+1$-th term:

$$\boldsymbol{E} = \begin{bmatrix} 0 \\ \vdots \\ 0 \\ E_0 \\ 0 \\ \vdots \\ 0 \end{bmatrix}. \tag{3.34}$$

The coefficients V_n are computed via the solution of the linear system of equation in (3.31) and the discrete voltage spectrum $V_{AB}(\omega)$ is directly defined by (3.21).

The time-domain voltage response $v_{AB}(t)$ is obtained by its Fourier series expansion [11], as follows:

$$v_{AB}(t) = \sum_{n=-\infty}^{+\infty} V_n \exp(j(n\omega_c + \omega_0)t) \tag{3.35}$$

Now, all the variables of the circuit of Fig. 3.4(b) can be evaluated by means of the voltage $V_{AB}(\omega)$, according to the classical laws used for the analysis of LTI circuits (the solution does not involve integral operators). The advocated approach can be used to solve generic PSL circuits where the LTI blocks are connected to a the time-varying elements composed by memoryless elements and switches.

It is important to remark that PSL circuits are the extension of the well-known LTI circuits, e.g., when the switch element of the example circuit of Fig. 3.4(a) is replaced with a simple resistor of conductance Y_0 the system of (3.31) becomes the following *scalar* relation:

$$\Lambda_0 V_0 = E_0 \tag{3.36}$$

The above scalar relation shows as the response of an LTI circuit does not present any frequency coupling since the spectrum of the response V_0 can *only* contain the same harmonics of the system excitation E_0.

3.3 Numerical Results

This Section deals with two numerical validations of the proposed frequency-domain mathematical analysis of the PSL circuit of Fig. 3.4. The time- and frequency-domain behaviors of the voltage v_{AB} obtained via the proposed method are compared with the results of classical time-domain MATLAB simulations in Simulink environment, for two different voltage excitations $e(t)$. The PSL block is characterized by a switching period $T = 0.1$ ms where the switch S is closed in the first half part $t_{close} = 0.5 \times T$ and by two resistors $R = 100\,\Omega$. The remaining parameters of the circuit are the following: $R_L = 100\,\Omega$, $L = 1$ mH, $R_C = 10\,\Omega$ and $C_p = 1$ nF.

Figure 3.5 shows the time- and frequency-domain responses of the voltage v_{AB} of the circuit to a DC voltage excitation $e(t) = 10$ V (a constant excitation is seen in frequency-domain as a cisoidal signal with an angular frequency $\omega_0 = 0$ rad/s, thus $E(\omega) = 10/(2\pi)\delta(\omega)$).

As a second validation, Fig. 3.6 shows the voltage response v_{AB} computed both in time- and frequency-domain for a sinusoidal voltage excitation $e(t) = 10\sin(2\pi f_0 t)$, where $f_0 = 50$ kHz.

The results show a perfect agreement between the steady-state solutions of voltage v_{AB} obtained by the proposed mathematical description with the reference curves. It also worth remarking that the proposed method is completely independent from the time-step used in time-domain simulation since it is based on a frequency-domain formulation of the circuit. The analysis provides directly both the time- and frequency-domain behaviors of the voltage v_{AB} in 0.14 s simply by solving the linear system of (3.31) without employing the FFT or the IFFT routines. The simulation time is related to the dimensions of the matrix $\mathbf{T}$, thus on the total number of harmonics

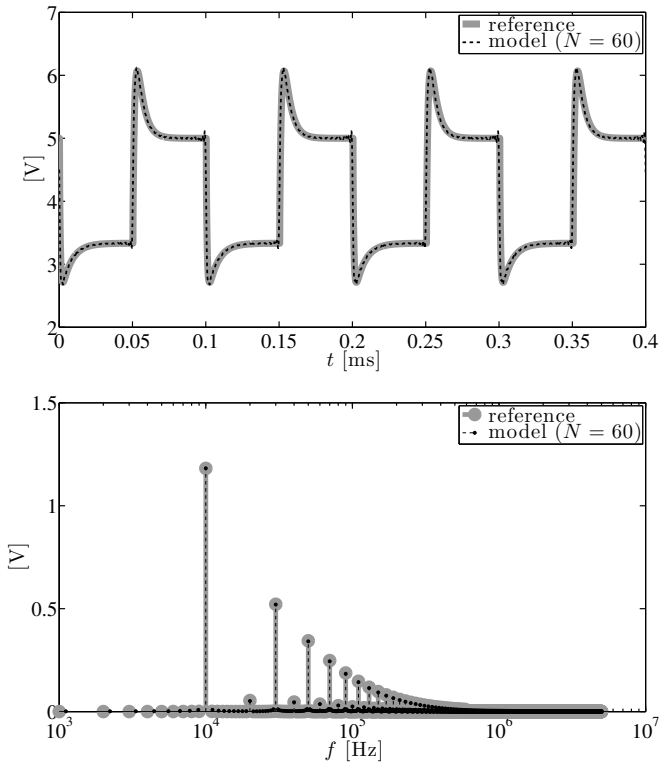

Figure 3.5: Time-domain response of the voltage $v_{AB}(t)$ of the circuit in Fig. 3.4 (top panel) and its corresponding frequency-domain spectrum $V_{AB}(f)$ (bottom panel) for a DC excitation $e(t) = 10V$. Solid gray lines: results from the proposed mathematical model; solid black lines: results from reference time-domain simulation.

$(2N + 1)$ considered in the Fourier series (3.21) (in the proposed results $(2N + 1) = 121$). From the Fourier theory, the number of harmonics to take into account in the Fourier expansion of the voltage $V_{AB}(\omega)$ depends on the regularity of the behavior of the voltage in time-domain [49]. Instead the computation cost of the reference time-domain piece-wise simulation is 3 s but it depends on the considered time-step and on the duration of the transient of the variables of the circuit.

3.4 Chapter Summary

This Chapter shows how the mathematical framework introduced in Chap. 2 can be suitably used to analyze generic circuits containing periodic switches via two examples. The proposed method is an extension of well-known *harmonic balance* method [21, 22] for the particular case of PSL circuits that belongs to the class of PLTV systems, where the time-varying element is replaced by its augmented admittance or impedance representation. The proposed results shown a good agreement with the standard time-domain simulation technique both in time- and in frequency-domain, but it is not clear how the method can be generalized for the analysis of circuit with a

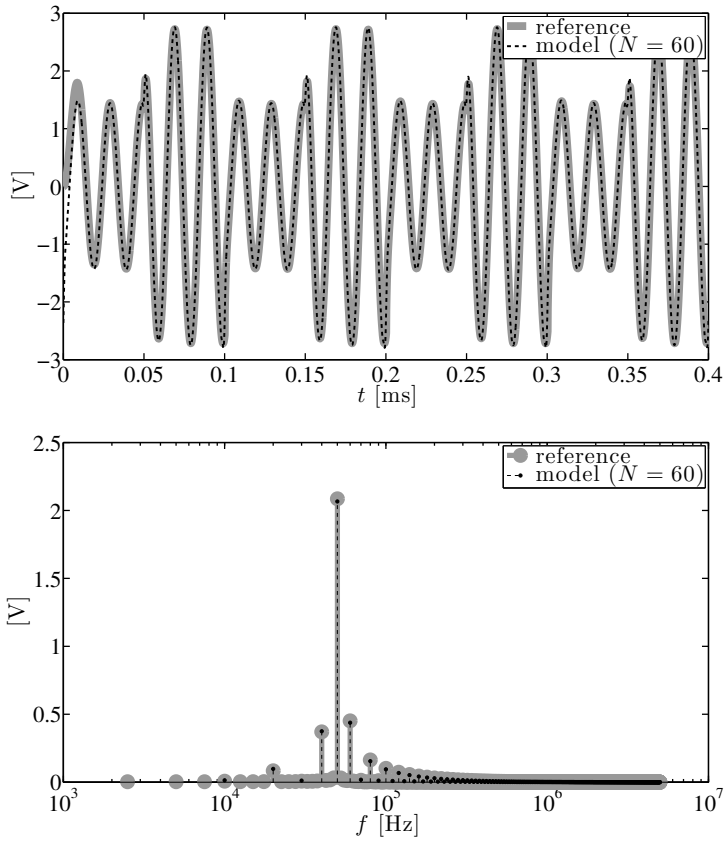

Figure 3.6: Time-domain response of the voltage $v_{AB}(t)$ of the circuit in Fig. 3.4(top panel) and its corresponding frequency-domain spectrum $V_{AB}(f)$ (bottom panel) for a sinusoidal excitation $v_s(t) = 10\sin(2\pi f_0 t)$, where $f_0 = 50\,\text{kHz}$. Solid gray lines: results from mathematical model; solid black lines: results from simulations.

large number of components. The next chapter will deal with an automatic tool for the circuit simulation based on a new interpretation of the classical approaches for the circuit analysis.

Chapter 4

Solution via Augmented Nodal Analysis

The results collected in the previous Chapter clearly highlight that the steady-state response of a PSL circuit can be readily obtained directly in frequency-domain via the solution of a system of linear equations. As an example, for the illustrative circuit of Fig. 3.4 writes:

$$\mathbf{TV} = \mathbf{E} \tag{4.1}$$

where the matrix $\mathbf{T}$ is related to the structure of the network, $\mathbf{V}$ is a vector collecting the Fourier coefficients of the unknown voltage variable of the circuit and $\mathbf{E}$ is a vector containing the excitation terms. It is important to notice that the above equation has been derived using a custom approach via the direct application of the Kirchhoff's equations, thus leading to a procedure that is dependent on the specific example at hand.

In order generalize the method, this Chapter suggests to interpret the PSL circuits as the combination of LTI elements and ideal switches. According to the theory of PLTV systems, all the circuit elements are then replaced by suitable LTI augmented equivalents that are computed once. The above equivalents generate an augmented circuit that can be solved directly in frequency-domain by means of standard tools for circuit analysis as the modified nodal analysis (MNA). Clearly, this procedure provides a general and modular approach to PSL circuit analysis based on robust methods available for the solution of time-invariant circuits.

The Chapter is organized as follows. In the first section, the classical MNA tool for LTI circuits is shortly presented. Section 4.2 focuses on its extension to the steady-state analysis of PSL circuits. In Sections 4.4 and 4.5 the proposed method is applied to predict the steady-state responses of two example circuits with additional details on its accuracy, efficiency and convergence.

4.1 MNA Tool

The MNA equation [24, 23] can in general be expressed in the form:

$$\left[\begin{array}{c|c} \mathbf{Y_R}(\omega) & \mathbf{B} \\ \hline \mathbf{C} & \mathbf{D}(\omega) \end{array}\right] \left[\begin{array}{c} \mathbf{V}(\omega) \\ \hline \mathbf{I}(\omega) \end{array}\right] = \left[\begin{array}{c} \mathbf{J}(\omega) \\ \hline \mathbf{F}(\omega) \end{array}\right] \tag{4.2}$$

where $\mathbf{Y_R}$ is a reduced form of the nodal matrix excluding the contributions due to the voltage sources, current controlled elements, etc., $\mathbf{B}$ contains that partial derivatives of the KCL current equations with respect to the additional current variables of the current controlled elements and thus contains only ± 1. The branch constitutive relations for the current controlled components are represented by matrices $\mathbf{C}$ and $\mathbf{D}$. It is noticed that $\mathbf{C} = \mathbf{B}^T$ except for some nonreciprocal elements. The vectors $\mathbf{J}$ and $\mathbf{F}$ are the excitations which include current and voltage sources respectively. It is advantageous to consider the contributions of each circuit element to the MNA matrix separately as shown in the Table 4.1.

ELEMENT	SYMBOL	MATRIX	SOURCE	EQUATION
Current Source	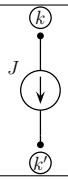		$\begin{matrix} k \\ k' \end{matrix}\begin{bmatrix} J \\ -J \end{bmatrix}$	$I_k = J$ $I_{k'} = -J$
Voltage Source	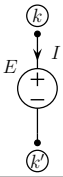	$\begin{matrix} & V_k & V_{k'} & I \\ k & & & 1 \\ k' & & & -1 \\ l+m & 1 & -1 & 0 \end{matrix}$	$\begin{matrix} k \\ k' \\ l+m \end{matrix}\begin{bmatrix} \\ \\ E \end{bmatrix}$	$V_k - V_{k'} = E$ $I_k = I$ $I_{k'} = -I$
Conductance		$\begin{matrix} & V_k & V_{k'} \\ k & g & -g \\ k' & -g & g \end{matrix}$		$I_k = g\,(V_k - V_{k'})$ $I_{k'} = -g\,(V_k - V_{k'})$
Admittance (voltage controlled element)	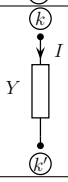	$\begin{matrix} & V_k & V_{k'} \\ k & Y & -Y \\ k' & -Y & Y \end{matrix}$		$I_k = Y\,(V_k - V_{k'})$ $I_{k'} = -Y\,(V_k - V_{k'})$
Impedance (current controlled element)	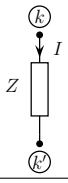	$\begin{matrix} & V_k & V_{k'} & I \\ k & & & 1 \\ k' & & & -1 \\ l+m & 1 & -1 & -Z \end{matrix}$		$V_k - V_{k'} - ZI = 0$ $I_k = -I_{k'} = 0$

Table 4.1: Table collecting the MNA stamps for the main LTI elements.

For the sake of illustration let us consider the example circuit of Fig. 4.1, where a non-ideal voltage source with inductive series impedance is connected to a generic voltage controlled component (i.e. a capacitor) described by its admittance $Y(\omega)$.

According to the Table 4.1 the MNA equation in matrix form of the circuit writes:

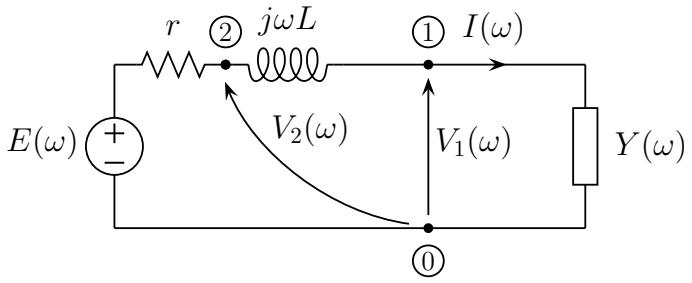

Figure 4.1: Example test circuit used for illustrating the proposed MNA formulation for the case of an LTI circuit.

$$\left[\begin{array}{c:c|c} Y(\omega) & 0 & -1 \\ \hdashline 0 & g & 1 \\ \hline -1 & 1 & -j\omega L \end{array}\right] \left[\begin{array}{c} V_1(\omega) \\ \hdashline V_2(\omega) \\ \hdashline I(\omega) \end{array}\right] = \left[\begin{array}{c} 0 \\ \hdashline gE(\omega) \\ \hdashline 0 \end{array}\right] \tag{4.3}$$

where $g = 1/r$ and the series interconnection between the voltage source $E(\omega)$ and the resistor r is replaced by its Norton equivalent. The unknown node voltages $V_1(\omega)$ and $V_2(\omega)$ and the current $I(\omega)$ can be computed by inverting the MNA matrix for each value of the frequency variable ω.

It is import to remark, that for the case of LTI circuits the MNA equation (e.g., (4.3)) does not show any coupling among the different harmonics of the variables of the circuit, this means that current and voltage variables contain the same frequency components of the excitation of the circuit.

4.2 Augmented Time-Invariant Interpretation of Switching Circuits

The classical MNA tool derived in the previous Section can be extended to the case of PSL circuits. For notational convenience, a generic two-terminal LTI or switch element with the associated voltage $v(t)$ and current $i(t)$ variables defined with passive sign convention is assumed. All the electrical variables of the circuit are represented in the augmented framework by means of a truncated series of delta function as introduced in Chap. 3.

As an example a generic voltage variable $V(\omega)$ of a PSL circuit to a cisoidal excitation is replaced in the augmented version of circuit by the series:

$$V(\omega) \approx \sum_{n=-N}^{+N} V_n \delta(\omega - n\omega_c - \omega_0) \tag{4.4}$$

where $\omega_c = 2\pi T$ and T represents the period of the PSL system and ω_0 represents the frequency of the excitation of the system.

The following results illustrate the contributions of each circuit element to the MNA equation separately.

4.2.1 Characteristic of LTI elements

For the case of a simple resistor with characteristic $v = Ri$, the relation between its current and voltage harmonics turns out to be frequency independent and writes:

$$I_n = V_n/R = GV_n, \quad n = -N, \ldots, 0, \ldots, N \tag{4.5}$$

that can be rewritten in matrix form as:

$$\begin{bmatrix} I_{-N} \\ \vdots \\ \vdots \\ I_N \end{bmatrix} = \begin{bmatrix} G & 0 & \ldots & 0 \\ 0 & G & \ddots & \vdots \\ \vdots & \ddots & \ddots & 0 \\ 0 & \ldots & 0 & G \end{bmatrix} \begin{bmatrix} V_{-N} \\ \vdots \\ \vdots \\ V_N \end{bmatrix}, \tag{4.6}$$

or in a more compact form:

$$\mathbf{I} = \mathbf{G}\mathbf{V} \tag{4.7}$$

where $\mathbf{G} = \mathrm{diag}([G, \ldots, G])$ and the voltage and current variables $V(\omega)$ and $I(\omega)$ are replaced by the vectors $\mathbf{V} = [V_{-N}, \ldots, V_0, \ldots, V_N]^T$ and $\mathbf{I} = [I_{-N}, \ldots, I_0, \ldots, I_N]^T$. The above vectors, that have dimension $(2N + 1)\times 1$, are filled in by the harmonic coefficients defining the steady-steady response of the corresponding variables and play the role of the new port variables of an augmented circuit element as shown in (4.4).

For the case of a dynamic element, such as the capacitor with $i = Cdv/dt$, the corresponding constitutive relation becomes:

$$I_n = j(\omega_0 + n\omega_c)CV_n, \quad n = -N, \ldots, 0, \ldots, N, \tag{4.8}$$

That can be recast as:

$$\begin{bmatrix} I_{-N} \\ \vdots \\ \vdots \\ I_N \end{bmatrix} = \begin{bmatrix} j(\omega_0 + N\omega_c)C & 0 & \ldots & 0 \\ 0 & \ddots & \ddots & \vdots \\ \vdots & \ddots & \ddots & 0 \\ 0 & \ldots & 0 & j(\omega_0 - N\omega_c)C \end{bmatrix} \begin{bmatrix} V_{-N} \\ \vdots \\ \vdots \\ V_N \end{bmatrix}, \tag{4.9}$$

or in a more compact form:

$$\mathbf{I} = j\boldsymbol{\omega}C \cdot \mathbf{V} \tag{4.10}$$

where $\boldsymbol{\omega} = \mathrm{diag}([\omega_0 - N\omega_c, \ldots, \omega_0 + N\omega_c])$.

Following the same reasoning, a similar equation can be derived for the alternate case of the linear inductor:

$$\mathbf{V} = j\boldsymbol{\omega}L \cdot \mathbf{I} \tag{4.11}$$

It is important to remark that the augmented representations of the classical LTI elements involve diagonal matrices only. In fact due to the time-invariant properties, the port variables of the LTI elements do not present any coupling between their harmonic components.

4.2.2 Characteristic of switches

Different from the case of the LTI elements, the augmented version of a switch element requires additional effort. Similar to the case of the PSL block analyzed in Sec. 3.1, the generic periodical switch element S_k of Fig. 4.2 needs to be characterized by its bi-frequency admittance or impedance representation.

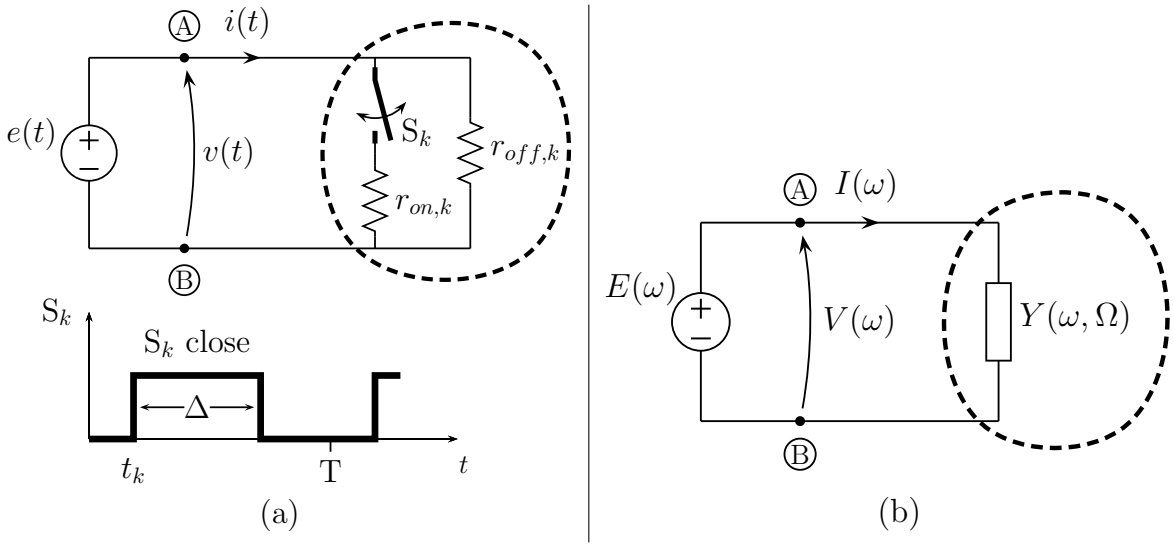

Figure 4.2: Panel(a): time-domain model for a generic switch element; Panel(b): frequency-domain representation in terms of its bi-frequency admittance $Y(\omega, \Omega)$.

According to Fig. 4.2(a), the switch element S_k is defined by the following parameters:

1. the close and open resistances $r_{on,k}$ and $r_{off,k}$ which are the resistance values at the input port of the element when the switch is in the open and close state (to simplify the following equations we assume $r_{on,k} \ll r_{off,k}$);
2. the switching period T and its corresponding switching frequency f_c;
3. the closure time instant of the switch in the fist period t_k;
4. the duration of the closed state Δ_k.

The considered element S_k is the generalization of the simple resistive PSL example seen in Chap. 3, and its v-i time-domain characteristic is given by the following time-dependent resistance $r_k(t)$:

$$r_k(t) = r_{on,k} \sum_{n=-\infty}^{+\infty} \Pi_{\Delta_k}(t - t_k - nT) + r_{off,k} \left(1 - \sum_{n=-\infty}^{+\infty} \Pi_{\Delta_k}(t - t_k - nT)\right) \tag{4.12}$$

where $\Pi_\Delta(t - t_0)$ is the window function defined in Chap. 3:

$$\Pi_{\Delta}(t-t_0) = \begin{cases} 1 & t_0 \leq t \leq \Delta + t_0 \\ 0 & \text{otherwise} \end{cases} \tag{4.13}$$

From to the theory of the PSL systems (see Chap. 2) the bi-frequency admittance $Y(\omega, \Omega)$ for a generic switch element is defined as:

$$Y_k(\omega, \Omega) \;=\; 2\pi \sum_{n=-\infty}^{+\infty} Y_{n,k} \cdot \delta\left(\omega - \Omega - n\omega_c\right). \tag{4.14}$$

where the aliasing admittances $Y_{n,k}$ for the considered switch element S_k, are defined by the following equation:

$$Y_k \;=\; f_c c_{n,k} \left(g_{on,k} + g_{off,k} \exp\left(jn\omega_c t_k\right)\right) \tag{4.15}$$

where in this case $g_{on,k} = 1/r_{on,k}$, $g_{off,k} = 1/r_{off,k}$ and $\omega_c = 2\pi f_c$.

According to the definition of the window function $w_k(t) = \Pi_{\Delta_k}(t - t_k)$ (4.13), the Fourier coefficients $c_{n,k}$ are computed by the following integral:

$$\begin{aligned} c_{n,k} &= \int_{-\infty}^{+\infty} w(t) \exp(-jn\omega_c t) dt \\ &= \int_{t_k}^{t_k+\Delta_k} \exp(-jn\omega_c t) dt \\ &= \frac{\exp(-jn\omega_c t_k) - \exp(-jn\omega_c(t_k+\Delta_k))}{jn\omega_c}. \end{aligned} \tag{4.16}$$

The generalized Ohm's law introduced in the previous Chapters for a truncated expansion of order N of the voltage and current variables allows to write:

$$\begin{aligned} I(\omega) &= \sum_{n=-N}^{+N} I_n \delta(\omega - n\omega_c - \omega_0) \\ &= \sum_{l=-N}^{N} \sum_{m=-N}^{N} Y_{m,k} V_l \delta(\omega - (l+k)\omega_c - \omega_0) \end{aligned} \tag{4.17}$$

for $|m + l| \leq N$.

Similar to the example of Chap. 3, the current and the voltage variables through and across the PSL element are replaced by $(2N + 1)$ Fourier coefficients V_n and I_n respectively. The last equation can be rewritten in terms of its matrix formulation:

$$\begin{bmatrix} I_{-N} \\ \vdots \\ I_0 \\ \vdots \\ I_N \end{bmatrix} = \begin{bmatrix} Y_{0,k} & Y_{-1,k} & \dots & \dots & Y_{-2N,k} \\ Y_{1,k} & Y_{0,k} & \dots & \dots & \vdots \\ \vdots & \vdots & \ddots & \vdots & \vdots \\ \vdots & \vdots & \vdots & \ddots & Y_{-1,k} \\ Y_{2N,k} & \dots & \dots & Y_{1,k} & Y_{0,k} \end{bmatrix} \begin{bmatrix} V_{-N} \\ \vdots \\ V_0 \\ \vdots \\ V_N \end{bmatrix} \tag{4.18}$$

where the voltage and current variables $V(\omega)$ and $I(\omega)$ are replaced by the vectors $\mathbf{V} = [V_{-N}, \dots, V_0, \dots, V_N]^T$ and $\mathbf{I} = [I_{-N}, \dots, I_0, \dots, I_N]^T$ as in the augmented representation of the LTI elements. Equation (5.6), that turns out to be a linear time-invariant representation of the PSL element, which can be written in a more compact form as

$$\mathbf{I} = \mathbf{Y}_k \mathbf{V} \tag{4.19}$$

where $\mathbf{Y}_k$ is the $(2N+1) \times (2N+1)$ matrix of (5.6).

Different from the classical LTI elements the MNA stamp for the LTI element in Sec. 4.2.1, the augmented admittance matrix for the switch element is a non-diagonal matrix. In fact due to the presence of the integral operator (3.9) the PSL switch element couples the voltage and current harmonics, thus the frequency response of PSL circuits to a single bar excitation contains an infinite number of harmonics.

4.3 Analysis via Augmented MNA

The analysis by means of the augmented MNA equation can be summarized as follows:

- compute the augmented admittance representations of both the classical LTI and the switching elements [20, 19]. For the LTI case, as outlined in Sec. 4.2.1, the augmented representations are trivial and turns out to be vectors with one nonzero entry for the voltage or current sources or diagonal matrices for circuit elements such as resistors, capacitors and inductors. Instead the augmented representation for the switched elements leads to a full coupled matrix as described in Sec. 4.2.2;

- re-interpret the original time-varying circuit as an equivalent augmented circuit consisting of the interconnection of the above alternative representations of circuit elements. In this circuit the new nodal voltages correspond to the expansion coefficients of the original nodal voltages (e.g., the entries of vector $\mathbf{V}$ in (4.4));

- apply standard simulation tools as the MNA to compute the expansion coefficients of the variable of interests.

In the next sections the proposed approach is applied to compute the response of two PSL circuits.

4.4 Example 1

The example is based on the PSL circuit of Fig. 4.3(a) and on its frequency-domain representation of Fig. 4.3(b) where the switch is replaced by its bi-frequency admittance representation Y_1. During the following MNA formulation the ideal voltage source $e(t)$ is defined by a cisoidal excitation $e(t) = (E_0/2\pi)\exp(j\omega_0 t)$ with angular frequency ω_0. All the variables of the circuit are replaced by their Fourier expansion according to (4.4).

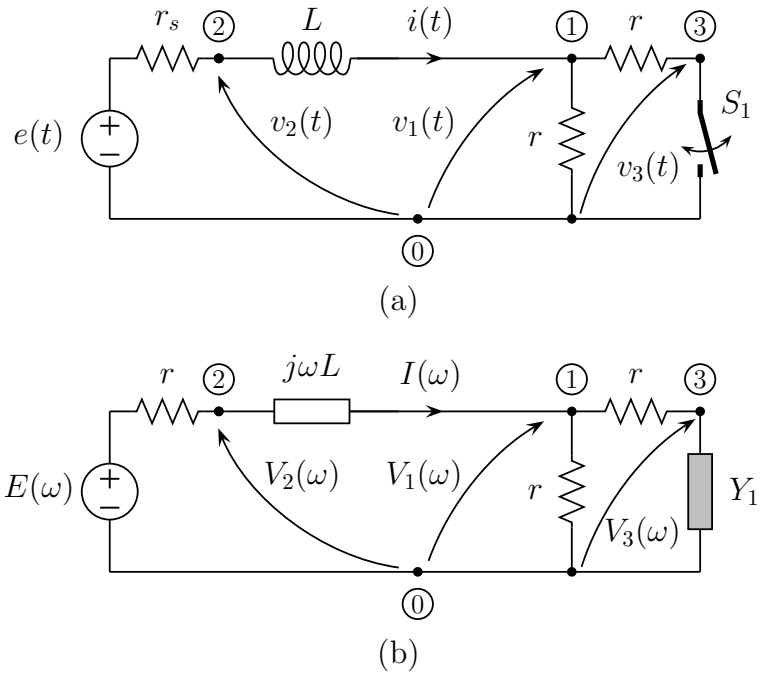

Figure 4.3: Test PSL circuit for the example 1 used for illustrating the proposed augmented MNA formulation both in time-domain (panel(a)) and in frequency-domain (panel(b)).

The augmented characteristic of the two-terminal switch element defined by (5.6) and (4.19) and the companion relations that can be readily obtained for the classical LTI elements allow to write the MNA equation as:

$$\left[\begin{array}{c:c:c|c} 2g\mathbf{1} & \mathbf{0} & -g\mathbf{1} & -\mathbf{1} \\ \hdashline \mathbf{0} & g_s\mathbf{1} & \mathbf{0} & \mathbf{1} \\ \hdashline -g\mathbf{1} & \mathbf{0} & g\mathbf{1}+\mathbf{Y_1} & \mathbf{0} \\ \hline -\mathbf{1} & \mathbf{1} & \mathbf{0} & -j\boldsymbol{\omega}L \end{array}\right] \left[\begin{array}{c} \boldsymbol{V}_1 \\ \hdashline \boldsymbol{V}_2 \\ \hdashline \boldsymbol{V}_3 \\ \hdashline \boldsymbol{I} \end{array}\right] = \left[\begin{array}{c} \mathbf{0} \\ \hdashline g\boldsymbol{E} \\ \hdashline \mathbf{0} \\ \hdashline \mathbf{0} \end{array}\right] \tag{4.20}$$

where all the the entries of the matrix are submatrices with dimension $(2N+1)\times(2N+1)$, where $\mathbf{1}$=diag(1), $\mathbf{0}$=diag(0) and $\boldsymbol{\omega}$=diag($[\ldots,(\omega_0-\omega_c),\omega_0,(\omega_0+\omega_c),\ldots]$), according to

Sec. 4.2.2. On the right hand side of the MNA equation, the excitation term is composed by vectors of dimension $(2N+1)\times 1$ defined as $\mathbf{0}=[0,\ldots,0]^T$ and $\boldsymbol{E}=[0,\ldots,E_0,\ldots,0]^T$.

Clearly, equation (4.20) turns out to be $(2N+1)$ times larger than the corresponding MNA equation of a circuit with the PSL element replaced by a LTI element. However, the proposed extended MNA equation, that belongs to the same class of (4.3), can be readily solved via simple linear inversion. What is more important, the steady-state response of the PSL circuit can be computed by re-interpreting the coefficients of the new voltage and current unknowns by means of (3.21). As an example, the unwrapped and complete extended MNA stamp for the example circuit of Fig. 4.3 with $N=1$ becomes the matrix equation (4.21).

Summarizing, the proposed simulation method is valid for PSL circuits with both constant sources (a constant is seen as a cisoidal signal with null angular frequency) and any arbitrary periodic excitation, provided that the latter signal is expended in Fourier series. Also, the solution of the augmented MNA equation like (4.21) provides the direct computation of the steady-state response of the circuit.

Numerical Results

In order to validate the frequency-domain augmented description presented in this Chapter, the current i and the voltage v_1 of the example PSL circuit of Fig. 4.3 are computed via the MNA equation (4.20) for an increasing number of the expansion order N. For plot readability, a maximum order of $N=50$ has been considered since a larger order generates responses overlapping the reference curve very well and does not allow to appreciate the differences among the approximated responses.

The values of the components used in the simulation are the following: $r_s = 10\,\Omega$, $L = 1\,\text{mH}$, $r = 100\,\Omega$ and the switch S has a periodic switching activity at frequency $f_c = 10\,\text{kHz}$. The independent DC voltage source $e(t) = 10\,\text{V}$ is defined in frequency-domain as: $E(\omega) = 10/2\pi\delta(\omega)\,\text{V}$.

Fig. 4.4 shows a comparison for the current i and voltage v_1 between the presented approach and a time-domain MATLAB simulation (reference curves) based on the standard ordinary differential equation (ODE) integration routines assumed as reference.

In order to provide a better and quantitative comparison, Table 4.2 collects the main figures on the accuracy and efficiency of the ODE-based and of the proposed frequency-domain MNA-based method implemented in MATLAB environment.The accuracy is assessed by computing the relative mean square error between the reference and the predicted responses. Also, the overhead of the proposed method in computing the aliasing admittances Y_n is included in the total CPU-time. The numbers in the Table confirm the strengths of the proposed approach, that has a number of advantages over alternative state-of-the art methods. Mainly, it allows to compute the solution of the nodal variables of a periodically switched circuit in both frequency- and time-domain by means of the solution of a single linear problem. The coefficients of the unknown vector of (4.21) are the numbers multiplying either the complex trigonometric functions defining the time-domain responses or the deltas defining the different terms composing the corresponding frequency-domain spectra.

Table 4.2: CPU time required by the simulation of the circuit of Fig. 4.3 and accuracy of the computed current and voltage responses $i(t)$ and $v_1(t)$, for an increasing number of terms N defining their truncated expansions (e.g., see (3.21)).

	ODE	Extended MNA						
Method	t_{step}=1 ns $t_{\max}$=500 μs	N=1	N=5	N=15	N=50	N=75	N=100	N=150
CPU Time	18.7 s	0.052 s	0.059 s	0.079 s	0.15 s	0.17 s	0.23 s	0.46 s
Relative error $i(t)$	reference	4.7%	1.3%	0.4%	0.13%	0.09%	0.06%	0.04%
Relative error $v_1(t)$	reference	15%	9.5%	5.9%	3.4%	2.7%	2.42%	1.98%

4.5 Example 2

As a second example, the proposed augmented MNA approach is applied to the schematic of Fig. 4.5. The topology of this second example is similar to the ones occurring in a number of application (e.g., the dc-dc boost converter is defined by a similar circuit involving two switch elements i.e., the diode and the MOS transistor as shown in Chap. 6).

Similar to the previous example, the augmented interpretation of the LTI and PSL elements of the schematic in Fig. 4.5(b) allows to write the augmented MNA equation of the considered circuit directly in frequency-domain, as follows:

$$\left[\begin{array}{c|c|c|c|c} g\mathbf{1} & \mathbf{0} & \mathbf{0} & \mathbf{0} & -\mathbf{1} \\ \hline \mathbf{0} & g\mathbf{1}+\mathbf{Y_1} & -\mathbf{Y_1} & \mathbf{0} & -\mathbf{1} \\ \hline \mathbf{0} & -\mathbf{Y_1} & G\mathbf{1}+\mathbf{Y_1} & -G\mathbf{1} & \mathbf{0} \\ \hline \mathbf{0} & \mathbf{0} & -G\mathbf{1} & (G+G_L)\mathbf{1}+j\boldsymbol{\omega}C & \mathbf{0} \\ \hline \mathbf{1} & -\mathbf{1} & \mathbf{0} & \mathbf{0} & -j\boldsymbol{\omega}L \end{array}\right] \left[\begin{array}{c} \boldsymbol{V}_1 \\ \hline \boldsymbol{V}_2 \\ \hline \boldsymbol{V}_3 \\ \hline \boldsymbol{V}_4 \\ \hline \boldsymbol{I}_2 \end{array}\right] = \left[\begin{array}{c} g\boldsymbol{E} \\ \hline \mathbf{0} \\ \hline \mathbf{0} \\ \hline \mathbf{0} \\ \hline \mathbf{0} \end{array}\right] \tag{4.22}$$

where, all the entries of the matrix are $(2N+1)\times(2N+1)$ submatrices and the scalar conductances are defined as: $g = 1/r$, $G = 1/R$ and $G_L = 1/R_L$.

Numerical Results

Also for this second example, the augmented MNA equation (4.22) is used to compute the steady-state responses of the voltage v_4 and of the current i_2 for the schematic in Fig. 4.5.

The values of the components used in the simulation are the following: $r_s = 10\,\Omega$, $L = 1\,\text{mH}$, $r = 100\,\Omega$, $r_L = 100\,\Omega$ and $C = 1\,\mu\text{F}$. The switch operates as in the first example of Fig. 4.3. The independent voltage source $e(t) = 10 + 2\sin(\omega_0 t)\,\text{V}$ is defined in frequency-domain as $E(\omega) = 10/(2\pi)\delta(\omega) + 1/j\pi(\delta(\omega - \omega_0) - \delta(\omega + \omega_0))\,\text{V}$, where $\omega_0 = 2\pi f_0$ and $f_0 = 40\,\text{kHz}$.

Figure 4.6 shows the reference and the predicted responses of the voltage $v_4(t)$ and the current $i_2(t)$ of this second test circuit. The curves in the Figure highlight that the proposed method produces the steady-state responses of a PSL circuit and that does not include the initial transient observed in the reference response of the circuit calculated via an ODE-based solver with null initial conditions of the dynamical components. As far as the performance of the proposed method is concerned, the trend given by the numbers of Tab. 4.2 is also confirmed for this second example in Tab. 4.3.

Table 4.3: CPU time required by the simulation of the circuit of Fig. 4.5 and accuracy of the computed current and voltage responses $i_2(t)$ and $v_4(t)$, for an increasing number of terms N defining their truncated expansions (e.g., see (3.21)).

	ODE	Extended MNA						
Method	t_{step}=1 ns $t_{\max}$=500 μs	N=1	N=5	N=15	N=50	N=75	N=100	N=150
CPU Time	34.5 s	0.029 s	0.051 s	0.076 s	0.19 s	0.24 s	0.445 s	1.1 s
Relative error $i_2(t)$	reference	3.3%	0.9%	0.3%	0.08%	0.05%	0.04%	0.02%
Relative error $v_4(t)$	reference	4.9%	1.7%	0.6%	0.2%	0.14%	0.1%	0.07%

4.6 Chapter Summary

This Chapter addressed the analysis and the simulation of the steady-state behavior of an important class of time-varying circuits consisting of LTI (possibly dynamical) circuit elements, periodically switched linear resistive elements and ideal sources defined by periodic excitations. The proposed solution is based on the generation of an augmented time-invariant MNA equation governing the circuit behavior. The new nodal unknowns in the advocated formulation correspond to the harmonic coefficients defining the expansions of the unknown voltage and current variables. A topological approach is considered, with emphasis on an intuitive physical based interpretation of the switching element in the network. The proposed solution is proven to offer a modular approach to circuit analysis, leading to accurate results with good simulation speed-ups. Also, it is sufficiently general to handle a wide class of circuit topologies occurring in real application problems. The feasibility and strengths of the method are demonstrated on simple analytical examples and two validation test circuits.

$$
\left[\begin{array}{cccccccccc|cccc}
2g & 0 & 0 & 0 & 0 & 0 & -g & 0 & 0 & 0 & -1 & 0 & 0 \\
0 & 2g & 0 & 0 & 0 & 0 & 0 & -g & 0 & 0 & 0 & -1 & 0 \\
0 & 0 & 2g & 0 & 0 & 0 & 0 & 0 & -g & 0 & 0 & 0 & -1 \\
0 & 0 & 0 & 2g & 0 & 0 & 0 & 0 & 0 & -g & 0 & 0 & 0 \\
\hline
0 & 0 & 0 & 0 & g_s & 0 & 0 & 0 & 0 & 0 & 1 & 0 & 0 \\
0 & 0 & 0 & 0 & 0 & g_s & 0 & 0 & 0 & 0 & 0 & 1 & 0 \\
0 & 0 & 0 & 0 & 0 & 0 & g_s & 0 & 0 & 0 & 0 & 0 & 1 \\
\hline
-g & 0 & 0 & 0 & 0 & 0 & Y_0+g & Y_{-1} & Y_{-2} & 0 & 0 & 0 & 0 \\
0 & -g & 0 & 0 & 0 & 0 & Y_1 & Y_0+g & Y_{-1} & 0 & 0 & 0 & 0 \\
0 & 0 & -g & 0 & 0 & 0 & Y_2 & Y_1 & Y_0+g & 0 & 0 & 0 & 0 \\
\hline
-1 & 0 & 0 & 1 & 0 & 0 & 0 & 0 & 0 & -j(\omega_0-\omega_c)L & 0 & 0 & 0 \\
0 & -1 & 0 & 0 & 1 & 0 & 0 & 0 & 0 & 0 & -j(\omega_0)L & 0 & 0 \\
0 & 0 & -1 & 0 & 0 & 1 & 0 & 0 & 0 & 0 & 0 & -j(\omega_0+\omega_c)L & 0
\end{array}\right]
\left[\begin{array}{c}
V_{1,-1} \\ V_{1,0} \\ V_{1,1} \\ V_{2,-1} \\ V_{2,0} \\ V_{2,1} \\ V_{3,-1} \\ V_{3,0} \\ V_{3,1} \\ I_{-1} \\ I_0 \\ I_1
\end{array}\right]
=
\left[\begin{array}{c}
0 \\ 0 \\ 0 \\ 0 \\ 0 \\ 0 \\ gE_0 \\ 0 \\ 0 \\ 0 \\ 0 \\ 0
\end{array}\right]
\tag{4.21}
$$

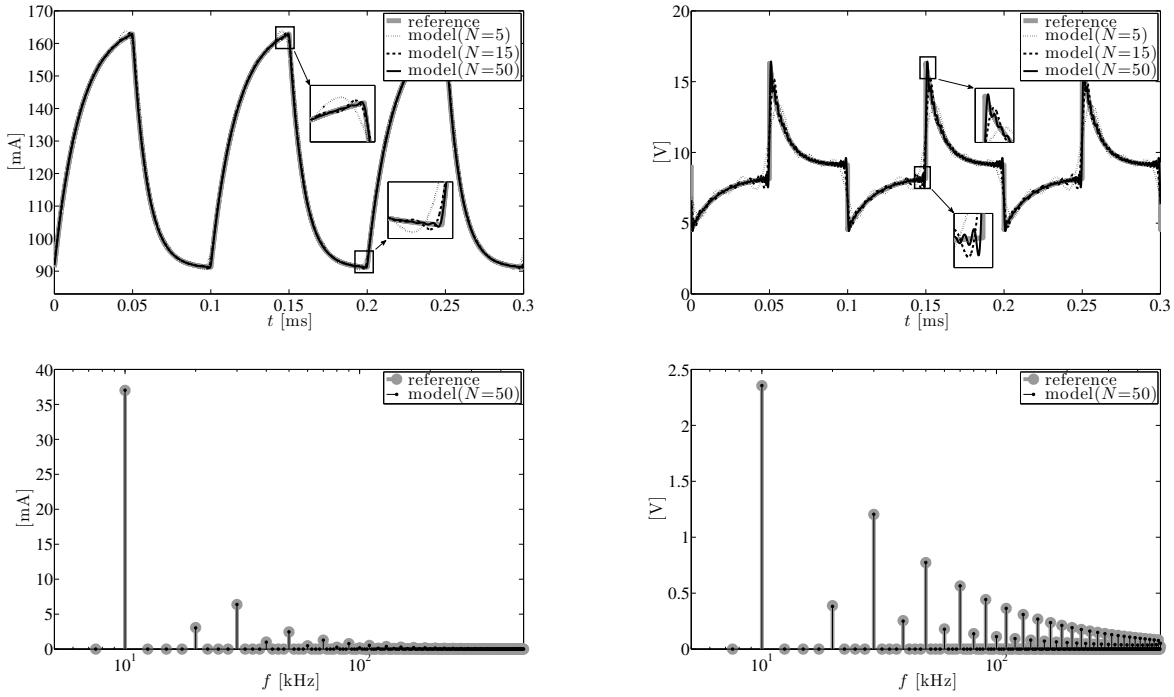

Figure 4.4: Time-domain (steady-state) responses of the current $i(t)$ for the circuit of Fig. 4.3 and its corresponding frequency-domain spectrum; The reference time-domain response (computed by means of the ODE-based routines in Matlab®) is compared with the solutions arising from (4.21) and different values of the order of expansion N.

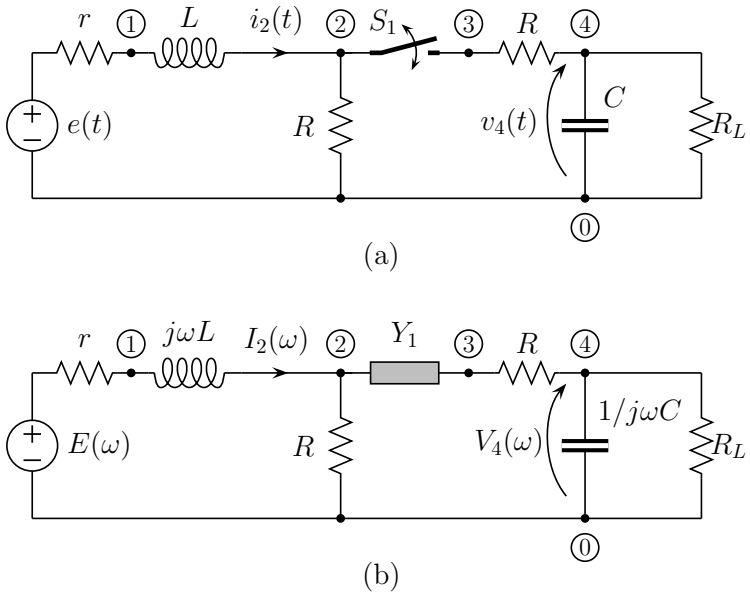

Figure 4.5: Test PSL circuit for the example 1 used for illustrating the proposed augmented MNA formulation both in time-domain (panel(a)) and in frequency-domain (panel(b)).

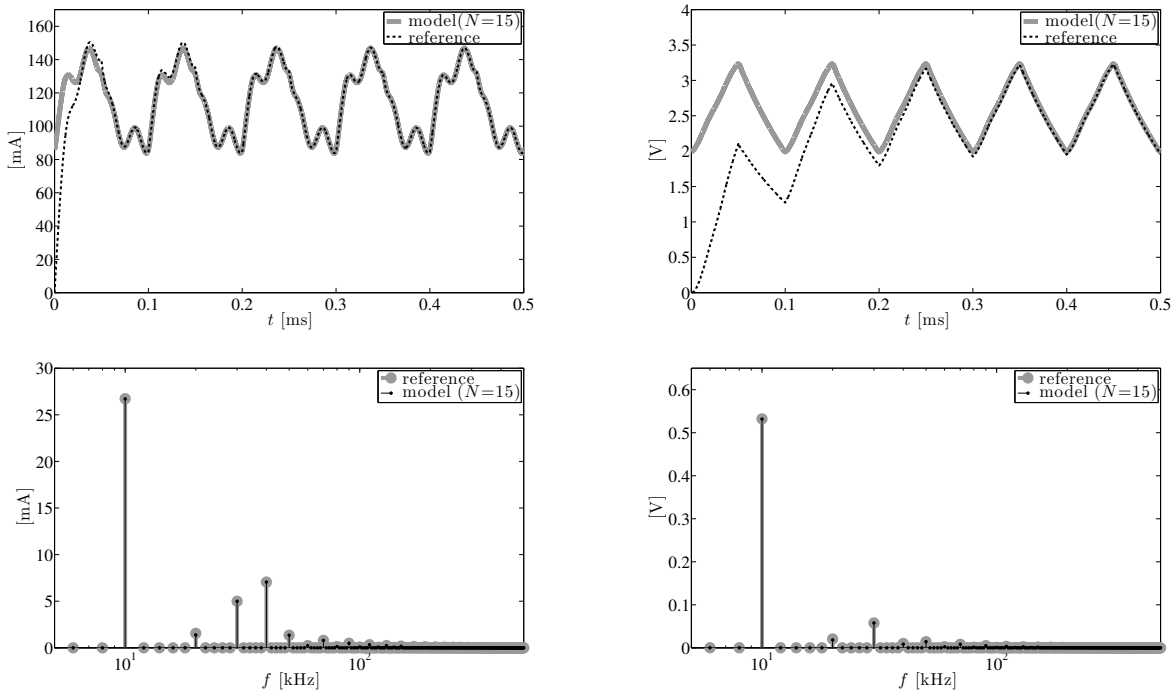

Figure 4.6: Top panel: current $i_2(t)$ and voltage $v_4(t)$ time-domain responses of the circuit of Fig. 4.5. Bottom panel: current $I_2(f)$ and voltage $V_4(f)$ frequency-domain spectra. The reference responses are computed with order expansion $N = 15$.

Chapter 5

Applications

For the sake of a better understanding, the proposed frequency-domain approach has been introduced by means of simple examples. This Chapter considers more realistic and meaningful applications, in which the innovative technique developed in this thesis is specialized on the analysis of four types of *switching converters* [43]–[45].

Switching converters are massively used to supply energy to electrical and electronic equipment and appliances. This class of circuits are inherently time-varying PSL systems that are characterized by the periodic behavior of their internal switches and demand for suitable methods for the prediction of the time-evolution of voltage and current signals.

Several simulation techniques are available that share a common and robust mathematical framework based on the time- and frequency-domain representation of the periodically switching response of this class of circuits [8, 10, 37, 31, 38, 39, 40, 41]. The main differences among these contributions reside in the computation of the kernels needed to represent the steady-state time-varying circuit behavior. In most of the literature, however, the mathematical development and the proposed technical solutions are cumbersome or demand for improvements, thus hindering the analysis of arbitrary network configurations. The aim of this Chapter is to provide a practical and efficient simulation procedure for the switching converters, based on the innovative approach introduced in this thesis.

5.1 Example 1: Boost Converter

In this Section the proposed frequency-domain analysis of switching circuit is applied on the *boost converter* of Fig. 5.1, operating in continuous conduction mode (CCM).

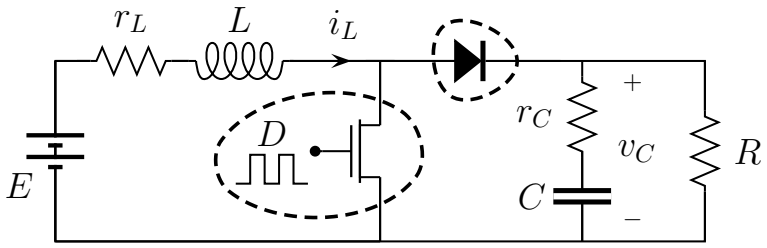

Figure 5.1: Dc-dc boost converter with its relevant electrical variables and components.

The boost converter is a dc-dc power converter where the output voltage v_c is greater than the input voltage E. The circuit is based on the switching activity of the nonlinear MOS and diode elements which are used as electronic switches. The MOS is controlled by a square wave of period T and duty cycle D, that is defined as the ratio between the time interval for which the MOS is tuned on (it is equivalent to a closed switch) and to the entire period. The switching frequency of the converter is defined via the period of the periodic square signal as $f_c = 1/T$.

The operating mode of the considered boost converter in CCM consists of two phases:

1. *the inductor charge phase*: the MOS is turned on and the inductor L is charged by the voltage source E causing the current i increasing to its maximal value;

2. *the inductor discharge phase*: the MOS is turned off, the inductor L is discharged into the RC parallel through the diode, causing the current i to decrease from the maximal value to its minimum one. Since L is discharged in series to the voltage generator E, the output voltage v_c will always be higher than E.

Summarizing, during the CCM the diode and the MOS can be represented by means of two switches characterized by a complementary periodic behavior, in fact, when the MOS is turned on the diode becomes an open circuit and vice versa.

At the steady-state the circuit presents a periodical behavior with switching frequency f_c defined via the frequency of the square waveform driving the MOS element which is periodically turned on and turned off. The frequency-domain representation of the converter of Fig. 5.2 is obtained from the schematic of Fig. 5.1 by replacing the nonlinear switching elements by the gray two-terminal switching elements labeled as Y_1 and Y_2 respectively, according to the theory of PSL elements (see Chap. 3).

The simulation of the circuit is based on its augmented MNA equation where the voltage and current unknowns are replaced by their Fourier expansions. Similar to the examples considered in the Chap. 4, the proposed simulation approach can be decomposed into the following two steps: (i) generate augmented LTI characteristics of all the circuit elements; (ii) obtain the steady-state solution of the original circuit in terms of the solution of an augmented LTI nodal equation.

The augmented MNA equation can be written in compact form as follows:

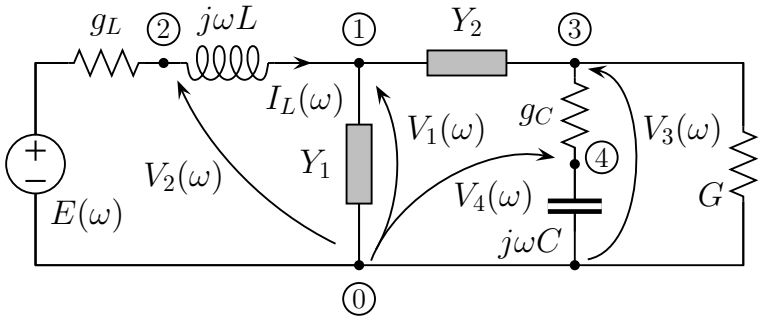

Figure 5.2: Frequency-domain representation of the boost converter of Fig. 5.1, where the PSL components are replaced with two augmented admittances Y_1 and Y_2.

$$\left[\begin{array}{c|c|c|c|c} \mathbf{Y_1+Y_2} & \mathbf{0} & \mathbf{-Y_2} & \mathbf{0} & \mathbf{-1} \\ \hline \mathbf{0} & g_L\mathbf{1} & \mathbf{0} & \mathbf{0} & \mathbf{1} \\ \hline \mathbf{-Y_2} & \mathbf{0} & \mathbf{Y_2}+(g_C+G)\mathbf{1} & -g_C\mathbf{1} & \mathbf{0} \\ \hline \mathbf{0} & \mathbf{0} & -g_C\mathbf{1} & g_C\mathbf{1}+j\boldsymbol{\omega}C & \mathbf{0} \\ \hline \mathbf{-1} & \mathbf{1} & \mathbf{0} & \mathbf{0} & -j\boldsymbol{\omega}L \end{array}\right] \left[\begin{array}{c} \boldsymbol{V}_1 \\ \hline \boldsymbol{V}_2 \\ \hline \boldsymbol{V}_3 \\ \hline \boldsymbol{V}_4 \\ \hline \boldsymbol{I}_L \end{array}\right] = \left[\begin{array}{c} \mathbf{0} \\ \hline g_L\boldsymbol{E} \\ \hline \mathbf{0} \\ \hline \mathbf{0} \\ \hline \mathbf{0} \end{array}\right] \tag{5.1}$$

In order to validate the proposed MNA characterization of the boost converter of Fig. 5.2, the input current I_L and the output voltage V_3 are computed both in frequency- and time-domain by inverting the matrix equation (5.1) and by using their Fourier series expansion (4.4). In the following results, the circuit elements of Fig. 5.1 take the following values: $E = 20\,\text{V}$, $r_L = 1\,\text{m}\Omega$, $L = 5\,\text{mH}$, $r_C = 5\,\text{m}\Omega$, $C = 10\,\mu\text{F}$, $R = 20\,\Omega$, $f_c = 10\,\text{kHz}$ and $D = 50\%$.

Fig. 5.3 and 5.4 collect the comparisons between the predicted and the reference time- and frequency-domain responses for the current $i_L(t)$ and $v_C(t)$ of Fig. 5.1. The reference results are computed via a MATLAB time-domain simulation based on classical ODE methods, while the corresponding spectra are obtained by applying the FFT algorithm to steady-state portion of the time-domain responses.

The curves highlight the good accuracy of the proposed solution in reproducing the steady-state responses of the boost converter without including the initial transient observed in the reference responses. It is important to remark that in the proposed comparison the two switches describing the MOS and the diode are assumed to have a non-ideal behavior, with an overlapping of 1% of the period T in which they are both closed. This is a parasitic condition occurring in a real power converter due to possible delays during the commutations of the non-linear elements.

The expansion order is set to a sufficiently large value $N = 110$ to allow for the inclusion of the high-frequency components of the proposed responses. As far as the accuracy and efficiency is concerned, a speed-up of $177\times$ ($0.13\,\text{s}$) and a mean square error-computed from the difference between the reference and the predicted responses of $< 0.25\%$ only is achieved.

The simulation results are obtained by a MacBook Pro (Intel Core i5 running @2.4GHz, 4GB RAM).

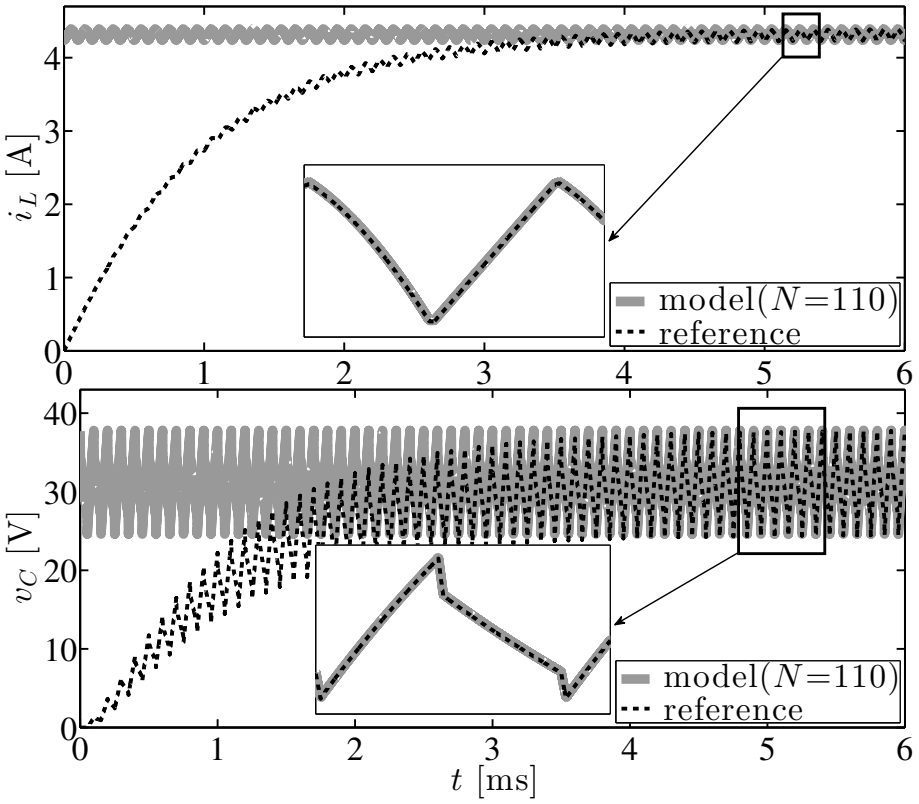

Figure 5.3: Time-domain responses of the current $i_L(t)$ and the voltage $v_C(t)$ of the circuit in Fig. 5.1. Dashed black: reference; solid gray: prediction with expansion order $N = 110$.

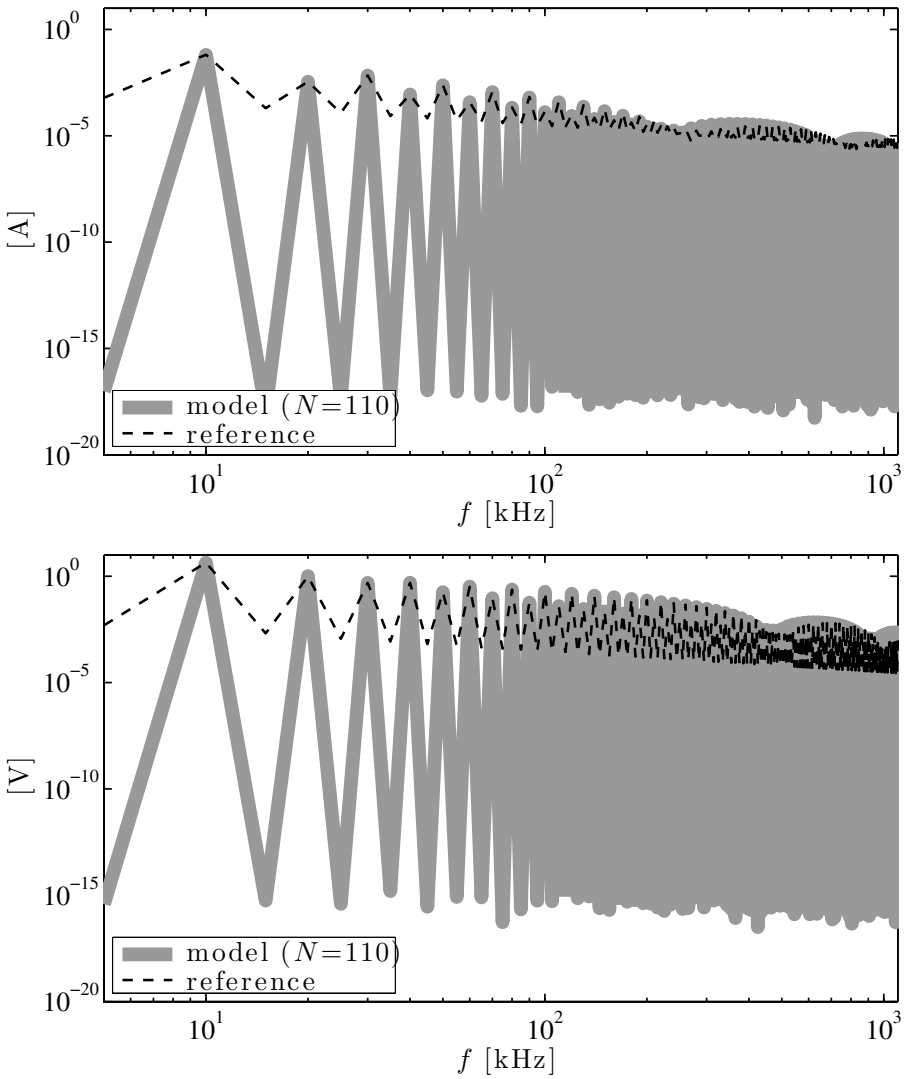

Figure 5.4: Frequency-domain responses of the current $i_L(t)$ and the voltage $v_C(t)$ of the circuit in Fig. 5.1. Dashed black: reference; solid gray: prediction with expansion order $N = 110$.

5.2 Example 2: Buck converter

In this Section the proposed frequency-domain approach is applied on the *buck converter* of Fig. 5.5 operating in CCM.

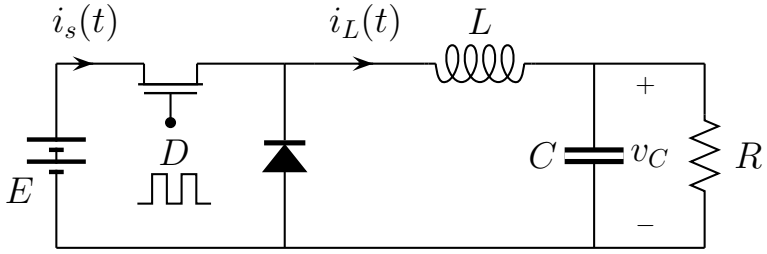

Figure 5.5: Schematic of a dc-dc buck converter with its relevant electrical variables and components.

The buck converter is voltage step down and current step up dc-dc converter. The device can be considered as a pulse width modulator followed by a low-pass filter. Similar to the boost converter, the schematic of Fig. 5.5 contains two non-linear elements the diode and the MOS transistor which is driven by a periodical square wave with period T and frequency $T = 1/f_c$. According to the previous example the duty cycle of the square wave signal defines the ratio between the turn on and the turn off time interval of the MOS component.

A buck converter operates in CCM, if the current through the inductor never falls to zero during the commutation cycle. In this mode, the operating principle is described by the following two phases:

1. *the inductor charge phase*: the MOS is turned on and the diode is reversed biased by the voltage source E. The input energy is transferred concomitantly to the inductor L by charging it and to the load R. The current through the inductor i_L rises linearly. It is natural to expect that v_c is lower than E;

2. *the inductor discharge phase*: the MOS is turned off, the inductor current continues to flow turning on the diode. The inductor L is discharged into the RC parallel. The current trough the inductor i_L decreases to the minimum value.

Similar to the previous example, the frequency-domain representation of the converter of Fig. 5.5 is obtained by substituting the MOS and the diode of the circuit with two periodic switching element Y_1 and Y_2 and by replacing the voltage source E and the MOS by a Norton equivalent, as shown in Fig. 5.6.

The schematic provides a time-invariant representation of the converter that can be analyzed by the following augmented MNA equation:

$$\left[\begin{array}{c:c:c} \mathbf{Y_1 + Y_2} & \mathbf{0} & \mathbf{1} \\ \hdashline \mathbf{0} & j\boldsymbol{\omega}C + G\mathbf{1} & -\mathbf{1} \\ \hdashline \mathbf{1} & -\mathbf{1} & -j\boldsymbol{\omega}L \end{array}\right] \left[\begin{array}{c} \boldsymbol{V}_1 \\ \hdashline \boldsymbol{V}_2 \\ \hdashline \boldsymbol{I}_L \end{array}\right] = \left[\begin{array}{c} \boldsymbol{Y_1 E} \\ \hdashline \mathbf{0} \\ \hdashline \mathbf{0} \end{array}\right] \tag{5.2}$$

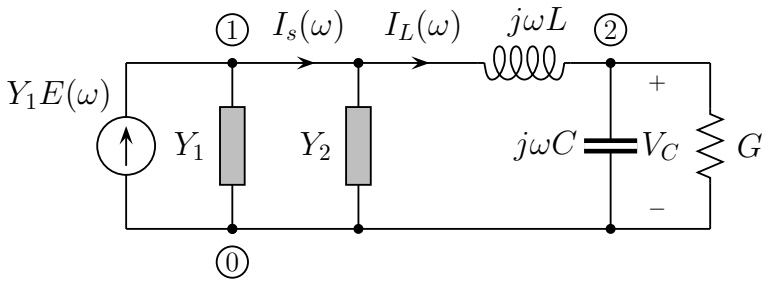

Figure 5.6: Frequency-domain representation of the buck converter of Fig. 5.5 where the PSL elements are replaced by their time-invariant augmented admittances Y_1 and Y_2.

The current $I_s(\omega)$ can be simply computed from the variables of MNA equations by the following relations:

$$I_s(\omega) = Y_1(E(\omega) + V_1(\omega)) \tag{5.3}$$

The proposed analysis is validated by considering the following parameters of the schematic of Fig. 5.5: $E = 45$ V, $L = 120\,\mu$H, $C = 33\,\mu$F, $R = 100\,\Omega$, $f_c = 250$ kHz and $D = 50\%$.

Fig. 5.7 and 5.8 show a comparison between the predicted and the reference responses of the current $i_s(t)$ and the voltage $v_c(t)$ of Fig. 5.5 both in time- and frequency-domain. The reference curves are obtained by a classical time-domain ODE simulation ($t_{step} = 5$ ns) in MATLAB environment.

Also in this example, the curves highlight the good accuracy of the proposed solution in reproducing the steady-state responses of the buck converter without including the transient portion observed in the reference responses. Unfortunately, different from the previous example the analysis required a high expansion order $N = 500$ since the spectrum of the input current $i_s(t)$ of the converter contains high-frequency components. As far as the accuracy and the efficiency is concern a speed-up of $300\times$ (0.05 s) and a mean square error $< 3\%$ only is achieved.

The simulation results are obtained by a MacBook Pro (Intel Core i5 running @2.4GHz, 4GB RAM).

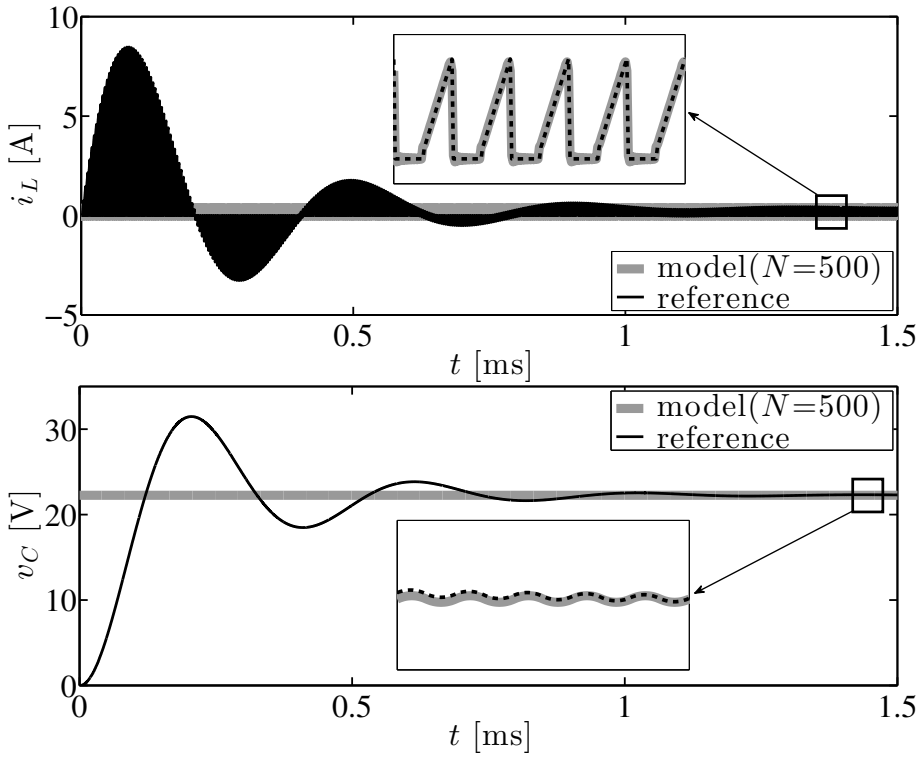

Figure 5.7: Time-domain responses of the current $i_L(t)$ and the voltage $v_C(t)$ of the circuit in Fig. 5.5. Dashed black: reference; solid gray: prediction with expansion order $N = 500$.

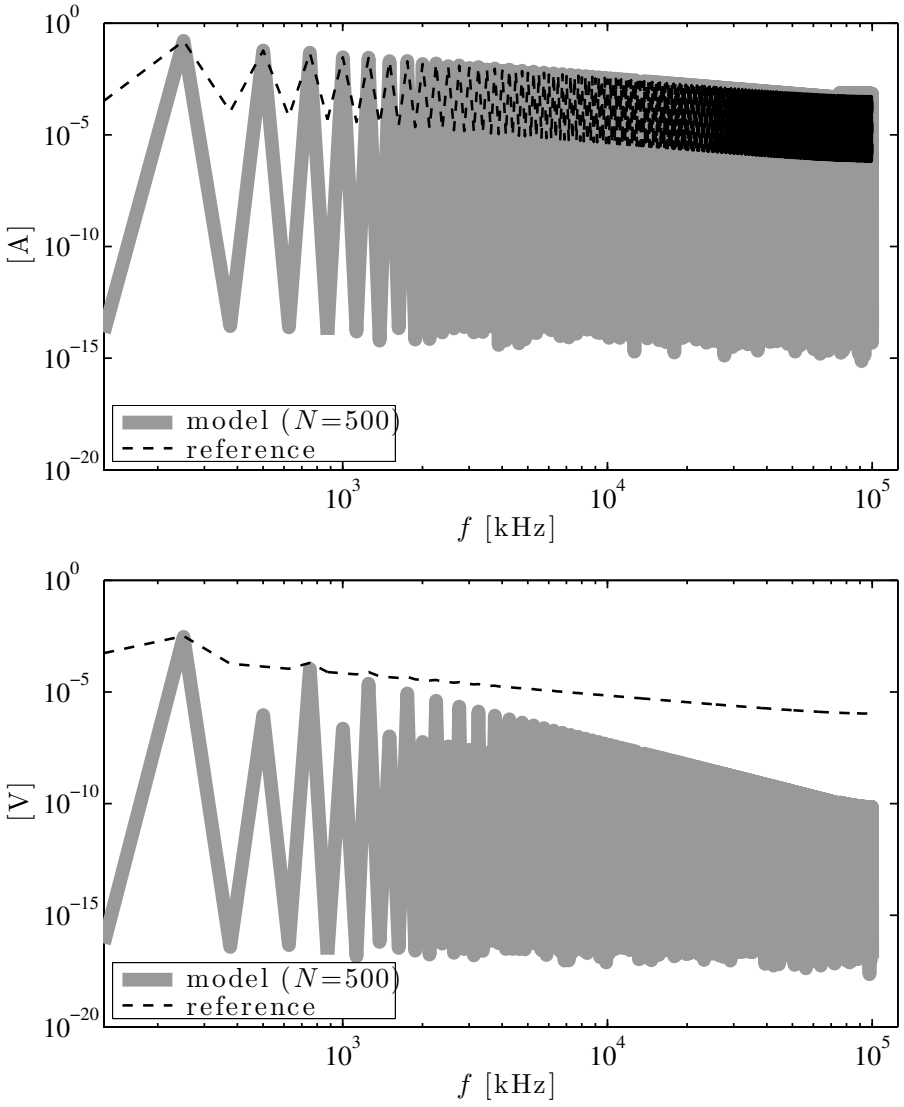

Figure 5.8: Frquency-domain responses of the current $I_L(f)$ and the voltage $V_C(f)$ of the circuit in Fig. 5.5. Dashed black: reference; solid gray: prediction with expansion order $N = 500$.

5.3 Example 3: Cuk converter

This Section focuses on the analysis and the simulation of the *Cuk converter* shown in Fig. 5.9 operating in continuos conduction mode (CCM).

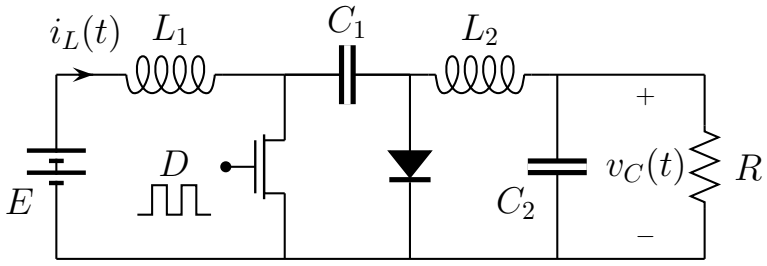

Figure 5.9: Schematic of a dc-dc cuk converter with its relevant electrical variables and components.

The considered dc-dc converter corresponds to a series interconnection of a boost converter (see Sec. 5.1) followed by a buck converter (see Sec. 5.2) with a transfer capacitor C_1 to couple the energy, unlike most other types of converters which use an inductor. The non-isolated Cuk converter can only have opposite polarity between input and output. Also in this case, at the steady-state the two non-linear elements of the circuit can be substituted by two periodic switches with switching frequency $f_c = 1/T$ defined by the frequency of the square wave control signal of the MOS transistor.

The operating principle of the Cuk converter can be summarized by the following two phases:

1. *the transfer capacitor charge phase*: the MOS is turned off, the inductor currents flow through the diode and energy is stored in the transfer capacitor C_1 from the input voltage source E and the inductor L_1. Instead the energy stored in the inductor L_2 is transferred to the output. As a results, both the inductor currents are linearly decreasing.

2. *the transfer capacitor discharge phase*: the MOS is turned on, the inductor currents flow through the transistor and the transfer capacitor C_1 discharged while energy is stored in the inductor L_1. As the capacitor C_1 discharges through the transistor, energy is stored in the inductor L_2. Consequently, both of the inductor currents are linearly increasing.

Similar to the previous example, the time-invariant augmented MNA equation of the considered Cuk converter of Fig. 5.9 is obtained by replacing the non-linear elements of the circuit with two periodic switches described by their augmented admittance characteristics. The MNA equation is then validated by considering the time- and frequency-domain behavior of the input current i_L and the output voltage v_c. In the following results, the circuit elements of Fig. 5.9 take the following values: $E = 15\,\text{V}$, $L_1 = 180\,\mu\text{H}$, $C_1 = 220\,\mu\text{F}$, $L_2 = 150\,\mu\text{H}$, $C_2 = 220\,\mu\text{F}$, $R = 10\,\Omega$, $f_c = 25\,\text{kHz}$ and $D = 50\%$.

Fig. 5.10 and 5.11 collect the comparison between the predicted and the reference time and frequency-domain responses for the current $i_L(t)$ and $v_C(t)$, where the reference results are computed by means of a MATLAB time-domain simulation based on classical ODE methods ($t_{step} = 0.1\,\mu\text{s}$).

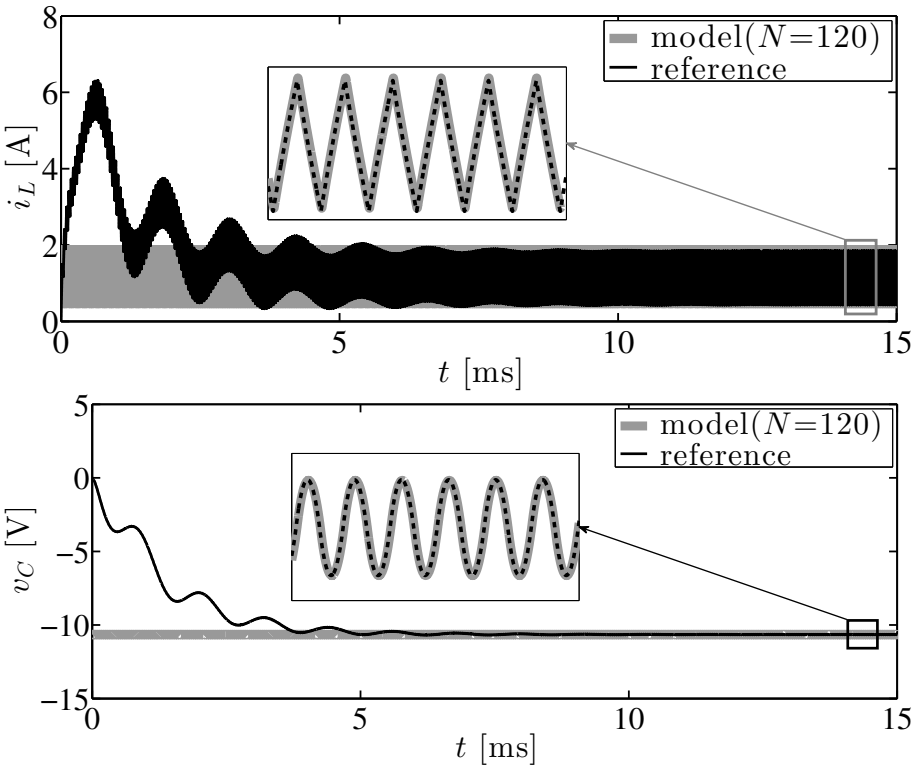

Figure 5.10: Time-domain responses of the current $i_L(t)$ and the voltage $v_C(t)$ of the circuit in Fig. 5.9. Dashed black: reference; solid gray: prediction with expansion order $N = 120$.

The results highlight the good accuracy of the proposed solution in reproducing the steady-state responses of the cuk converter without including the transient portion observed in the reference time-domain responses. As far as the accuracy and the efficiency is concern a speed-up of $260\times$ (0.05 s) and a mean square error $< 2\%$ only is achieved by considering an order expansion $N = 120$.

The simulation results are obtained by a MacBook Pro (Intel Core i5 running @2.4GHz, 4GB RAM).

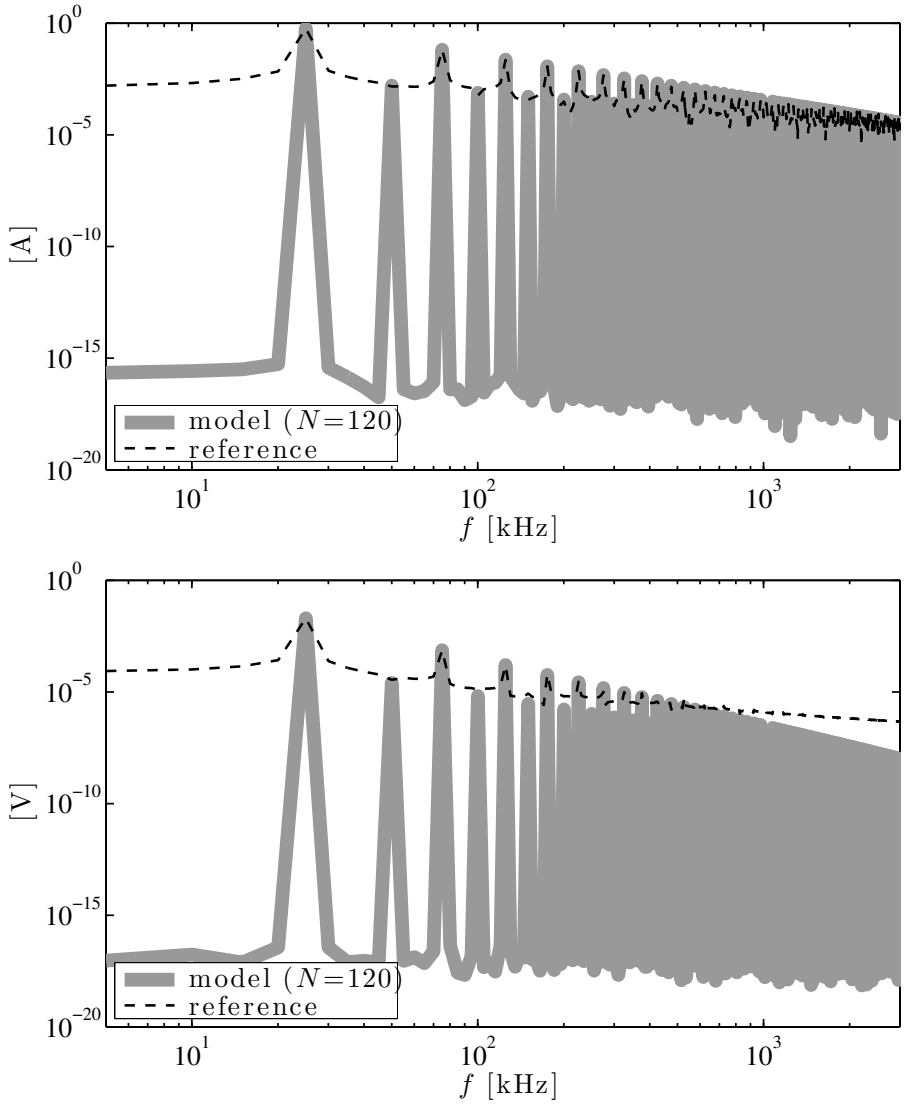

Figure 5.11: Frequency-domain responses of the current $i_L(t)$ and the voltage $v_C(t)$ of the circuit in Fig. 5.9. Dashed black: reference; solid gray: prediction with expansion order $N = 120$.

5.4 Example 4: PWM Single Phase Inverter

For the sake of simplicity, so far we limited the proposed method to the analysis of PSL circuits where the switching elements are characterized by a single periodic commutation during the period T. In this Section, the considered approach is extended to the case of pulse-width modulated (PWM) switches, that present multiple commutations during a single period. The discussion is based on the PWM full-bridge single phase inverter [43] of Fig. 5.12.

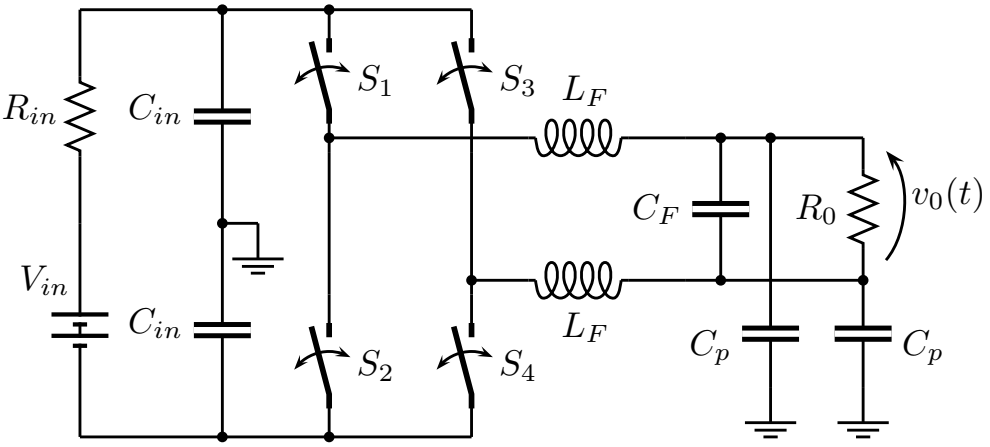

Figure 5.12: Schematic of a PWM full-bridge single inverter with its relevant electrical variables and components.

The single phase inverter is a dc-ac switching converter consisting of the interconnection of a voltage generator (here represented by the independent voltage source $V_{in} = 15\,\mathrm{V}$ connected in series with its internal resistor R_{in}) driving the input capacitive block (capacitor C_{in} in the schematic) in parallel with the so-called "H-bridge" switching structure. This block is connected on the right-hand side to the output resistor R_0 through a low-pass LC filter. The circuit elements take the following values: $V_{in} = 15\,\mathrm{V}$, $R_{in} = 1\,\Omega$, $C_{in} = 47\,\mu\mathrm{F}$, $L_F = 2\,\mathrm{mH}$, $C_F = 30\,\mu\mathrm{F}$, $C_p = 300\,\mathrm{pF}$ and $R_0 = 20\,\Omega$.

The switches S_k, $k = 1, \ldots, 4$ are driven by four PWM signals obtained according to the waveforms shown in Fig. 5.13. Specifically, the switches operation is derived by comparing a reference sinusoidal signal $r(t)$ with a companion carrier function $c(t)$ defined by a periodic triangle function of frequency f_c. As an example, the time-domain behavior of the switches S_1 and S_3 of the H-bridge is shown in Fig. 5.14. This is defined by means of the functions $\Pi_1(t)$ and $\Pi_3(t)$, which are given by the following relations:

$$\Pi_1(t) = \begin{cases} 1, \text{ if } r(t) > c(t) \\ 0, \text{ otherwiswe} \end{cases} \tag{5.4}$$

$$\Pi_3(t) = \begin{cases} 1, \text{ if } r(t) > -c(t) \\ 0, \text{ otherwise} \end{cases} \tag{5.5}$$

The behavior of the remaining switches S_2 and S_4 is defined by the functions $\Pi_2(t) = 1 - \Pi_1(t)$ and $\Pi_4(t) = 1 - \Pi_3(t)$, which avoid a short circuit across the voltage source V_{in}.

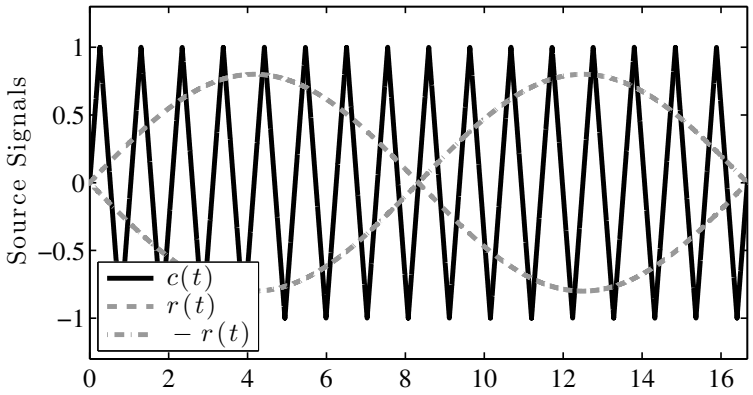

Figure 5.13: Reference 60 Hz sinusoidal signal and its companion carrier periodic triangular function with frequency $f_c = 960$ Hz.

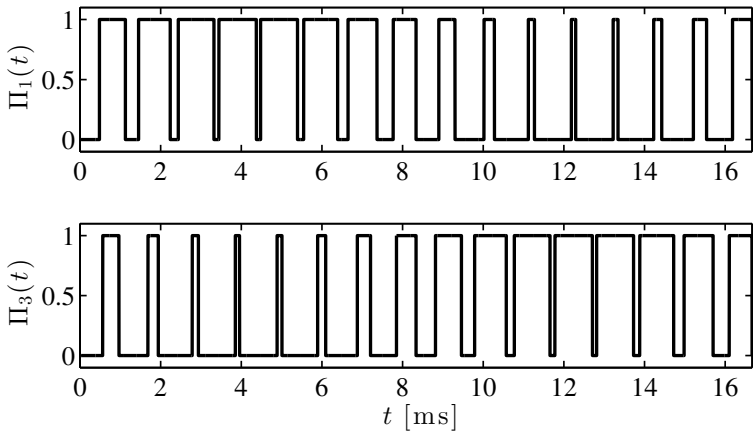

Figure 5.14: Operation of the switches S_1 and S_3 in the scheme of Fig. 5.12.

According to Chap. 3, the v-i characteristic of a generic periodic switch element can be defined by the following matrix relation:

$$\begin{bmatrix} I_{-N} \\ \vdots \\ I_0 \\ \vdots \\ I_N \end{bmatrix} = \begin{bmatrix} Y_0 & Y_{-1} & \dots & \dots & Y_{-2N} \\ Y_1 & Y_0 & \dots & \dots & \vdots \\ \vdots & \vdots & \ddots & \vdots & \vdots \\ \vdots & \vdots & \vdots & \ddots & Y_{-1} \\ Y_{2N} & \dots & \dots & Y_1 & Y_0 \end{bmatrix} \begin{bmatrix} V_{-N} \\ \vdots \\ V_0 \\ \vdots \\ V_N \end{bmatrix}, \tag{5.6}$$

where $Y_n = G_n + jB_n$ are complex numbers computed as the Fourier coefficients of the time-domain periodic behavior of the switch admittance as follows:

$$Y_n = \frac{1}{T}\int_0^T \frac{1}{R_{on}}\Pi(t)\exp(-jn\omega_c t)dt. \tag{5.7}$$

Obviously, the behavior of the functions $\Pi(t)$ for PWM switches is more complicated than the simple window functions considered in Chap. 3. In principle, the behavior of a generic binary switching element can be interpreted as a sum of single commutation window functions $\Pi_{\Delta_k}(t - t_k)$:

$$\Pi(t) = \sum_{k=1}^{M} \Pi_{\Delta_k}(t - t_k) \tag{5.8}$$

where M is the number of commutations occurring in a single period. Thanks to the linearity of the Fourier operator, the coefficient Y_n of (5.7) are in turn computed as a superposition of the analytical result provided in the previous Chapters of this thesis (3.7). Nonetheless an alternative and more practical approach is to numerically compute these entries by replacing the continuos-time Fourier transform (5.7) with a discrete Fourier transform (DFT) via the following relation:

$$Y_{MC,n} = \begin{cases} \dfrac{1}{R_{on}N_s}\displaystyle\sum_{k=0}^{N_s-1}\Pi[k]\exp\left(-\frac{jk2\pi n}{N_s}\right) & \text{if } n \geq 0 \\ \dfrac{1}{R_{on}N_s}\displaystyle\sum_{k=0}^{N_s-1}\Pi[k]\exp\left(-\frac{jk2\pi(N_s+n)}{N_s}\right) & \text{if } n < 0 \end{cases} \tag{5.9}$$

where $N_s = 4N + 1$ and $\Pi[k] = \Pi(k\Delta_t)$ is the sampled version of the continuous signal $\Pi(t)$ on a single period T at equispaced intervals $\Delta_t = T/N_s$.

The number of samples N_s has to be greater than $4N + 1$ to obtain all the entries of the admittance matrix (5.6) (from Y_{-2N} to Y_{2N}). It is worth to remark that, since the spectrum of a generic switching signal $\Pi(t)$ is of infinite bandwidth, the sampling will inevitably lead to aliasing. In order to reduce the aliasing effect on the first $2N + 1$ harmonics of the spectrum of the discrete signal $\Pi[k]$, a number of samples $N_s > 8N$ is suggested [42].

The proposed approach is a generalization of the analytical formulation of the problem and allows to simplify the assessment of the frequency-domain equivalent of a switch element. It allows to replace the PWM time-varying behavior of the switches with their augmented admittance representations (5.6) to obtain a linear time-invariant equivalent of the PWM switching converter. Similar to the previous examples, the new augmented representation of the converter has been implemented in a MATLAB script by means of an augmented MNA equation. Figures 5.15 and 5.16 collect the comparison between the reference and the predicted time- and frequency-domain responses of the load voltage $v_0(t)$. The curves in the figures highlight the good accuracy of the proposed solution in reproducing the steady-state response of the circuit via the proposed interpretations, without the initial transient.

The expansion order is set to a sufficient large value $N = 180$ to account for the high frequency components of the steady-state response, leading to a maximum absolute error computed as the difference between the reference and the predicted steady-state responses that is below 1%. It is important to remark that the proposed method achieves a speed-up of $30\times$ with respect to the

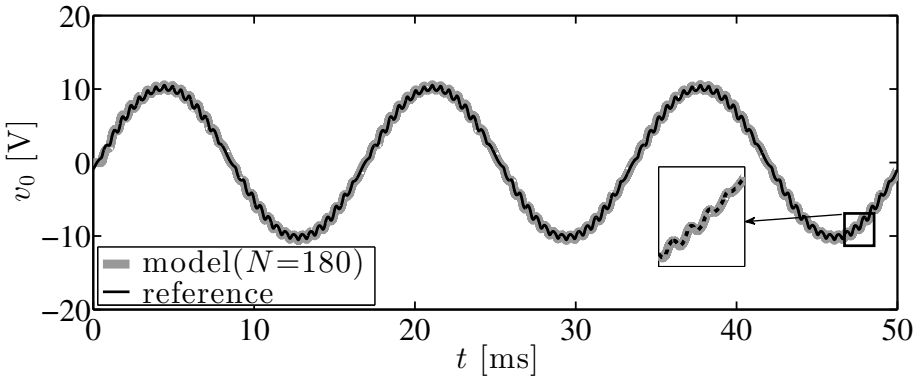

Figure 5.15: Time-domain responses of the output voltage $v_0(t)$ of the circuit in Fig. 5.12. Solid gray: reference; Dashed black: prediction with expansion order $N = 180$.

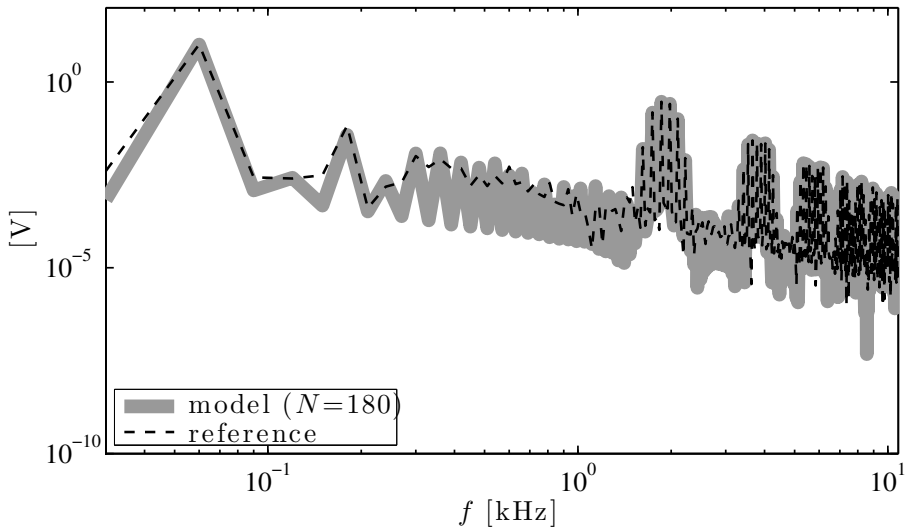

Figure 5.16: Frequency-domain responses of the output voltage $v_0(t)$ of the circuit of Fig. 5.12. Dashed black: reference; solid gray: prediction with expansion order $N = 180$.

reference the ODE time-domain simulation ($t_{step} = 0.1\,\mu$s) with a total simulation time of $1.04\,$s only, providing both the time- and frequency-domain responses of all the variables of the circuit, independently from the considered time-step.

The simulation results are obtained by a MacBook Pro (Intel Core i5 running @2.4GHz, 4GB RAM).

5.5 Chapter Summary

In this Chapter the frequency-domain method proposed in this thesis is applied to four switching converters consisting of classical LTI components and switches driven by periodic single or multiple commutation events. A robust framework is derived, where the original time-varying circuit is interpreted in terms of an augmented LTI equivalent system. The new variables correspond to the harmonics of the steady-state circuit responses and are calculated via a single system inversion. The method provides remarkable accuracy and improved efficiency with respect to the standard solutions based on the time-domain simulation of the switching circuit.

Chapter 6

EMI Prediction via Numerical Simulation

Switching power converters are massively used in almost any electrical and electronic equipment and appliances. This class of circuits are inherently time-varying systems that are characterized by the periodic activity of their internal switches which leads to discontinuous absorbed currents. The above currents, that play the role of high frequency noisy disturbances feeding the power distribution system, become a serious concern for designers that need to comply with the EMC regulation for the CE.

This Chapter addresses the analysis and the simulation of the CE produced by switching circuits by means of the proposed augmented representation. Different from the state-of-the-art methods, the augmented interpretation is an alternative solution to the direct frequency-domain EMI analysis of switched circuits. A dc-dc boost converter is considered and the results obtained from the PSL analysis are validated by means of real measurements.

The Chapter is organized as follows. In the Sec. 6.1 the standard setup for the measurement of the CE is presented. Section 6.2 introduces the EMI generation process characteristic of the switching converter and proposes an alternative augmented model for the prediction of the CE generated from a test-case boost converter. The obtained results are validated by means of real measurements.

6.1 Measurement Setup for Conducted Emissions

The propose measurement setup is used to verify compliance of the CE with the regulatory limits. The FCC and the CISPR–22 standards limit the CE from $150\,\text{kHz}$ to $30\,\text{MHz}$ [46, 47].

For the verification of compliance with the regulatory limits, the CE have to be measured with a line impedance stabilization network (LISN) inserted between the supply main and the device under test (DUT) [48]. A typical test configuration is illustrated in Fig. 6.1.

As illustrated in Fig. 6.1, also in this Section the voltage and current variables are represented in frequency-domain by their Fourier harmonics.

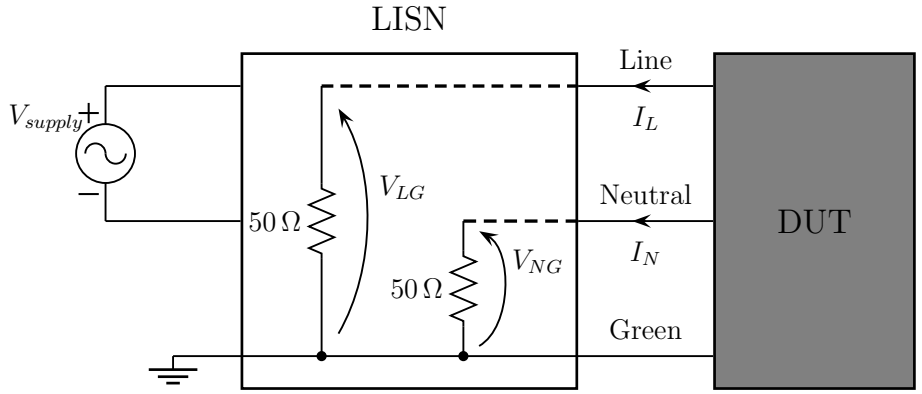

Figure 6.1: Measurement setup for the characterization of CE according to the FCC and CISPR–22 standards.

6.1.1 The Line Impedance Stabilization Network (LISN)

The purpose of the conducted emission testing is to measure the noise currents that flow from the DUT power cord to the supply main. Different from standard current measurements, the characterization of the CE needs to be performed for a fixed loading condition at the input port the DUT in order to ensure the repeatability of the measurement in different environments. Obviously, the impedance of the supply network varies in time and depends on the devices connected to network. Also the amount of noise that is present on the power system net varies from sites to sites, thus it needs to be removed from the measurement results.

In order to univocally define the measurement conditions for the characterization of the CE, a LISN has to be inserted into the measurement setup (see Fig. 6.1). The main functions of the LISN can be summarized as follows:

- to provide a precise impedance of $50\,\Omega$ to the power input of the DUT for the entire bandwidth of the CE (from $150\,$kHz to $30\,$MHz), to get repeatable measurements of the DUT noise present at the LISN measurement port;
- to prevent the high-frequency noise of the power source from coupling in the system. In fact the LISN provides a high impedance to the *external* noise while allowing the low-frequency power to flow through the DUT;
- to prevent the external currents in the frequency range of the regulatory limit from flowing through the $50\,\Omega$ resistors of the LISN. Emissions outside the frequency range of the regulatory limit are of no concern with regard to meeting the conducted emission limit.

The LISN specified for the use in the conducted emission measurements is shown in Fig. 6.2.

The schematic shows as the external high-frequency noise that comes from the supply main is short circuited by means of the $1\,\mu$F capacitor, which prevents that noise from flowing through the measurement device and contaminating the test data. Also the supply main is isolated from the noisy currents generated by the DUT by means of the $50\,\mu$H inductors, therefore the high-frequency CE are forced to flow through the $50\,\Omega$ resistors. Instead the $0.1\,\mu$F capacitors prevent

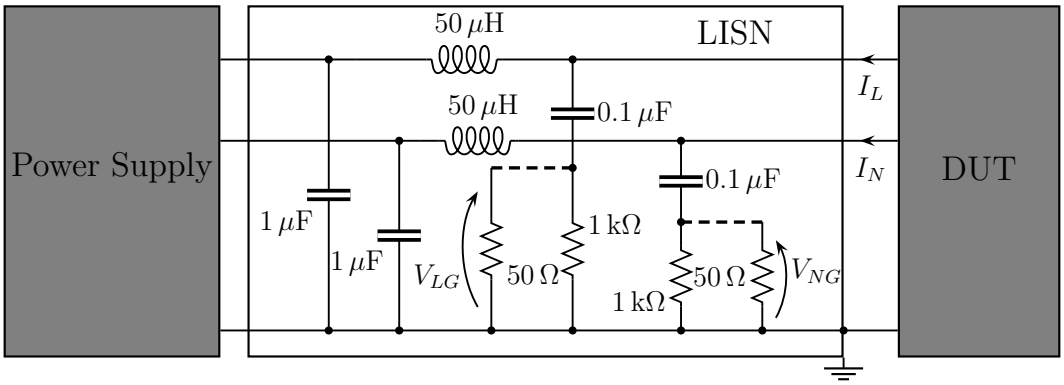

Figure 6.2: Illustration of the LISN schematic.

any dc signals from overloading the input of the test receiver avoiding possible damages of the instrumentation connected to the $50\,\Omega$ resistors.

The CE currents I_L and I_N are related to the voltages V_L and V_N measured at the output of the LISN by:

$$V_L = 50 I_L \tag{6.1}$$

$$V_N = 50 I_N \tag{6.2}$$

where the $0.1\,\mu$F capacitors are considered as short-circuits over the entire bandwidth of CE regulation and the $50\,\mu$H inductors are seen as open-circuits.

6.1.2 Differential- and Common-Mode Disturbances

The differential mode (DM) and the common mode (CM) analysis of the CE of the DUT is simplified by considering the LISN as a $50\,\Omega$ load between the line wire and the green wire and between the neutral wire and the green wire as shown in Fig. 6.3.

The currents I_L and I_N can be decomposed in terms of the DM and CM current components I_D and I_C by the following relations:

$$I_L = I_C + I_D \tag{6.3}$$

$$I_N = I_C - I_D \tag{6.4}$$

the above equation can be re-written as:

$$I_D = \frac{1}{2}(I_L - I_N) \tag{6.5}$$

$$I_C = \frac{1}{2}(I_L + I_N). \tag{6.6}$$

According to (6.1) and (6.2), the voltages V_{LG} and V_{NG} measured at the output terminals of the LISN can be defined through the the differential and common mode currents as follows:

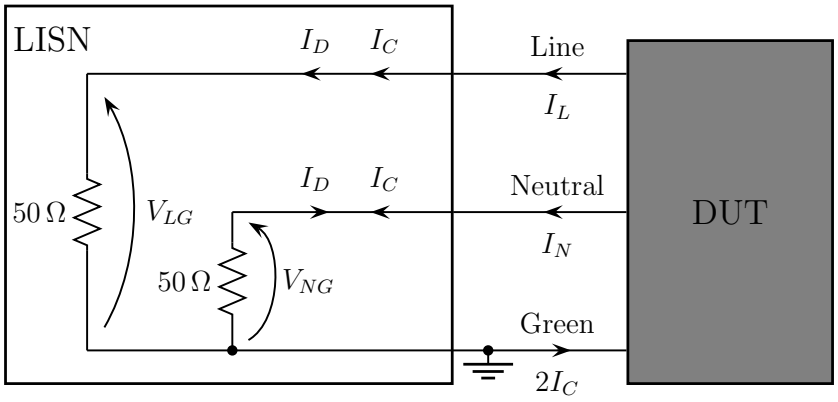

Figure 6.3: Illustration of the contributions of DM and CM current components on the measured CE.

$$V_{LG} = 50(I_C + I_D) \tag{6.7}$$

$$V_{NG} = 50(I_C - I_D) \tag{6.8}$$

Thus the common mode noise and the differential mode noise can be estimated by the voltage of the LISN by the following relations:

$$V_D = \frac{1}{2}(V_{LG} - V_{NG}) \tag{6.9}$$

$$V_C = \frac{1}{2}(V_{LG} + V_{NG}). \tag{6.10}$$

6.2 EMI Assessment of a Real Switching Converter

Switching converters introduced in Chap. 5 are of widespread use in modern days because they present significant benefits in reduction of the physical sizes and high efficiency comparing to the linear regulator classically used in linear power supplies. With this benefits comes a major drawback *noise*. Due to their inherent switching nature the considered converters are one of the principal source of noise into the distribution network. For this class of devices, the required output voltage is obtained from high-frequency commutations of the configuration of the circuit that leads to fast transitions of the voltage and the current waveforms (high dv/dt and di/dt). The fast transitions are the cause of the broadband electromagnetic disturbances (EMD) as CE.

In this Section, the proposed method for the frequency-domain analysis of switching circuits is applied for the assessment of DM noise spectrum of a *real dc-dc boost converter* in the typical configuration for CE measurement of Fig. 6.4, according to Sec. 6.1.

The parameters and operating conditions defining this example test case are the following: the converter operates in CCM at $f_c = 40\,\text{kHz}$ with duty cycle $D = 45\%$; the input voltage $E = 20\,\text{V}$ is applied through the LISN. The converter is composed of a load resistor ($R_0 = 300\,\Omega$), a boost inductor ($L_{boost} = 470\,\mu\text{H}$, $R_{lp} = 1.3\,\Omega$ and $C_{lp} = 27\,\text{pF}$), the output capacitor ($C_0 = 470\,\mu\text{F}$,

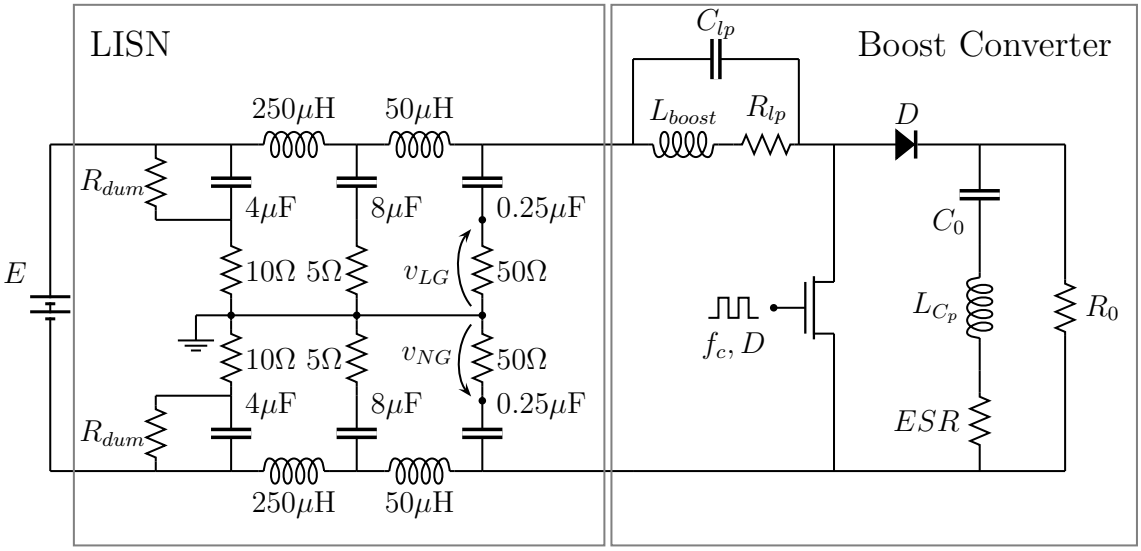

Figure 6.4: Schematic representing the typical setup for the measurement of the DM emissions of a switching power converter via a LISN network in standard configuration. The example dc-dc boost circuit of Sec. 6.2 is considered in this study (see text for details).

$L_{cp} = 25\,\text{nH}$ and $ESR = 280\,\text{m}\Omega$), diode (BYW77P-200) and MOSFET (IRFP250N). The parasitic elements of the boost inductor and the output capacitor are extracted from their datasheet. The reference frequency-domain response of the DM noise is obtained from the time-domain measurements by means of the equation (6.9) and of the FFT routine via a MATLAB script. According to the procedure of Chap. 4, the augmented LTI equivalent built from the schematic of Fig. 6.4 is generated.

Figure 6.5 shows the comparison between the reference and predicted time-domain responses of the DM noise voltage $v_{DM}(t)$. From the curves in this figure, it is clear that the proposed solution allows to generate accurate predictions with a tunable accuracy that can be chosen via the expansion order N. The bottom panel of Fig. 6.5 highlights that $N = 100$ is enough to describe the signature of the DM noise without the spurious spikes. To achieve a better accuracy, the expansion order unavoidably needs to be increased to a much larger value (e.g., $N = 1000$). In the latter case, the agreement is excellent and the measured responses are very well reproduced by the prediction.

Similarly, Fig. 6.6 collects a similar comparison for the case of the frequency-domain spectrum of the DM noise, thus confirming the accuracy of the predicted responses in reproducing both the envelope and the notches of the reference curve. From the curves in Fig. 6.6 it is even more evident that the expansion order should be large enough to cover the entire bandwidth required for the characterization of the conducted emissions spectrum (i.e., 150 kHz–30 MHz). It is relevant to remark that the largest harmonic of a series expansion like (4.4) is located at $f_{\max} = f_0 + Nf_c$. In the boost example, with a constant voltage excitation E (i.e., a cisoidal signal at $f_0 = 0\,\text{Hz}$) the minimum number of harmonics spanning a 30 MHz bandwidth turns out to be $N \geq (30\,\text{MHz}/f_c = 750)$.

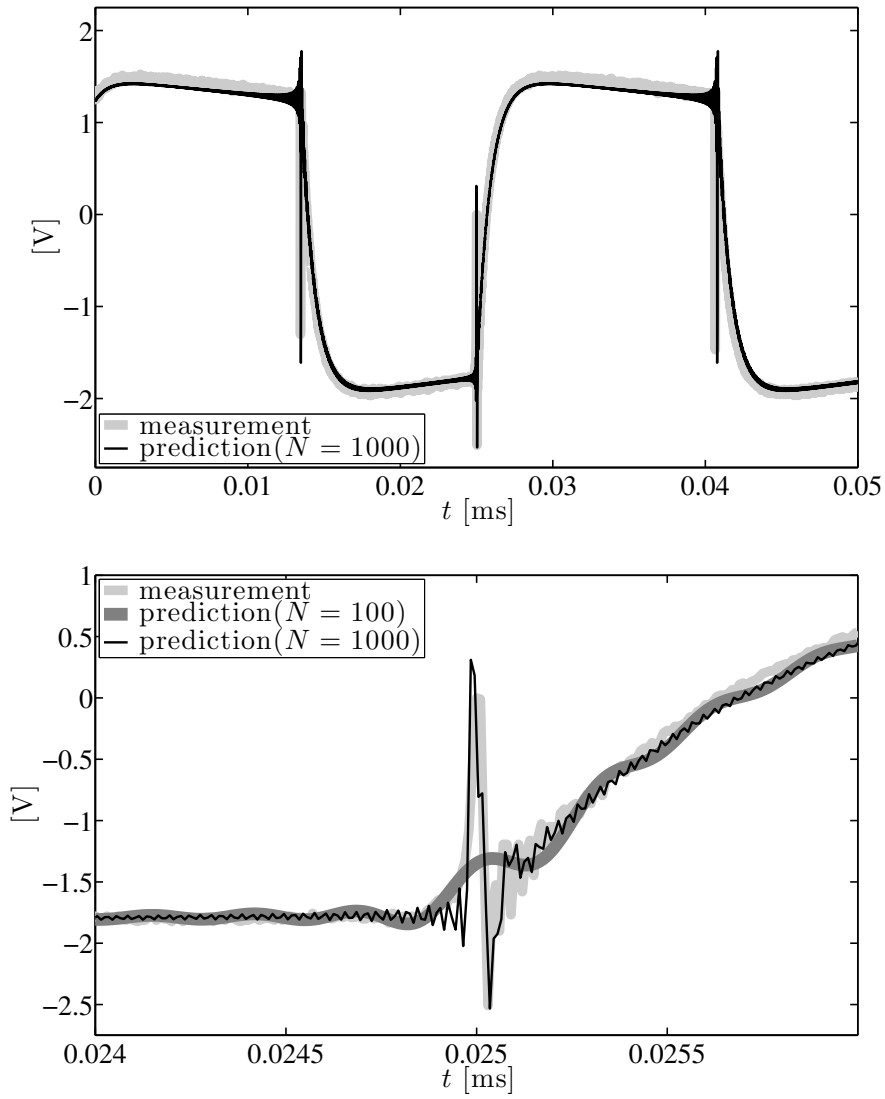

Figure 6.5: DM noise voltage response $v_{DM}(t)$ of the example test case of Fig. 7.1. Light gray: measurement; dark gray: prediction ($N = 100$); black thin: prediction ($N = 1000$).

The obtained results show that the proposed method allows to model the non-ideal switching behavior of the diode due to the diffusion of carriers in the turn-on process and to the charge stored in the depletion region during the conduction operation, without changing the structure of the MNA matrix. In fact the non-ideal commutation behavior of the diode is the cause of the voltage spikes in time-domain waveform at the commutation instants (see Fig. 6.5), that are related to periodic time-slots ($\simeq$ 7 ns), where the two switches are both closed or open. Figure 6.5(bottom panel) provides the high-frequency nature of the spikes which do not appear in the response computes with an expansion of order $N = 100$.

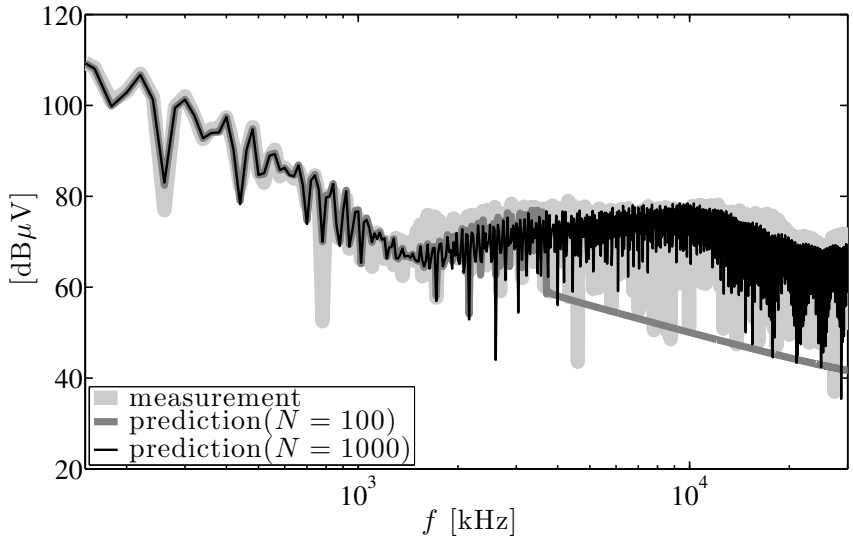

Figure 6.6: Frequency-domain spectrum of DM noise voltage response $v_{DM}(t)$ of the example test case of Fig. 7.1. Light gray: measurement; dark gray: prediction ($N = 100$); black thin: prediction ($N = 1000$).

To conclude the comparison, Tab. 6.1 summarizes the main figures of the efficiency and covered bandwidth of the proposed method, for an increasing number of the expansion order N. The numbers in the table, that are obtained by a MacBook Pro (Intel Core i5 running @2.4 Ghz, 4 GB RAM), highlights a good CPU time in generating the steady-state response of the example test circuit for any value of N. However, even if a large expansion number is considered the EMI prediction is always achieved in less than 10 s.

Table 6.1: Figures summarizing the efficiency of the proposed method and the covered bandwidth for an increasing number of the expansion order N (see text for details).

N	CPU time	Bandwidth
10	0.016 s	366 kHz
20	0.039 s	732.6 kHz
100	0.23 s	3.66 MHz
200	0.25s	7.32 MHz
500	1.08 s	18.31 MHz
1000	9.79 s	36.63 MHz

6.3 Chapter Summary

This Chapter addressed the modeling and simulation of the steady-state response of a switching circuit with the aim of predicting its EMI disturbances feeding the power distribution network. The proposed approach provides an alternative yet effective solution to this problem that is based on the generation of an augmented linear time-invariant equivalent. The solution of the above augmented network via an augmented version of the MNA tool at a single frequency point allows to compute the harmonic coefficients of the steady-state noisy current generated from the switching converter. Predicted responses are compared with measured data, thus yielding to a remarkable accuracy and good simulation time.

Chapter 7

EMI Modeling from Measured Data

This chapter addresses the modeling of the CE produced by circuits characterized by a periodic switching behavior. The proposed approach is based on the theory of PLTV systems [2, 3, 5, 11, 10, 12, 17, 19] introduced in Chap. 2 and on the estimation of an augmented impedance or admittance *equivalent* of the switching circuit by means of real measurements. Different from the state-of-the-art time-invariant behavioral models, the considered approach takes into account the inherent time-varying nature of the switching devices and allows for the full characterization of the CE disturbances via a well-defined modeling procedure. The strength and the accuracy of the method are verified on a dc-dc boost converter via real measurement data.

The Chapter is organized as follows. Section 7.1 describes the power converter used in this study to demonstrate the proposed method and to provide a comparison of the obtained models with the state-of-the-art LTI approximations introduced in Sec. 7.2. Sections 7.3 and 7.4 extend the well-known impedance and admittance concepts defined for the LTI circuits to the more general PLTV case and present an alternative black-box strategy for model generation. Validation results based on real measurements and model predictions are presented in Section 7.5. Section 7.6 collects useful remarks justifying the assumed model structure and discusses the effects of its different constitutive parts on the predicted CE. Sec. 7.7 provides a summary of results and concludes the Chapter.

7.1 Application Test Case

This Section introduces the example test case used hereafter in this Chapter to illustrate the proposed modeling approach and to demonstrate its application to the prediction of the CE in switching devices. Similar to the previous Chapter the discussion is based on the dc-dc boost converter of Fig. 7.1 sharing the same key features of the absorbed current of the typical switching circuits connected to the supply main. In order to model the CE of the boost example, i.e., to fully describe the frequency spectrum of the current $i(t)$, the converter is seen as a black-box circuit element characterized by it external i-v relationship.

The converter is designed to operate in continuous mode at a switching frequency $f_c = 50\,\text{kHz}$, with duty cycle $D = 50\%$ and a nominal input voltage $v = 5\,\text{V}$. The circuit parameters are: $L = 470\,\mu\text{H}$, $C = 470\,\mu\text{F}$, $R = 150\,\Omega$, the diode model is FES16DT and n-channel MOS is

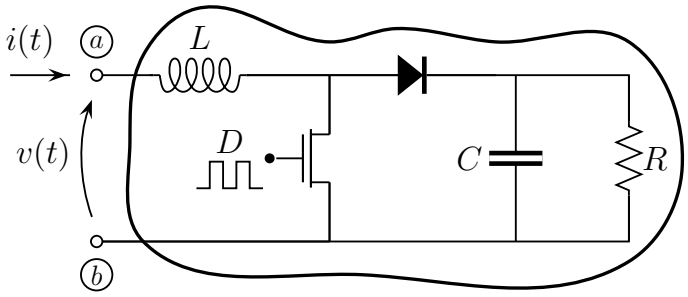

(a)

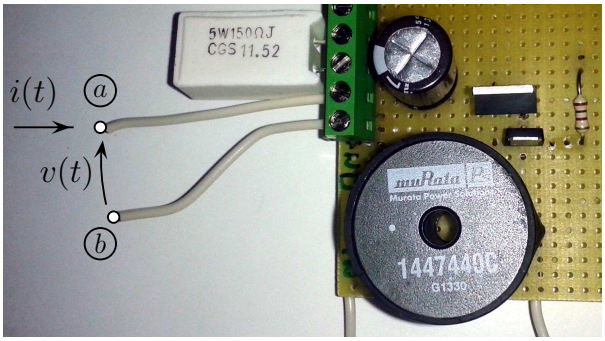

(b)

Figure 7.1: Example dc-dc boost converter used for illustrating the proposed modeling method. Panel (a): schematic; panel (b): test-board.

IRFU4105.

According to Chap. 5 the considered converter is seen as a PLTV circuit where the MOS and the diode are approximated by linear switches (see Fig. 7.2).

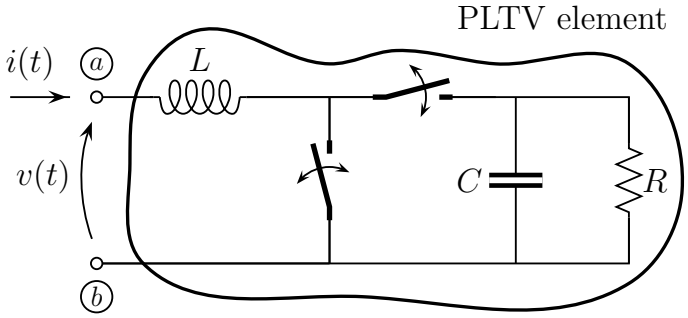

Figure 7.2: PLTV circuit interpretation of the boost example of Fig. 7.1.

7.2 State-of-the-art CE models

This Section focuses on the state-of-art approaches used to represent the port behavior of a switching circuit and to estimate its CE disturbances. According to [31, 32, 33, 34, 35, 36, 37], the CE in frequency-domain are in general modeled by means of LTI circuit elements based on the classical Thevenin- or Norton-like structures with possible modifications or improvements.

As an example, the input port behavior of the circuit of Fig. 7.1(a) can be approximated via the Norton-like element of Fig. 7.3. In the above simplified model the unknown parameters, i.e. the independent current source $I_N(\omega)$ and the impedance $Z_N(\omega)$, are computed from external observations. Specifically, the computation of the active source I_N is in general straightforward and comes directly form the interpretation of the above contribution as the spectrum of the short circuit current $i(t)$. For the class of dc-dc power converters it is approximated by the input current $i(t)$ recorded during standard working conditions, with a constant (i.e., dc) supply source feeding the converter. Different from the noise current source, there is not a clear and unique procedure for the computation of the equivalent impedance $Z_N(\omega)$. Most of the available approaches suggest suitable fitting or averaging techniques. In the latter case $Z_N(\omega)$ is seen as the average impedance carried out among all the impedances observed during the commutation of the device [31, 34]. Similar comments hold for alternative structures (like these based on Thevenin-like structures) and the reader should refer to [36, 37] for details.

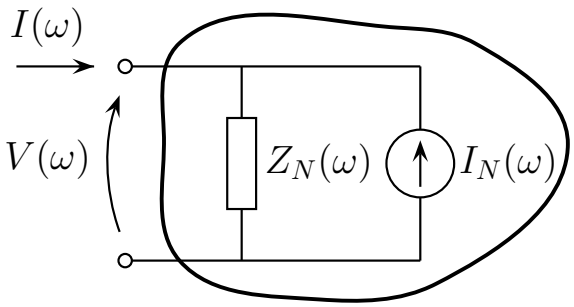

Figure 7.3: Time-invariant Norton-like structure hat can be used to model the port behavior of a switching device as the boost circuit of Fig. 7.1.

The characterization strategy for the generation of simplified LTI models is simple and in many cases gives good results. However, the proposed models are based on two erroneous assumptions:

1. **Time-invariant behavior**. It is not possible to define an equivalent LTI impedance (as $Z_N(\omega)$ in the scheme of Fig. 7.3) of a time-varying circuit element;

2. **Noisy source**. The model must be passive, in fact the device does not contain active elements like voltage or current generators (as $I_N(\omega)$).

The above two assumptions justify the possible strange and unpredictable behavior of these simplified models that is sometimes observed when the operating condition of the switching device changes from the one used for parameter estimation. As an example, Fig. 7.4 shows the reference and the predicted steady-state current responses of the example boost converter when a low-pass

RC filter ($R_F = 5\,\Omega$ and $C_F = 5\,\mu$F of Fig. 7.4a) and a high-pass RL filter ($R_F = 5\,\Omega$, $L_F = 5\,\mu$H and $R_L = 0.1\,\Omega$ of Fig. 7.4b) are interposed between the supply main and the converter. It is important to remark that the high-pass filter of Fig. 7.4b provides an unrealistic and extreme test case devised to stress the models performance. The curves in the figure clearly offer a visual check of the aforementioned behavior of the simplified structure-based models and provide a convincing motivation of the proposed study.

Summarizing, to further understand and to overcome the above limitations we need to improve the modeling strategy by fully exploiting the theory of time-varying circuits and systems.

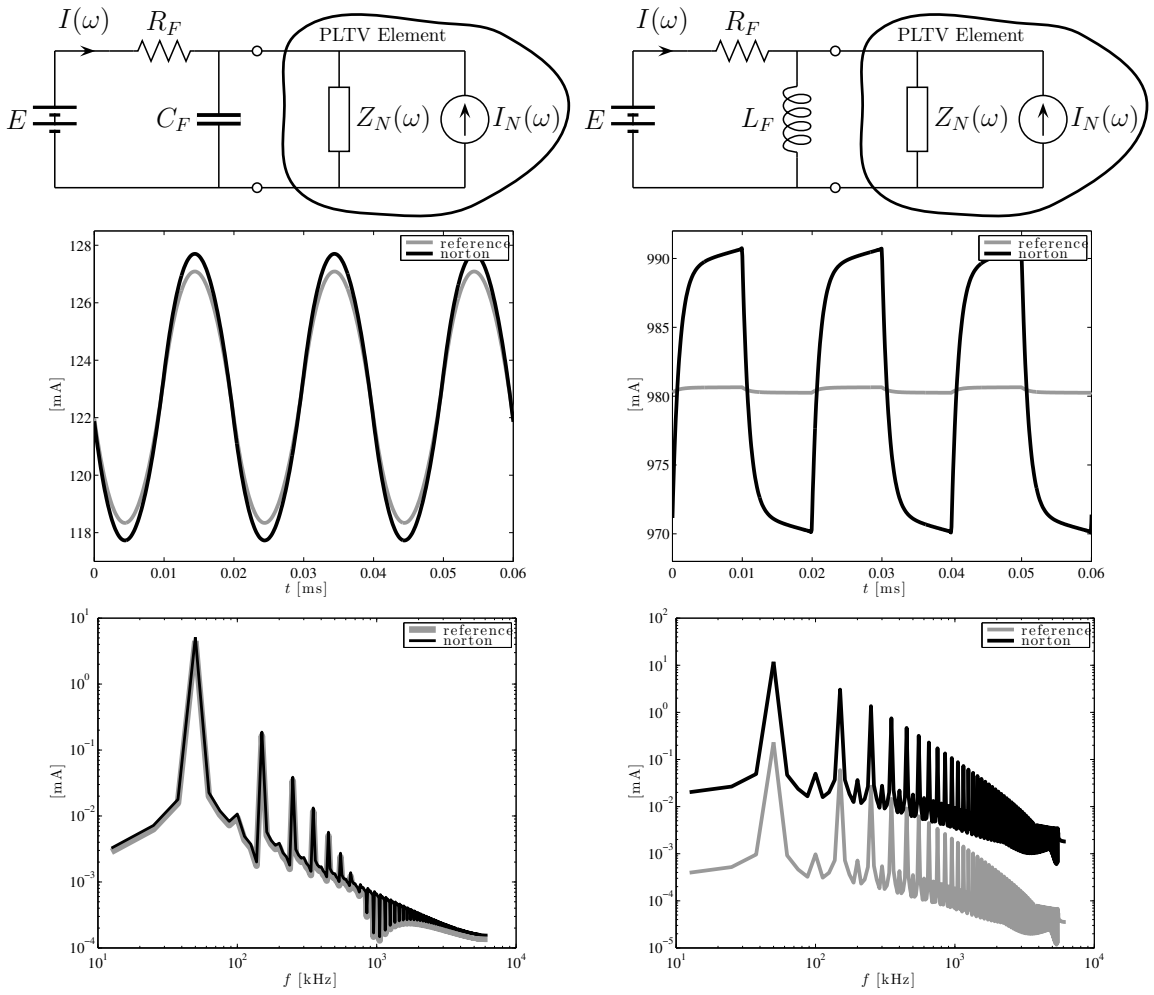

(a) RC filter with $R = 5\,\Omega$ and $C = 5\,\mu$F

(b) RL Filter with $R = 5\,\Omega$ and $L = 5\,\mu$H

Figure 7.4: Spectra and time-domain responses of current $I(\omega)$ supplied by the DC voltage generator when the boost converter in Fig. 7.1 is connected to two different RC and RL filters.

7.3 Constitutive Relations of PLTV Elements

This Section deals with the description of the v-i behavior of a generic PLTV element in terms of its augmented admittance or impedance representation according to mathematical framework introduced in Chap. 2 and in [2, 19].

The discussion starts with the well-known definition of the admittance $Y(\omega)$ of a two-terminal LTI element (e.g., the boost converter of Fig. 7.1(a) for a static configuration of the switches):

$$Y_{LTI}(\omega) = \frac{I(\omega)}{V(\omega)} = \left.\frac{i(t)}{v(t)}\right|_{v(t)=\exp(j\omega t+j\phi)}, \quad \forall \omega, \phi \in \mathbb{R}. \tag{7.1}$$

The above equation is based on the time-invariant property of LTI circuits, i.e., the voltage v and current i have the same frequency ω and the admittance $Y(\omega)$ is independent of the phase ϕ. According to the concept of the *time-varying transfer function* introduced in Chap. 2, the previous definition can be extended to the case of a linear time-varying (LTV) element by means of the following relation:

$$Y_{LTV}(t, \Omega) = \left.\frac{i(t)}{v(t)}\right|_{v(t)=\exp(j\Omega t+j\Phi)}, \quad \forall \Omega, \Phi \in \mathbb{R}. \tag{7.2}$$

The key underlying difference in the above two definitions is that the current response $i(t)$ of a LTV system depends both on the frequency Ω and on the phase Φ of the voltage excitation $v(t)$, thus on the time-instant when the excitation occurs. Owing to this, the time-varying activity of the system is taking into account by introducing the time variable t into the admittance operator $Y_{LTV}(t, \Omega)$.

In addition, for the important class of PLTV circuits, that are characterized by elements that periodically change their state or value with a period T, the time dependent admittance can be rewritten in terms of its Fourier expansion as follows [5, 11, 10, 12, 17, 19]:

$$Y_{PLTV}(t, \Omega) = \sum_{n=-\infty}^{+\infty} Y_n(\Omega) \exp(jn\omega_c t) \tag{7.3}$$

where $\omega_c = 2\pi f_c$ and $f_c = 1/T$.

It is important to remark that the time-varying admittance of (7.3) is a generalization of the augmented admittance representation of a resistive switch element introduced in Chap. 3 since the aliasing functions $Y_n(\Omega)$ are frequency dependent. Equation (7.3) is the admittance definition for a *generic dynamic PLTV element*.

Also in this case at the steady-state, the circuit response of a PLTV two-terminal element to a cisoidal voltage excitation $v(t)$ at angular frequency Ω can be defined as:

$$i(t; \Omega) \quad = \quad \sum_{n=-\infty}^{+\infty} I_n(\Omega) \exp\left[j(\omega - n\omega_c - \Omega)t\right] \tag{7.4}$$

where $I_n(\Omega)$ are the coefficients of a Fourier's series expansion centered at frequency Ω.

Substituting (7.3) and (7.4) into (7.2) leads to the following *generalization of the Ohm's law* (3.9) [19, 20].

$$\begin{aligned}&\sum_{n=-\infty}^{+\infty} I_n(\Omega)\exp(j(\Omega+n\omega_c)t) = \\ &= \sum_{n,m=-\infty}^{+\infty} Y_n(\Omega+m\omega_c)V_m(\Omega)\exp(j(\Omega+(n+m)\omega_c)t)\end{aligned} \tag{7.5}$$

The above equation clearly explains that the current response $i(t)$ of a PLTV element is the linear combination of all the harmonics of the voltage excitation $v(t)$.

In order to better understand the role of the mixed-domain admittance, the n-th harmonic of the current $i(t)$ writes:

$$I_n(\Omega) = \sum_{m+p=n} Y_p(\Omega+m\omega_c)\cdot V_m(\Omega) \qquad \text{for } n,m,p\in\mathbb{Z}. \tag{7.6}$$

By truncating the infinite series to $(2N+1)$ terms, equation (7.5) can be rewritten as follows:

$$\mathbf{I}(\Omega) \approx \mathbf{Y}(\Omega)\mathbf{V}(\Omega) \tag{7.7}$$

where vectors $\mathbf{V}(\Omega) = [V_{-N}(\Omega),\ldots,V_N(\Omega)]^T$ and $\mathbf{I}(\Omega) = [I_{-N}(\Omega),\ldots,I_N(\Omega)]^T$ collect the coefficients of the Fourier expansion of the corresponding v and i responses, respectively, with central angular frequency Ω.

Equation (7.7) provides a more compact representation of the characteristic of a PLTV element, where the admittance operator $Y_{PLTV}(t,\Omega)$ is replaced by a $(2N+1)\times(2N+1)$ complex matrix $\mathbf{Y}(\Omega)$:

$$\mathbf{Y}(\Omega) = \begin{bmatrix} Y_0(\Omega-N\omega_c) & \ldots & \vdots & \ldots & \vdots \\ Y_1(\Omega-N\omega_c) & \ldots & Y_{-1}(\Omega) & \ldots & \vdots \\ Y_2(\Omega-N\omega_c) & \ldots & Y_0(\Omega) & \ldots & Y_{-2}(\Omega+N\omega_c) \\ \vdots & \ldots & Y_1(\Omega) & \ldots & Y_{-1}(\Omega+N\omega_c) \\ \vdots & \ldots & \vdots & \ldots & Y_0(\Omega+N\omega_c). \end{bmatrix}. \tag{7.8}$$

It is worth noticing that the admittance matrix $\mathbf{Y}(\Omega)$ completely characterizes the voltage-current behavior of a two-terminal PLTV element and generalizes the classical LTI admittance $Y_{LTI}(\omega)$. In the latter case, it is also clear that LTI circuit elements do not involve constitutive relations with the coupling between the different harmonics of their port voltage port voltage variable (i.e., the entries of vector $\mathbf{V}$), leading to a diagonal matrix $\mathbf{Y}$. The above observation explains that a full admittance matrix is therefore needed to take into account the aforementioned coupling arising from to the time-varying activity of the circuit.

7.4 Modeling from external observations

This Section outlines the proposed modeling strategy for the external characterization of a PLTV circuit element based on the results collected in the previous sections and the schematic of Fig. 7.5. The above circuit is a realistic experimental setup for the estimation of the admittance representation (7.7) consisting of the direct interconnection of a real voltage source (an ideal voltage source $E(\omega)$ and its internal impedance $Z_{in}(\omega)$) with the PLTV element.

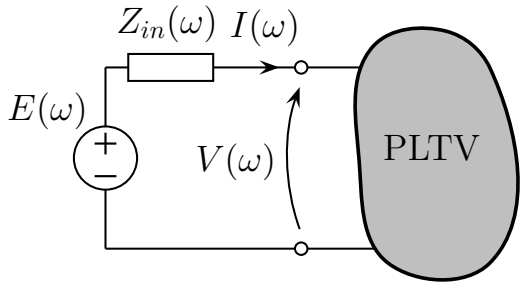

Figure 7.5: Example circuit used for computing the augmented admittance representation $\mathbf{Y}(\Omega)$ of the PLTV block from measured data.

For notational convenience, matrix $\mathbf{Y}(\Omega)$ is interpreted as a sequence of $(2N+1)$ column vectors, thus rewriting equation (7.7) as:

$$\begin{bmatrix} | \\ \mathbf{I}(\Omega) \\ | \end{bmatrix} \approx \begin{bmatrix} | & | & | \\ \mathbf{Y}_{-1}(\Omega) & \mathbf{Y}_0(\Omega) & \mathbf{Y}_{+1}(\Omega) \\ | & | & | \end{bmatrix} \begin{bmatrix} | \\ \mathbf{V}(\Omega) \\ | \end{bmatrix} \tag{7.9}$$

where $\mathbf{V}(\Omega)$ and $\mathbf{I}(\Omega)$ are vectors of dimension $(2N+1)$ representing the harmonics of voltage and the current variables across and through the PLTV element relative to the excitation $E(\omega)$.

From the above equation it is clear that the modeling of the port behavior of a PLTV circuit element like the one of Fig. 7.5 amounts to computing the column entries of the admittance matrix from a suitable set of responses of the device under modeling. A similar procedure can be applied for the alternate case of the impedance characterization by suitably exchanging the role of the current and voltage variables in (7.9) and in the formulas collected hereafter in this Section.

7.4.1 Analytical Case

Let's start by considering the schematic of Fig. 7.5 where the real voltage source is replaced by an ideal voltage excitation ($Z_{in} = 0\,\Omega$), thus $e(t) = v(t)$. According to (7.9), the columns of the admittance matrix can be selectively observed via a series of single tone voltage excitations $\mathbf{V}(\Omega) = \mathbf{E}_m(\Omega)$ at frequencies $(\Omega + m\omega_c)$. As an example, an ideal cisoidal excitation $e_m(t) = E_m \exp(j(\Omega + m\omega_c)t + j\phi_m)$ is mapped into the voltage vector

$$\mathbf{E}_m(\Omega) = \begin{bmatrix} 0 \\ \vdots \\ E_m \exp(j\phi_m) \\ 0 \\ \vdots \\ 0 \end{bmatrix}, \tag{7.10}$$

yielding to

$$\mathbf{I}(\Omega) \approx \mathbf{Y}(\Omega)\mathbf{E}_m = \mathbf{Y}_m(\Omega)E_m \exp(j\phi_m). \tag{7.11}$$

Of course, the previous equation does not suggest a ready-to-use method that is suited to real measurements yet because cisoidal excitations are complex signals that can not be used for real measurements and also because in most of the cases the effect of input impedance $Z_{in}(\omega)$ is not negligible, therefore the modeling procedure should be suitably revisited.

7.4.2 Real Measurement

In order to better understand the modeling procedure used for the real measurement, let us start from the case of an ideal voltage source as in the previous example leading to $e(t) = v(t)$. A realistic cosinusoidal voltage excitation $\tilde{e}_m(t)$ is now considered:

$$\begin{aligned} \tilde{e}_m(t;\pm\Omega) &= E_0 \cos((\Omega + m\omega_c)t + \phi_m) \\ &= \frac{E_0}{2}\left[\exp(j(\Omega + m\omega_c)t)\exp(j\phi_m) + \right. \\ &\quad \left. + \exp(-j(\Omega + m\omega_c)t)\exp(-j\phi_m)\right] \end{aligned} \tag{7.12}$$

where the phase ϕ_m is defined in accordance to the period of the device switching activity. Equation (7.12) can be rewritten in frequency-domain as a sum of delta functions:

$$\tilde{E}_m(\omega;\pm\Omega) = E_m^+\delta(\omega - \Omega - m\omega_c) + E_{-m}^-\delta(\omega + \Omega + m\omega_c) \tag{7.13}$$

where $E_m^+ = E_0/2\exp(j\phi_m)$ and $E_{-m}^- = E_m^{+*}$, leading to the source vector $\tilde{\mathbf{E}}_m(\pm\Omega)$ with two non-zero entries:

$$\tilde{\mathbf{E}}_m(\pm\Omega) = \begin{bmatrix} 0 \\ \vdots \\ 0 \\ E_m^+ \\ \vdots \\ 0 \\ \vdots \\ E_{-m}^- \\ 0 \\ \vdots \\ 0 \end{bmatrix}. \tag{7.14}$$

For this class of excitations, equation (7.11) is in turn replaced by the following sum of two contributions:

$$\mathbf{I}(\pm\Omega) = \mathbf{Y}_m(\Omega)E_m^+ + \mathbf{Y}_{-m}(-\Omega)E_{-m}^- \tag{7.15}$$

From the previous equation, it is clear that the two columns of the $\mathbf{Y}$ matrix of (7.9), $\mathbf{Y}_m$ and $\mathbf{Y}_{-m}$ can be obtained from the spectrum of two current measurements $\mathbf{I}_1(\pm\Omega)$ and $\mathbf{I}_2(\pm\Omega)$ via the solution of a linear system with complex coefficients. Specifically,

$$\begin{cases} \mathbf{I}_1(\pm\Omega) = \mathbf{Y}_m(\Omega)E_{m,1}^+ + \mathbf{Y}_{-m}(-\Omega)E_{-m,1}^- \\ \\ \mathbf{I}_2(\pm\Omega) = \mathbf{Y}_m(\Omega)E_{m,2}^+ + \mathbf{Y}_{-m}(-\Omega)E_{-m,2}^- \end{cases} \tag{7.16}$$

where $E_{\pm m,1}^{\pm} \neq E_{\pm m,2}^{\pm}$ are two excitations signals with a different phase term ϕ_m.

The proposed procedure can be generalized to the case where $Z_{in} \neq 0$, thus when $V(\omega) \neq E(\omega)$ by considering the following relation:

$$\mathbf{Y}(\Omega) \approx \begin{bmatrix} | & & | \\ \mathbf{I}_1 & \dots & \mathbf{I}_{(2N+1)} \\ | & & | \end{bmatrix} \left(\begin{bmatrix} | & & | \\ \mathbf{V}_1 & \dots & \mathbf{V}_{(2N+1)} \\ | & & | \end{bmatrix} \right)^{-1} \tag{7.17}$$

where $\mathbf{V}_n$ and $\mathbf{I}_n$ are column vectors containing $(2N+1)$ samples of the spectrum corresponding to the n-th voltage $V(\omega)$ and current $I(\omega)$ measurement of the overall $(2N+1)$.

The previous equation can be rewritten in a more compact form as:

$$\mathbf{Y}(\Omega) \approx \mathbf{I}\mathbf{V}^{-1} \tag{7.18}$$

7.4.3 Boost example

The proposed modeling strategy is used to estimate the admittance matrix $\mathbf{Y}(\Omega = 0)$ of the dc-dc converter in Fig. 7.1. The central angular frequency $\Omega = 0$ is used since the boost operates in an ideal condition with a dc source connected to its input port.

The admittance matrix is extracted by using the measurement setup shows in Fig. 7.5 where the PLTV element is replaced by the converter. The measurements are performed in time-domain by means of a digital scope (LeCroy 7300A and passive voltage probes) and the corresponding spectra are computed offline via MATLAB and the FFT routine. The sinusoidal voltage excitations $e_m(t)$ are generated by a function waveform generator (Agilent 33250A).

As a preliminary validation, Fig. 7.6 shows the graphical comparison between the stamps of the estimated and of the theoretical admittance matrices, being the latter obtained through a simple MATLAB simulation of the circuit of Fig. 7.1(a). This comparison provides a first accuracy check, highlighting a good agreement between the analytical and the measured stamps. A detailed discussion of model performance along with its comparison with a simplified Norton-like element is collected in the next Section.

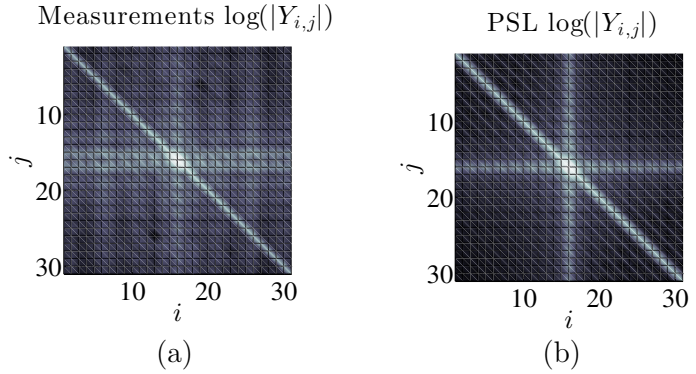

Figure 7.6: Comparison between the measured (left panel) and the theoretical (right panel) admittance matrix $\mathbf{Y}$ for $N = 15$. The grayscale image provides a graphical information of the absolute values of the matrix entries where white color is used for large dominant relative contributions.

7.5 Results

In this Section the CE of the boost converter of Fig. 7.1 are estimated by means of the proposed method and of the LTI Norton-based approach and compared with real measurements. The device under modeling is connected to the supply main through a LISN and a series resistance R_s as shown in the schematic of Fig. 7.7 (R_s is suitably varied to change the operating condition of the converter).

According to the EMC CIRSP-22 standard (Chap. 6) the differential mode (DM) CE are computed by the following relation:

$$V_{DM}(\omega) = \frac{V_L(\omega) - V_N(\omega)}{2} \tag{7.19}$$

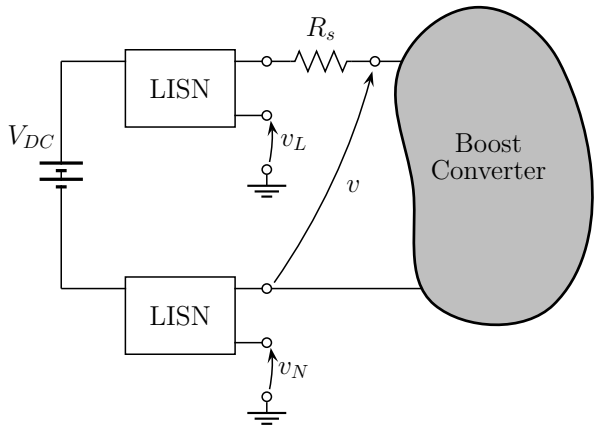

Figure 7.7: Experimental setup for model validation.

Validation for $R_s = 0\,\Omega$

In the first validation the converter is connected directly to the LISN, leading to $v \approx V_{DC}$. The measurement setup is implemented in an augmented MNA equation according to the procedure of Chap. 4, without considering the parasitic elements of the LISN and without modeling the electrical path of the common mode noise.

Figure 7.8 collects both the time-domain response of the differential mode voltage $v_{DM}(t)$ and its corresponding spectra and compares measured data with the predictions via two approached considered in the study. This validation shows a very good accuracy of both the Norton-based and the proposed models, leading to overlapping responses. The good behavior of the Norton-based model can be clearly explained by the choice $R_s = 0\,\Omega$. In this case, the setup of Fig. 7.7 approximately behaves as the circuit used for model estimation (i.e., an ideal voltage excitation connected to the converter as shown in Fig. 7.5).

Validation for $R_s = 56\,\Omega$

In this second validation, R_s is varied to modify the operating point of the converter and to stress the key features of the considered modeling approaches (see Fig. 7.9). This test confirms the same good accuracy of the proposed model, that turns out to provide a complete characterization of behavior of a PLTV circuit and offers a weak dependence on the operating condition. On the contrary, this Figure highlights the unavoidable lack of accuracy of simplified LTI models as the Norton-based element according to the preliminary assessment carried out in Sec. 7.2.

7.6 Insight into the admittance matrix

This Section provides a justification of the improved accuracy of CE predictions obtained with the alternative characterization of a PLTV circuit element in terms of its augmented admittance matrix

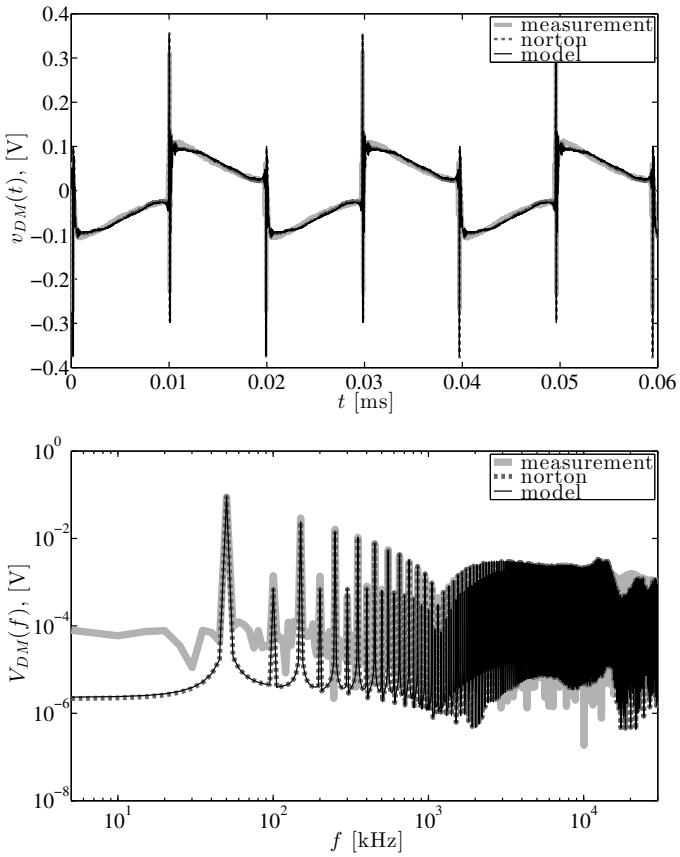

Figure 7.8: DM noise voltage response of the validation test case shown in Fig. 7.7 ($R_s = 0\,\Omega$). Light gray: measurement; dashed dark gray: Norton-based prediction; black: proposed method.

$\mathbf{Y}$ and discusses the possible separate contributions of different portions of the above matrix.

Without loss of generality, the following reasoning is based on the example boost converter that has a matrix $\mathbf{Y}$ with the dominant entries spread according to the picture of Fig. 7.6. it is worth remarking that most of the switching circuit characterized by a low-pass behavior (as the switching converter at hand) share the same features discussed above. However, similar conclusions can be drawn for possible different geometrical shapes of the augmented admittance matrix.

For the sake of illustration, Fig. 7.10 shows the interpretation of $\mathbf{Y}$ as the sum of the following four matrices.

$$\mathbf{Y} \approx \mathbf{Y}_F + \mathbf{Y}_{DC} + \mathbf{Y}_S + \mathbf{Y}_L. \tag{7.20}$$

The above terms can be classified on the basis of their effects on the final response of the proposed model. Specifically, they can be grouped into the pairs $(A) + (B)$ and $(C) + (D)$, leading to the low- and high-frequency components of the model response shown in Fig. 7.11. Additional details follow.

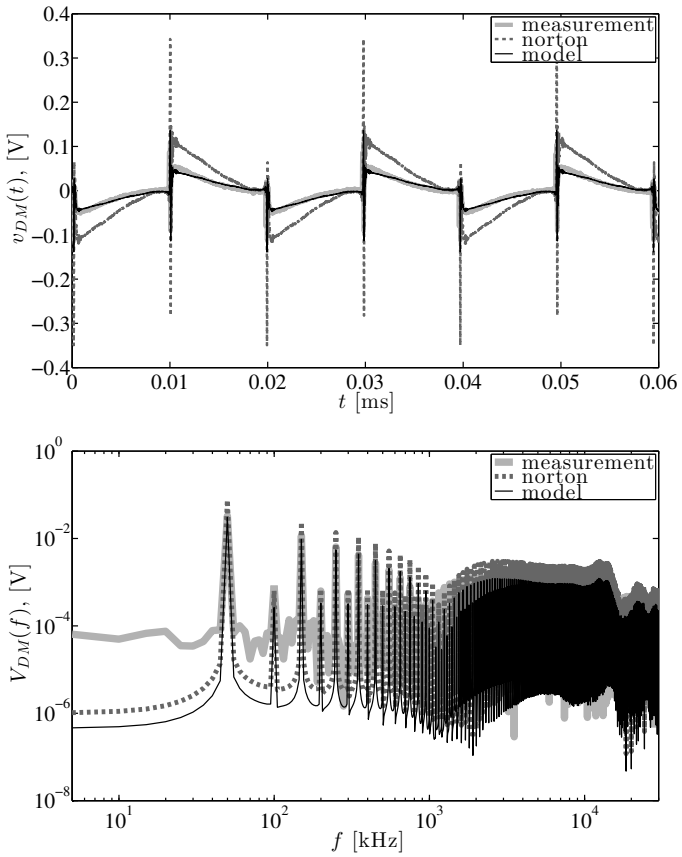

Figure 7.9: DM noise voltage response of the validation test case shown in Fig. 7.7 ($R_s = 56\,\Omega$). Light gray: measurement; dashed dark gray: Norton-based prediction; black: proposed method.

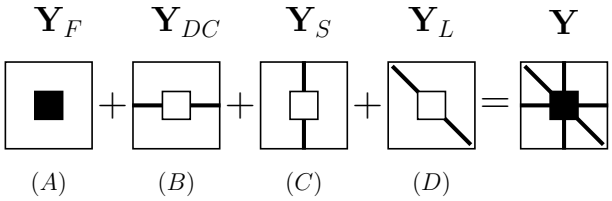

Figure 7.10: Structure of the admittance admittance of a boost-converter.

Functional behavior ($\mathbf{Y}_F$)

The functional central block of the admittance matrix $\mathbf{Y}$ is the portion that is most affected by the time-varying activity of the circuit and the coupling among different harmonics. It provides a good estimation of the low-frequency behavior of the device. The dimension of this central kernel depends on the cutoff frequency of the low-pass behavior of the circuit (in a boost converter it is related to the value of the inductance). However, its number is in general relatively small and for the example test case at hand it is in the range 5–10 (see Fig. 7.6).

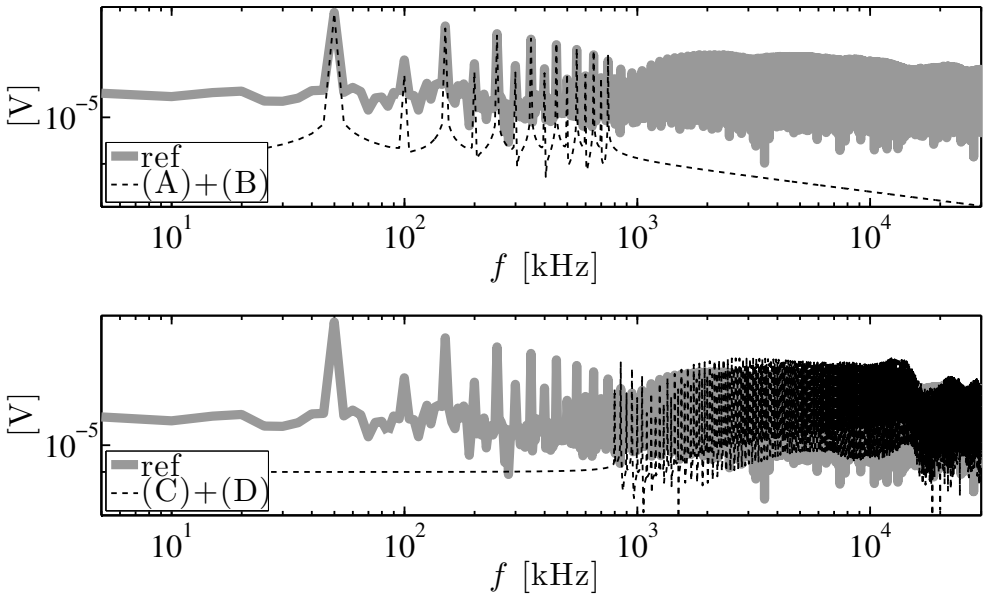

Figure 7.11: Frequency-domain spectrum of Fig. 7.9 obtained via the proposed model and the separate contributions of the blocks $(A) + (B)$ (low frequency characterization) or $(C) + (D)$ (high-frequency characterization) of Fig. 7.10

DC contribution ($\mathbf{Y}_{DC}$)

The DC matrix has all null entries with the exception of the central row, that is related to the coupling between harmonics of the port voltage excitation V_n and the DC component of the current response. Specifically:

$$\mathbf{I}_{DC} = \mathbf{Y}_{DC}\mathbf{V} \tag{7.21}$$

where only the harmonic of the current vector $\mathbf{I}_{DC}$ that corresponds to the DC component is different from zero.

High-frequency source term ($\mathbf{Y}_S$)

In the so-called source term only the central column of the matrix is different from zero. It can be simply estimated via the measurement of the current spectrum at the input port of the converter driven by a DC voltage generator. This contribution leads to the high-frequency EMI spectrum of the switched device (e.g., from 1 MHz to 30 MHz in Fig. 7.8 or Fig. 7.9). This block writes:

$$\mathbf{I}_S = \mathbf{Y}_S\mathbf{V} \tag{7.22}$$

where $\mathbf{I}_S$ is vector collecting the current harmonics I_n due to a voltage excitation $\mathbf{V}$ where only the DC harmonic $V_0 = V_{DC}$ is different from zero.

Dominant LTI behavior ($\mathbf{Y}_L$)

According to [20, 17], the diagonal matrix represents the LTI behavior of the circuit. Similar to a classical admittance, the harmonics of the current response I_n can be written as:

$$I_n = Y_{L,nn} V_n, \;\; n = -2N+1, \ldots 0, \ldots, 2N+1 \tag{7.23}$$

where the terms $Y_{L,nn}$ are the elements of the diagonal of the admittance matrix $\mathbf{Y}$. For the case of the boost converter it can be proven that this contribution is mostly related to the series inductor of the converter.

7.7 Chapter Summary

This Chapter proposes an alternative modeling approach for the prediction of the conducted emissions of switching devices. The general theory of periodical switched linear circuits is used to generate an augmented device port characterization that can be effectively computed from two set of voltage and current measurements and the solution of a linear problem. The estimation of the sensitive device responses like the current absorbed by a power converter connected to the supply main is carried out by means of the application of the augmented MNA description of the whole circuit introduced in the previous Chapters of this thesis. The proposed solution is compared with the classical state-of-the-art approaches available in the literature and based on the generation of simplified linear time invariant equivalents, thus highlighting a superior modeling accuracy in a wide range of device operating conditions. The feasibility of the method is demonstrated on a dc-dc boost converter by comparing the predicted CE responses with measured results.

Conclusions and Future Work

This thesis presented an innovative frequency-domain method for the analysis and the modeling of the EMI generated by switching circuits. The technique is based on a mathematical description of the inherently periodic time-varying nature of switching circuits by means of the theory developed for the time-varying systems and the generalized transfer function concept. The Fourier harmonics of the variables of a generic switching circuit are computed directly in frequency-domain by replacing each element of the circuit with its augmented admittance or impedance representation.

The proposed approach provides an augmented interpretation of the circuit that can be suitably implemented into the standard tools for the circuit analysis like the modified nodal analysis. Similar to the case of linear time-invariant circuits the augmented frequency-domain MNA equation is generated from topological inspection only, with emphasis on an intuitive physical based interpretation of the switching elements in the network. The new nodal unknowns in the advocated MNA equation correspond to the coefficients defining the expansion of the unknown current and voltage in terms of their Fourier series. The proposed method is proven to offer a modular approach to circuit analysis, leading to accurate results and remarkable speed-up with respect to standard time-domain simulations. The method is then specialized in the assessment of the steady-state behaviors of several switching converters. Afterwards, the method is applied to the prediction of the conducted emissions of a real boost converter. The obtained results are then validated via a series of measurements.

Finally, the theory of linear time-varying systems is used to generate an augmented one-port characterization of a generic switching circuit from two set of voltage and current measurements. The augmented representation is implemented in the augmented MNA equation allowing to predict the behavior of the noisy currents generated by the switching circuit for different working conditions. The proposed solution is compared with the classical state-of-the-art approaches available in the literature and that are based on a linear time-invariant small signal approximation of the circuits highlighting a superior modeling accuracy in a wide range of device operating conditions. The feasibility of the method is demonstrated on a real dc-dc converter by comparing predicted responses with measured data.

Although the results presented in this thesis have demonstrated the effectiveness of the proposed approach for both the analysis and the modeling of the CE generated by the switching circuits and converters, it could be further developed in a number of ways. Firstable the possibility of including into the proposed simulation also tool nonlinear elements, the transient response of the circuit (generalized Laplace transform) and the variability of some parameters of the circuit. Also the modeling needs some improvements especially for the estimation of the admittance matrix in order to apply the procedure to more complex devices.

Bibliography

[1] A. Papoulis, *Signal Analysis*. Auckland: McGraw- Hill, copyr. 1977.

[2] L. A. Zadeh, “Frequency analysis of variable networks”, Proceedings of the IRE, Vol. 38, No. 3, pp. 291–299, Mar. 1950.

[3] L. A. Zadeh, Charles A. Desoer, *Linear System Theory: the State Space Approach*. New York : McGraw- Hill, copyr. 1963.

[4] M.-L. Liou, “Exact analysis of linear circuits containing periodically operated switches with applications”, IEEE Trans. on Circuit Theory, Vol. 19, No. 2, pp. 146–154, Mar. 1972.

[5] T. Strom, S. Signell, “Analysis of periodically switched linear circuits”, IEEE Trans. on Circuits and Systems, Vol. 24, No. 10, pp. 531–541, Oct. 1977.

[6] Fei Yuan, Ajoy Opal, *Computer Methods for Analysis of Mixed-Mode Switching Circuits*, Kluwer Achademic Publisher, 2004.

[7] Fei Yuan; A. Opal, “Sensitivity analysis of periodically switched linear circuits using an adjoint network technique," Proc. of the *1999 IEEE International Symposium on Circuits and Systems, ISCAS’99*, pp. 331–334, 1999.

[8] J. A. Alvarez Martin, J. R. Melgoza, J. J. Rincon Pasaye, “Exact steady state analysis in power converters using Floquet decomposition.", Proc. of the *North American Power Symposium*, pp. 1–7, Aug. 2011.

[9] J. Kovar, Z. Kolka, D. Biolek, “Comparison of averaging and harmonic balance methods for switched DC-DC converters.", in Proc. of *17th Int. Conf. on Mixed Design of ICs and Systems*, pp. 402–407, June 2010.

[10] H. Behjati, L. Niu, A. Davoudi, P. L. Chapman, “Alternative time-invariant multi-frequency modeling of PWM DC-DC converters", IEEE Trans. on Circuits and Systems I: Regular Papers.

[11] T. A. C. M. Claasen, W. F. G. Mecklenbrauker, “On stationary linear time-varying systems”, IEEE Trans. on Circuits and Systems, Vol. 29, No. 3, pp. 169–184, Mar. 1982.

[12] H. Sandberg, E. Mollerstedt, Bernhardsson, “Frequency-domain analysis of linear time-periodic systems", IEEE Trans. on Automatic Control, Vol. 50, No. 12, pp. 1971–1983, Dec. 2005.

[13] P. M. Mellacheruvu, S. M. Mahajan, C. L. Carnal, J. J. Biernacki, “Application of Fourier and Laplace transform techniques for modeling an electric circuit having time-varying components", Proc. of the *Thirty-Eighth Southeastern Symposium on System Theory, SSST ’06*, pp. 147–151, 5–7 March 2006.

[14] J. Lerdworatawee, Won Namgoong, “Generalized noise analysis of active mixers by simple linear periodic time-varying circuit model", Proc. of *IEEE Custom Integrated Circuits Conference*, pp. 293–296, Sept. 21, 2005.

[15] J. Lerdworatawee, Won Namgoong, “Generalized Linear Periodic Time-Varying Analysis for Noise Reduction in an Active Mixer", IEEE Journal of Solid-State Circuits, Vol. 42, No. 6, pp. 1339–1351, Jun. 2007.

[16] Liou, M. L., Yen-Long Kuo, Clement F. Lee, “A tutorial on computer-aided analysis of switched-capacitor circuits”, Proceedings of the IEEE , Vol. 71, No.8, pp. 987,1005, Aug. 1983.

[17] J. Roychowdhury, “Reduced-order modeling of time-varying systems", IEEE Trans. on Circuits and Systems II: Analog and Digital Signal Processing, Vol. 46, No. 10, pp. 1273–1288, Oct 1999.

[18] Ting Mei; H. Thornquist, E. Keiter, S. Hutchinson, “Structure preserving reduced-order modeling of linear periodic time-varying systems", Proc. of *2011 IEEE/ACM International Conference on Computer-Aided Design, ICCAD*, pp. 361–366, 7-10 Nov. 2011.

[19] R. Trinchero, I. S. Stievano, and F. G. Canavero, “Steady-state response of periodically switched linear circuits via augmented time-invariant nodal analysis,” J. Elect. Comput. Eng., vol. 2014, article ID 198273, 2014.

[20] R. Trinchero, I. S. Stievano, F. G. Canavero, “Steady-state analysis of switching power converters via augmented time-invariant equivalents", IEEE Trans. on Power Electronics, Vol. 29, No. 11, pp. 5657–5661, Nov. 2014.

[21] M. Okumura, H. Tanimoto, T. Itakura, T. Sugawara, “Numerical noise analysis for nonlinear circuits with a periodic large signal excitation including cyclostationary noise sources", IEEE Trans. on Circuits and Systems I: Fundamental Theory and Applications, Vol. 40, No. 9, pp. 581–590, Sep. 1993.

[22] P. Dobrovolny, Gerd Vandersteen, P. Wambacq, S. Donnay, “Analysis and white-box modeling of weakly nonlinear time-varying circuits", Proc. of *Design, Automation and Test in Europe Conference and Exhibition, DATE*, pp. 624–629, 2003.

[23] J. Vlach, K. Singal, *Computer Methods for Circuit Analysis and Design*. New York: Van Nostrand Reinhold, copyr. 1994.

[24] C.-W. Ho, A. E. Ruehli, P. A. Pierce, “The modified nodal approach to network analysis", IEEE Trans. on Circuits and Systems, Vol. 22, No. 6, pp. 504–509, Jun. 1975.

[25] A. Davoudi, J. Jatskevich, T. De Rybel, “Numerical state-space average-value modeling of PWM DC-DC converters operating in DCM and CCM”, IEEE Trans. on Power Electronics, Vol. 21, No. 4, pp. 1003–1012, Jul. 2006.

[26] A. Sangswang and C. O. Nwankpa, “Noise characteristics of DC-DC boost converters: experimental validation and performance evaluation,” IEEE Trans. on Industrial Electronics, vol. 51, no. 6, pp. 1297–1304, Dec. 2004.

[27] V. Tarateeraseth, S. Kye Yak, F.G. Canavero, R.W. Chang, “Systematic electromagnetic interference filter design based on information from in-circuit impedance measurements”, IEEE Trans. on Electromagnetic Compatibility, Vol. 52, No. 3, pp. 588–598, Aug. 2010.

[28] X. Pei, Jian Xiong, Y. Kang, J. Chen, “Analysis and suppression of conducted EMI emission in PWM inverter", in Proc. of the *Int. Conf. IEMDC'03 on Electric Machines and Drives*, Vol. 3, pp. 1787–1792, June 2003.

[29] Y. Koyama, M. Tanaka, H. Akagi,“Modeling and analysis for simulation of common-mode noises produced by an inverter-driven air conditioner", in Proc. of *Int. Conf. on Power Electronics (IPEC)*, pp. 2877–2883, June 2010.

[30] E. Rondon-Pinilla, F. Morel, C. Vollaire, J.-L. Schanen, “Modeling of a Buck Converter With a SiC JFET to Predict EMC Conducted Emissions", IEEE Trans. on Power Electronics, Vol. 29, No. 5, pp. 2246–2260, May 2014.

[31] V. Tarateeraseth, I.A. Maio, F.G. Canavero, “Assessment of equivalent noise source approach for EMI simulations of boost converter", Proc. of the *20th Int. Zurich Symposium on EMC*, pp. 353–356, Jan. 2009.

[32] Y. Liu, Kye Yak See; King-Jet Tseng, “Conducted EMI prediction of the PFC converter including nonlinear behavior of boost inductor", IEEE Trans. on EMC, Vol. 55, No. 6, pp. 1107–1114, Dec. 2013.

[33] F. Yang, X. Ruan, Q. Ji; Z. Ye, “Input differential-mode EMI of CRM boost PFC converter", IEEE Trans. on Power Electronics, Vol. 28, No. 3, pp. 1177–1188, March 2013.

[34] R. Kahoul, Y. Azzouz, P. Marchal, B. Mazari, “New Behavioral Modeling for DC Motor Armatures Applied to Automotive EMC Characterization", IEEE Trans on EMC, Vol. 52, No. 4, pp. 888–901, Nov. 2010.

[35] Jian Sun, Lei Xing, “Parameterization of three-phase electric machine models for EMI simulation", IEEE Trans. on Power Electronics, Vol.29, No. 1, pp. 36–41, Jan. 2014.

[36] H. Bishnoi, P. Mattavelli, R. Burgos, D. Boroyevich, “EMI behavioral models of DC-Fed Three-Phase motor drive systems", IEEE Trans. on Power Electronics, Vol. 29, No. 9, pp. 4633–4645, Sept. 2014.

[37] H. Bishnoi, A. C. Baisden, P. Mattavelli, D. Boroyevich, “Analysis of EMI terminal modeling of switched power converters", IEEE Trans. on Power Electronics, Vol. 27, No. 9, pp. 3924–3933, Sept. 2012.

[38] S. Ahmed, D. Boroyevich, F. Wang, and R. Burgos, "Development of a new voltage source inverter (VSI) average model including low frequency harmonics," in *Proc. Twenty-Fifth Annual IEEE Appl. Power Electron. Conference*, Palm Springs, CA, USA, Feb. 2010, pp.881–886.

[39] A. Ravindranath, S.K. Mishra, and A. Joshi, "Analysis and PWM control of switched boost inverter," IEEE Trans. Ind. Electron., vol. 60, no. 12, pp. 5593–5602, Dec. 2013.

[40] S. Almer, S. Mariethoz, and M. Morari, "Dynamic phasor model predictive control of switched mode power converters," IEEE Trans. on Control Systems Technology. (in press).

[41] S. R. Sanders, J. M. Noworolski, X. Z. Liu, G. C. Verghese, "Generalized averaging method for power conversion circuits," IEEE Trans. on Power Electronics, Vol. 6, no. 2, pp. 251–259, Apr. 1991.

[42] K. Hausmair, S. Chi; P. Singerl, C. Vogel, "Aliasing-free digital Pulse-Width Modulation for Burst-Mode RF transmitters," IEEE Trans. on Circuits and Systems I: Regular Papers, Vol. 60, no. 2, pp. 415–427, Feb. 2013.

[43] M. H. Rashid, *Power Electronics: Circuits, Devices and Applications*. Prentice Hall 3rd edition, copyr. 2004.

[44] M. Wens, N. Steyaert, *Design and Implementation of Fully-Integrated Inductive Dc-Dc converters in Standard CMOS*. Springer, copyr. 2011.

[45] T. L. Skvarenina, *The Power Electronics Handbook*. CRC Press, copyr. 2002.

[46] 'Federal Communications Commission', http://www.fcc.gov/, accessed 2015.

[47] 'International Electrotechnical Commission', http:///www.iec.ch/, accessed 2015.

[48] C. R. Paul, *Introduction to Electromagnetic Compatibility*. Wiley-Interscience, copyr. 2006.

[49] L. Schwartz, *Mathematics for the Physical Sciences*. Hermann, copyr.1966.